Modulating the Conducting Orbitals of Single Molecules Through Chemical Design

Jonathan Low

Submitted in partial fulfilment of the

requirements for the degree of

Doctor of Philosophy

in the Graduate School of Arts and Sciences

COLUMBIA UNIVERSITY

2018

ABSTRACT

Modulating the Conducting Orbitals of Single Molecules Through Chemical Design

Jonathan Low

The last two decades have seen huge improvements in measuring the conductance of single molecules, especially with the establishment of the scanning tunneling microscope break-junction (STM-BJ) method. The availability of such a robust and reliable measurement technique allows for the study of more exotic molecules with built-in functionality. In this thesis, we employ creative chemical design to manipulate transport in a single molecule junction by tuning the conducting frontier orbitals. We investigate three classes of materials – thiophene dioxides, mixed-valence bis(triarylamines), and benzotriazinyl-based Blatter radicals. Within each system, we probe changes in conducting behavior or interfacial interactions that arise from modifying the molecular structure.

First, we demonstrate that a family of thiophene pentamers, which typically conduct through their highest occupied molecular orbital (HOMO), can be induced to conduct through their lowest unoccupied molecular orbital (LUMO) instead. This is akin to switching between from hole to electron transport. The switching was achieved using chemical modifications that drastically lower the LUMO level toward the Fermi energy of gold: oxidation at the sulfur position to form thiophene dioxides combined with installing electron-withdrawing groups at the 3- and 4-positions of the thiophene moiety. The ability to tune HOMO versus LUMO transport is potentially useful for assembling molecular circuits with n- and p-type components.

Next, we found that oxidation of bis(triarylamine) molecular wires into their mixed-valence state shifts their conducting orbitals close to the Fermi energy of gold, making these wires

highly conducting. We measured the length dependent transport of three bis(triarylamine) molecules. In their neutral state, the conductance of these compounds decreases with increasing length, which is observed for many different systems. However, when they are chemically oxidized, the mixed-valence molecular wires show an increase in conductance with increasing length. Such wires that maintain good electrical transport over long distances are valuable for building efficient molecular devices.

We then investigated the interaction of half-filled orbitals in organic radicals with gold substrates to explore the potential of these compounds for spintronic and magnetic applications. We found that a Blatter radical functionalized with gold-binding thiomethyl groups displays different charge transfer behavior depending on the environment. Under ultra-high vacuum, X-ray spectroscopy shows that the radical molecules in contact with the gold substrate gain a charge from gold and their singly unoccupied molecular orbitals get filled. Contrastingly, in solution-based single molecule measurements, the radical loses the electron from its singly occupied molecular orbital instead, and only the conductance of the oxidized species is detected.

We further probed the nature of charge transfer between the Blatter radical and gold in ultra-high vacuum by comparing spectroscopic measurements from three different derivatives. The derivative that was functionalized with two thiomethyl groups in order for it to be measured in the STM-BJ was the only molecule to undergo charge transfer in ultra-high vacuum. Two other Blatter derivatives that had only one and no thiomethyl groups did not show the same charge transfer; these retained their radical character even when in contact with the gold substrate. Therefore, the results indicate that only one of the thiomethyl groups mediates charge transfer between radical and substrate.

The body of work presented herein shows that chemical modifications to old and new systems can be used to modulate transport in junctions via the intrinsic character of the molecules rather than external engineering factors. Thiophene dioxides are a relatively nascent class of materials that already show versatility as molecular conductors, while organic mixed-valence and radical systems have been heavily researched in other fields but less so in molecular electronics. This thesis therefore seeks to encourage further research that takes advantage of the unique electronic structure of these materials systems to discover new transport phenomena.

Contents

List of Figures

Acknowledgments

I came to Columbia without knowing anyone in the city and without having really considered many aspects of what graduate school would entail besides research. Since I only had the chance to visit two schools in America, I also didn't have any basis for comparing the social aspects of different departments or the environment fostered by the Professors, students, and staff. So, I had no idea what to expect. In the first week here, when the department not only paid for all our meals, but also for activities to encourage the first years (and others) to socialize over tasty beverages, I knew that I had somehow fortuitously ended up in the right place. Therefore, I really appreciate all the people who continue to work hard to keep our spirits up when science doesn't behave, which is often.

I'm grateful for the guidance of my advisor Luis, who has supported my scientific advancement and exemplifies the idea that the best science happens through collaboration rather than by competition. He trusts his students implicitly and has provided the intellectual freedom for us to pursue projects that excite us. Being a talented speaker and writer himself, he has also helped me develop into a good communicator of science by encouraging me to present my work at various conferences. At these events, never shies away from introducing me to his colleagues and treats everyone his group as peers rather than subordinates.

Latha started out as a collaborator but has since become more like a co-advisor. The first time she asked me to present in her group meeting, I was terrified since there was so much I didn't know. However, that simple action made me feel like I really belonged to their group as well. She has also poured in plenty of time, effort, and thought to the projects I sprang upon her, for which I'm truly appreciative. I learn something new from her every time we meet to discuss science. Her generosity and intellect are qualities that I will strive toward.

Many other people were directly involved in the work within this thesis as well as those projects not presented here. It has been very stimulating learning and working with all of them. There is not enough space to list everyone individually, but I've been fortunate to interact with so many great scientists from Brookhaven National Lab and the Elettra Sincrotrone Trieste who are also great people.

There are also so many people that make day-to-day research very painless, and they contribute to a healthy work environment. Brandon Fowler and Steffen Jockusch perform mass spectrometry and EPR, and make both conveniently available. I also thank all the admin and support staff, especially for their willingness to help us out during our teaching assignments but also for ensuring all the events which we enjoy run smoothly. Here, I would also like to highlight Colin and his group, who have been so generous with their resources and equipment. They never hesitate to share chemicals and solvents with a small lab like ours who aren't always as well stocked. They also share a lot of their intellect through Mike Steigerwald, with whom I've had many enlightening discussions.

Next, there all the people who are the backbone of my support system here. The Campos group has always been small enough that we know each other inside out and are great friends besides being colleagues. All of you have left an indelible mark on my time at Columbia. I have the words but not the space to acknowledge each and every one of you. That said, I especially appreciate that Jessica, Sam, and Spencer have gone through the five years together with me. I hope the rest of you all continue to fight over lab music, discuss what constitutes a sandwich, work out together, celebrate birthdays, but especially continue to have lunch together every day!

The Venkataraman group members have also welcomed me as one of their own. Many of them have taken the time to train me to use their equipment and been very patient with me

whenever I have needed help due to inexperience. They are also always happy to teach me about molecular junctions and discuss our experimental results. It has been fun having an extra set of departmental social events and happy hours to attend together.

My time in New York has been enriched by the friends I spend time with away from the rigors of graduate school. I will miss Thursday ~~soccer~~ football with Mars Rovers, and climbing – as well as other random activities – with Anouck and Maddy. I will miss Jessica's refreshing cocktails and Evan's sumptuous meals, usually enjoyed in the wonderful company of Sam, Bonnie, Andrew, Andrew, Anastasia, Anouck, and recently Rachel. I will miss 4am FIFA with Matt and Soumyo. All these activities have provided solace at the end of long work days or weeks.

Last but definitely not least, I would like to acknowledge my family. We have spent years spread over many different parts of the world, but their support has been unwavering. My parents have worked especially hard and made many sacrifices to provide me with anything I needed to be successful and for that, I am grateful.

Cheers,

J. Low

To my family

Verena

Yoon Pak

Justin

Candice

1. Introduction

In 1956, Isaac Asimov wrote the short story "*The Last Question*", envisioning that as computers increased in complexity, transistors would be replaced by "molecular valves", enabling huge computing power to be transported to the far reaches of space. While mankind has not quite been able to develop space travel to the extent that Asimov imagined, our transistors have shrunk by such a large degree that it is conceivable they will soon reach the molecular size regime. In fact, many of us today carry around tiny devices in our pockets that contain over 2 billion transistors. The rate of miniaturization of transistors was articulated by Moore's famous paper in 1965, and silicon-based semiconductor chips have largely obeyed Moore's Law with the number of transistors in a chip doubling every year.[1] However, the implementation of a "molecular valve" has lagged in development. In 1974, Aviram and Ratner sparked the imagination of the scientific community by proposing a molecular diode,[2] and since then, the field of molecular electronics has been growing steadily.[3-8]

The simplest molecular circuit has three components – the metal electrodes, the molecule itself, and the functional groups or linkers on the molecule that allow it to bind to the electrode. The initial challenge for the field was to develop techniques to reliably connect the molecules to the electrodes in the desired orientation. Simple molecules like alkanedithiols were therefore the subject of intense study due to their ability to form self-assembled monolayers with one thiol end anchored on a bottom electrode and the other end exposed to make a top contact. A variety of creative methods have been utilized to connect the least amount of molecules possible between electrodes, including hanging mercury drops, nanopores, arrays of interconnected nanoparticles, and many others that are summarized elsewhere.[3,8] However, none of these are able to form a true single molecule junction. The invention of the scanning tunneling microscope (STM) by Binning

and Rohrer in 1981 and the subsequent development of STM break junction techniques by Xu and Tao in 2003 was therefore a breakthrough for the field.[9] Conductance signatures of discrete single molecules could now be reliably measured. Naturally, having a robust method of forming single molecule junctions allowed for increasingly complex molecular backbones to be studied.

While developing methods to measure molecules lies in the realm of physics and engineering, the responsibility of making interesting molecules to study rests on the shoulders of synthetic chemists. Chemical modifications that seem trivial on paper often require extensive thought and resources. From the humble alkane, one might think of moving down the periodic table and replacing carbon with silicon or germanium.[10] From oligophenyls, one might modify the aromatic building blocks to thiophenes or thiophene-dioxides,[11-13] or perhaps change the connection point to the electrode from meta to para.[14-18] All of these chemical modifications have a marked effect on the magnitude of conductance observed. There are countless molecules that can be made and measured, but the ultimate goal from a design perspective is to be able to draw a molecule on paper and predict how it will conduct. To some extent, this has already been achieved. For example, quantum interference is well known to suppress conductance,[14-18] as does aromaticity to a smaller degree,[19-21] while π and σ conjugation are known to increase conductance.[10,22] However, even these supposedly well-established concepts can break down as the complexity of the systems increases. For example, azulene, a seven-membered ring, exhibits atypical quantum interference behavior.[23] Therefore, not only do new design rules need to be established, but the old rules must also continually be tested with new molecules.

Chemists have the ability to manipulate chemical structure to tune the character and energy of a molecule's frontier orbitals. By extension, since these are the orbitals that determine conductance behavior, chemists should also be able to tune molecular conductance. This thesis

explores methods to manipulate conducting orbitals through chemical design. I present work on 3 families of molecules – oligothiophenes, bis(triarylamines) and 1,2,4-benzotriazinyl radicals. Each of these families explores a different chemical design element: modulating transport between the two frontier orbitals, inducing near-resonant transport through oxidation, and characterizing the interface between singly occupied frontier orbitals and a metal respectively.

The remainder of this section focuses on the measurement technique used and theoretical aspects of how the frontier orbitals of the molecules relate to conductance. The section concludes with an outline of the subsequent sections.

1.1 The STM-BJ technique

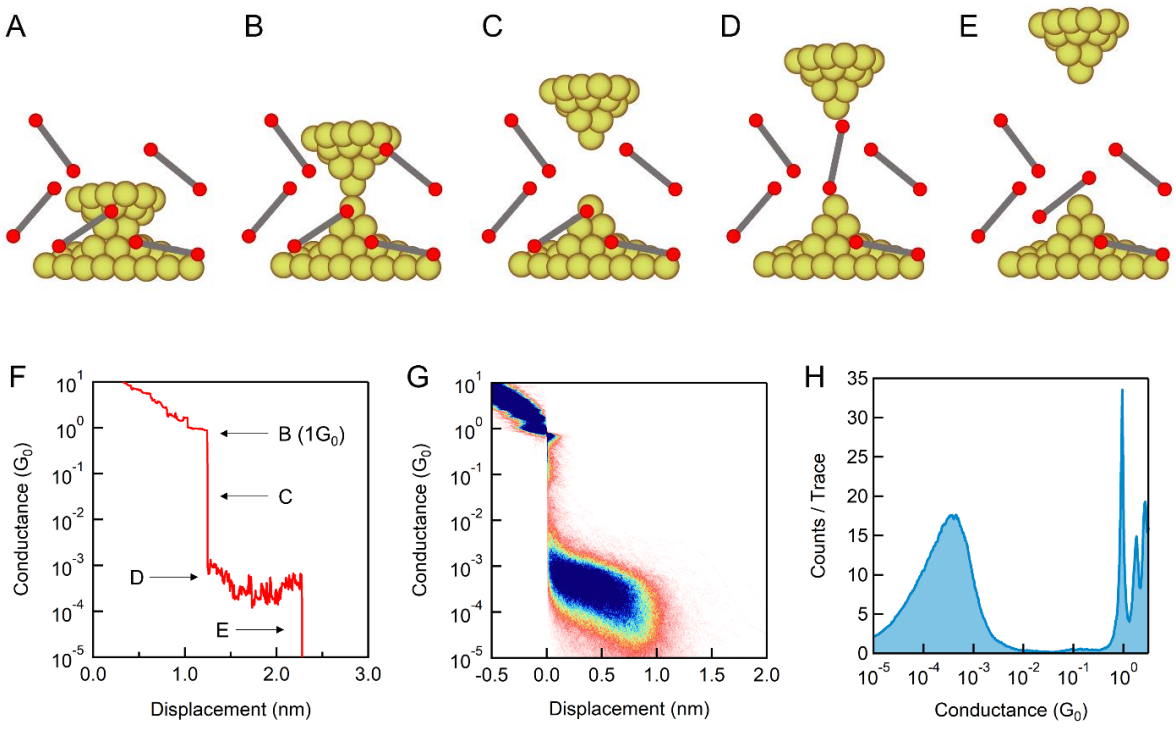

Figure 1.1. (a-e) Schematic representation of the formation of a molecular junction as the STM tip is retracted. See text for details. (f) A single conductance versus displacement curve with the features labelled according to the corresponding schematics in (a-e). (g) A 2D conductance histogram formed by overlaying 3000 individual conductance versus displacement curves. (h) A 1D conductance histogram obtained by logarithmically binning the 3000 conductance versus displacement curves.

The scanning tunneling microscope break-junction (STM-BJ) method is one of the most versatile techniques for measuring the conductance of single molecules available and is utilized throughout this thesis.[9] All the measurements were performed using a home-built STM setup, with freshly cleaved gold wires for the tip and gold evaporated onto mica or steel pucks as the substrate. Broadly, a solution of the molecules (usually in a high boiling point solvent like trichlorobenzene) is dropped onto the substrate. A bias is applied between the tip and substrate and the conductance is recorded as function of vertical tip displacement during the formation of molecular junctions.

Figures 1.1a to 1.1e depict in more detail the process of recording a single conductance versus displacement trace; an example trace is shown in Figure 1.1f with the corresponding features marked out. First, the gold STM tip is driven into contact with the gold substrate (Figure 1.1a). It is retracted until a point contact forms (Figure 1.1b), resulting in a conductance feature at 1 G_0 (= $2e^2/h$ = 77.48 μS). Further retraction ruptures the point contact (Figure 1.1c), leaving room for a molecule to bind (Figure 1.1d). When the molecule is in the junction, a conductance plateau is seen below 1 G_0. Finally, the junction breaks when the tip is withdrawn further, and the conductance drops to the noise floor (Figure 1.1e). This process can be repeated thousands of times to collect a statistically significant number of traces. To analyze the data, the collected traces can be aligned and overlaid to obtain a 2D histogram (Figure 1.1g) which provides information about the average junction length, or they can be compiled into a logarithmically binned 1D histogram (Figure 1.1h) from which the peak conductance can be extracted using a gaussian fit. This peak is the most probable conductance for the molecule.

1.2 The Transmission Function

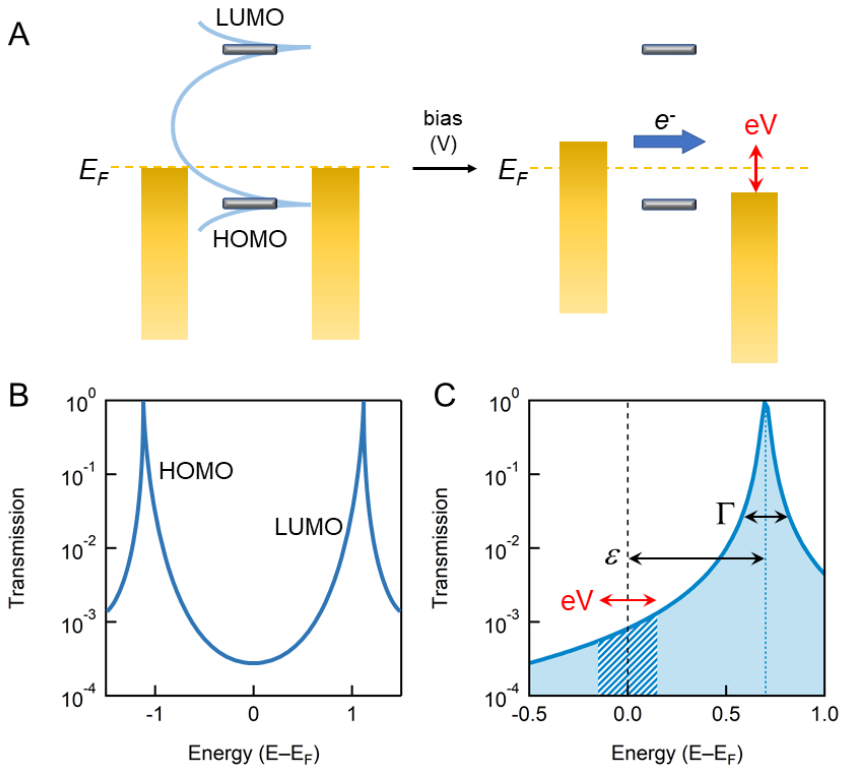

Figure 1.2. (a) Schematic representation of a molecular junction showing the Fermi energy E_F of gold and the relative HOMO and LUMO. The transmission function is depicted in the light blue curve. When a bias is applied, the chemical potential of the electrodes shifts and electrons can start to flow across the junction, as shown on the right. (b) Sample transmission function showing a HOMO and LUMO resonance. (c) Sample transmission function of a LUMO conducting molecule modeled by a single Lorentzian function, showing the coupling, Γ, and the energy of the orbital relative to E_F, ε. The dark shaded area is the current under bias V.

We now describe the physical origins of the molecular conductance signature. There are two main mechanisms of conduction – hopping and tunneling.[22,24] For short molecules, the tunneling mechanism dominates. The molecules act as a tunneling barrier through which the electron wavefunction transmits across without a change in phase. The tunneling probability depends on the height of the barrier, which depends on the proximity of a conducting orbital to the Fermi energy (E_F) of the electrodes and the length of the molecule. If the molecular orbitals are far from the leads or if the molecule is very long, the barrier is high. Although tunneling is suppressed

in longer molecules, electrons can still transverse the barriers by an incoherent hopping mechanism induced by the electric field instead. The difference between the tunneling and hopping regimes is that the former has weak temperature dependence, while the latter is thermally activated. The molecules reported in this thesis all conduct via a tunneling mechanism and the remainder of this section will focus on the tunneling model for transport.

When a molecule is bound between two electrodes, the molecular orbitals all align themselves at a certain energy relative to E_F. Usually, E_F lies in between the highest occupied molecular orbital (HOMO) and the lowest unoccupied molecular orbital (LUMO); the orbital that is closer to E_F will dominate transport. The HOMO and LUMO do not remain as discrete states due to the interaction with the continuum of metal states and broaden out as depicted in the left panel of Figure 1.2a. Due to the broadened molecular states, electrons at E_F can tunnel through the molecule with some finite probability. This probability can be mapped by a transmission function, which expresses the probability that an electron will tunnel through the junction at a given energy relative to E_F. An example is shown in Figure 1.2b. The sharp peaks in the transmission function indicate where the HOMO and LUMO lie. These are the molecular resonances, and denote a probability of 1, or perfect transmission. It follows that if the HOMO or LUMO resonance is perfectly aligned with E_F, transmission is maximized, and resonant transport is achieved.

In most cases, HOMO and LUMO are far from E_F. For such off-resonant transport, the transmission function can be approximated by a single Lorentzian curve with the form:[25-27]

$$T(E) = \frac{4\Gamma^2}{(E-\varepsilon)^2 + 4\Gamma^2}$$

where Γ is the coupling of the orbital to the electrode and affects the resonance width, and ε is the distance of the resonance from E_F (Figure 1.2c). When a bias is applied to the junction, the

chemical potential of the two electrodes shift apart from E_F by eV as shown in the right panel of Figure 1.2a. The current through the junction is found by integrating below the curve in the bias window, which is the shaded area in Figure 1.2c.

1.3 Thesis Outline

By understanding the mechanics behind molecular transport, we can design and synthesize molecules with a specific purpose. For example, to induce LUMO conducting behavior, we can pull the LUMO down toward E_F by adding electron withdrawing groups to the molecular backbone. Conversely, to make HOMO conducting molecules, electron donating groups are used instead. In practice it is often not so straightforward to cause a large shift in conducting orbitals,[28-30] especially when acting within constraints like a fixed molecular length.

Chapter 2 focuses on this very problem, using strong electron-withdrawing modifications on an oligothiophene backbone of fixed length to a switch the conducting orbital. Modulating between HOMO and LUMO conduction is analogous to inducing p-type or n-type transport in semiconductors. Specifically, we functionalize the thiophene monomers at the sulfur site to make thiophene-1,1-dioxides. These powerful electron-withdrawing moieties cause LUMO to shift drastically toward E_F.

One class of compounds that have exciting applications in the molecular electronic field are organic radicals. Radicals possess half-filled orbitals that often lie in the HOMO-LUMO gap; these are usually close to E_F and theoretical calculations predict that these compounds can show enhanced conductance versus their non-radical counterparts.[31] Furthermore, the half-filled orbitals allow the possibility to explore single molecule spin-based transport.[32] Though many stable organic radicals are available,[33] very few of these have been measured in molecular junctions to determine their conductance characteristics.[34-36] A larger body of work is needed to investigate

structure-property relationships in the various radicals available in order to be able to modulate transport through such half-filled orbitals. Chapters 3 to 5 explore aspects of transport in organic radicals.

In chapter 3, we study the conduction of bis(triarylamines), which are organic mixed-valence compounds. By definition, mixed-valence compounds are open-shell radicals. Chemical oxidation is used to generate the mixed-valence radical cation state of the bis(triarylamines) and show that these states are highly conducting. Length dependent studies surprisingly reveal an increase in conductance with length, which indicates transport in a regime that is close to the molecular resonance. Both of these phenomena are rarely observed at low bias and introduces the idea of using mixed-valence states to design highly conductive molecular wires.

Chapters 4 and 5 are devoted to the study of the interface between metals and neutral organic radicals. In chapter 4, the single molecule conductance of the 1,2,4-benzotriazinyl radical, or Blatter radical is measured in solution and we find that the molecule is oxidized in the junction to form a closed-shell species. Surprisingly, in X-ray spectroscopic measurements performed under ultrahigh vacuum, the radical gains an electron from the gold substrate and is reduced instead. Such an anomalous result shows that this particular metal-radical interface is very sensitive to its environment and small changes to the alignment between E_F and the radical's singly occupied and unoccupied frontier orbitals can cause different charge transfer behavior.

We extend the scope of X-ray spectroscopy to different Blatter radical derivatives in Chapter 5. It turns out that the charge transfer under ultrahigh vacuum is not merely due to the proximity of the radical singly occupied molecular orbital to E_F but is mediated by one of the thiomethyl functional groups that was added. Blatter radicals without this thiomethyl group do not interact strongly with the gold surface and do not undergo charge transfer. Therefore, to achieve

molecular transport through the singly occupied orbital in this system, the thiomethyl group must be decoupled from the conducting orbital.

The concluding remarks and future work can be found in chapter 6.

1.4 References

[1] Moore, G. E. "Cramming More Components onto Integrated Circuits." *Electronics* **1965**, *38*, 114-117.

[2] Aviram, A.; Ratner, M. A. "Molecular rectifiers." *Chem. Phys. Lett.* **1974**, *29*, 277-283.

[3] Xiang, D.; Wang, X.; Jia, C.; Lee, T.; Guo, X. "Molecular-Scale Electronics: From Concept to Function." *Chem. Rev.* **2016**, *116*, 4318-4440.

[4] Aradhya, S. V.; Venkataraman, L. "Single-molecule junctions beyond electronic transport." *Nat. Nanotechnol.* **2013**, *8*, 399-410.

[5] Su, T. A.; Neupane, M.; Steigerwald, M. L.; Venkataraman, L.; Nuckolls, C. "Chemical principles of single-molecule electronics." *Nat. Rev. Chem.* **2016**, *1*, 16002.

[6] Chen, F.; Hihath, J.; Zhifeng, H.; Li, X.; Tao, N. J. "Measurement of Single-Molecule Conductance." *Annu. Rev. Phys. Chem.* **2007**, *58*, 535-564.

[7] Tao, N. J. "Electron transport in molecular junctions." *Nat. Nanotechnol.* **2006**, *1*, 173-181.

[8] Hylke, B. A.; Bert de, B. "Electrical conduction through single molecules and self-assembled monolayers." *J. Phys.: Condens. Matter* **2008**, *20*, 013001.

[9] Xu, B.; Tao, N. J. "Measurement of single-molecule resistance by repeated formation of molecular junctions." *Science* **2003**, *301*, 1221-1223.

[10] Su, T. A.; Li, H.; Klausen, R. S.; Kim, N. T.; Neupane, M.; Leighton, J. L.; Steigerwald, M. L.; Venkataraman, L.; Nuckolls, C. "Silane and Germane Molecular Electronics." *Acc. Chem. Res.* **2017**, *50*, 1088-1095.

[11] Dell, E. J.; Capozzi, B.; DuBay, K. H.; Berkelbach, T. C.; Moreno, J. R.; Reichman, D. R.; Venkataraman, L.; Campos, L. M. "Impact of Molecular Symmetry on Single-Molecule Conductance." *J. Am. Chem. Soc.* **2013**, *135*, 11724-11727.

[12] Capozzi, B.; Dell, E. J.; Berkelbach, T. C.; Reichman, D. R.; Venkataraman, L.; Campos, L. M. "Length-Dependent Conductance of Oligothiophenes." *J. Am. Chem. Soc.* **2014**, *136*, 10486-10492.

[13] Dell, E. J.; Capozzi, B.; Xia, J.; Venkataraman, L.; Campos, L. M. "Molecular length dictates the nature of charge carriers in single-molecule junctions of oxidized oligothiophenes." *Nat. Chem.* **2015**, *7*, 209-214.

[14] Guédon, C. M.; Valkenier, H.; Markussen, T.; Thygesen, K. S.; Hummelen, J. C.; van der Molen, S. J. "Observation of quantum interference in molecular charge transport." *Nat. Nanotechnol.* **2012**, *7*, 305.

[15] Markussen, T.; Stadler, R.; Thygesen, K. S. "The Relation between Structure and Quantum Interference in Single Molecule Junctions." *Nano Lett.* **2010**, *10*, 4260-4265.

[16] Arroyo, C. R.; Tarkuc, S.; Frisenda, R.; Seldenthuis, J. S.; Woerde, C. H. M.; Eelkema, R.; Grozema, F. C.; van der Zant, H. S. J. "Signatures of Quantum Interference Effects on Charge Transport Through a Single Benzene Ring." *Angew. Chem., Int. Ed.* **2013**, *52*, 3152-3155.

[17] Tada, T.; Yoshizawa, K. "Molecular design of electron transport with orbital rule: toward conductance-decay free molecular junctions." *Phys. Chem. Chem. Phys.* **2015**, *17*, 32099-32110.

[18] Yoshizawa, K.; Tada, T.; Staykov, A. "Orbital Views of the Electron Transport in Molecular Devices." *J. Am. Chem. Soc.* **2008**, *130*, 9406-9413.

[19] Chen, W.; Li, H.; Widawsky, J. R.; Appayee, C.; Venkataraman, L.; Breslow, R. "Aromaticity Decreases Single-Molecule Junction Conductance." *J. Am. Chem. Soc.* **2014**, *136*, 918-920.

[20] Fujii, S.; Marqués-González, S.; Shin, J.-Y.; Shinokubo, H.; Masuda, T.; Nishino, T.; Arasu, N. P.; Vázquez, H.; Kiguchi, M. "Highly-conducting molecular circuits based on antiaromaticity." *Nat. Commun.* **2017**, *8*, 15984.

[21] Yin, X.; Zang, Y.; Zhu, L.; Low, J. Z.; Liu, Z.-F.; Cui, J.; Neaton, J. B.; Venkataraman, L.; Campos, L. M. "A reversible single-molecule switch based on activated antiaromaticity." *Sci. Adv.* **2017**, *3*.

[22] Choi, S. H.; Frisbie, C. D. In *Charge and Exciton Transport through Molecular Wires*; Siebbeles, L. D. A., Grozema Ferdinand, C., Eds.; Wiley: Weinheim, Germany, 2011, p 61-91.

[23] Xia, J.; Capozzi, B.; Wei, S.; Strange, M.; Batra, A.; Moreno, J. R.; Amir, R. J.; Amir, E.; Solomon, G. C.; Venkataraman, L.; Campos, L. M. "Breakdown of Interference Rules in Azulene, a Nonalternant Hydrocarbon." *Nano Lett.* **2014**, *14*, 2941-2945.

[24] Choi, S. H.; Risko, C.; Delgado, M. C. R.; Kim, B.; Brédas, J.-L.; Frisbie, C. D. "Transition from Tunneling to Hopping Transport in Long, Conjugated Oligo-imine Wires Connected to Metals." *J. Am. Chem. Soc.* **2010**, *132*, 4358-4368.

[25] Kim, Y.; Pietsch, T.; Erbe, A.; Belzig, W.; Scheer, E. "Benzenedithiol: A Broad-Range Single-Channel Molecular Conductor." *Nano Lett.* **2011**, *11*, 3734-3738.

[26] Hong, W.; Valkenier, H.; Mészáros, G.; Manrique, D. Z.; Mishchenko, A.; Putz, A.; García, P. M.; Lambert, C. J.; Hummelen, J. C.; Wandlowski, T. "An MCBJ case study: The influence of π-conjugation on the single-molecule conductance at a solid/liquid interface." *Beilstein J. Nanotechnol.* **2011**, *2*, 699-713.

[27] Kim, Y.; Hellmuth, T. J.; Sysoiev, D.; Pauly, F.; Pietsch, T.; Wolf, J.; Erbe, A.; Huhn, T.; Groth, U.; Steiner, U. E.; Scheer, E. "Charge Transport Characteristics of Diarylethene Photoswitching Single-Molecule Junctions." *Nano Lett.* **2012**, *12*, 3736-3742.

[28] Venkataraman, L.; Park, Y. S.; Whalley, A. C.; Nuckolls, C.; Hybertsen, M. S.; Steigerwald, M. L. "Electronics and Chemistry: Varying Single-Molecule Junction Conductance Using Chemical Substituents." *Nano Lett.* **2007**, *7*, 502-506.

[29] Frisenda, R.; Perrin, M. L.; Valkenier, H.; Hummelen, J. C.; van der Zant, H. S. J. "Statistical analysis of single-molecule breaking traces." *Phys. Status Solidi B* **2013**, *250*, 2431-2436.

[30] Zhao, X.; Huang, C.; Gulcur, M.; Batsanov, A. S.; Baghernejad, M.; Hong, W.; Bryce, M. R.; Wandlowski, T. "Oligo(aryleneethynylene)s with Terminal Pyridyl Groups: Synthesis and Length Dependence of the Tunneling-to-Hopping Transition of Single-Molecule Conductances." *Chem. Mater.* **2013**, *25*, 4340-4347.

[31] Heimel, G.; Zojer, E.; Romaner, L.; Brédas, J.-L.; Stellacci, F. "Doping Molecular Wires." *Nano Lett.* **2009**, *9*, 2559-2564.

[32] Sanvito, S. "Molecular spintronics." *Chem. Soc. Rev.* **2011**, *40*, 3336-3355.

[33] Hicks, R. G. "What's new in stable radical chemistry?" *Org. Biomol. Chem.* **2007**, *5*, 1321-1338.

[34] Frisenda, R.; Gaudenzi, R.; Franco, C.; Mas-Torrent, M.; Rovira, C.; Veciana, J.; Alcon, I.; Bromley, S. T.; Burzurí, E.; van der Zant, H. S. J. "Kondo Effect in a Neutral and Stable All Organic Radical Single Molecule Break Junction." *Nano Lett.* **2015**, *15*, 3109-3114.

[35] Hayakawa, R.; Karimi, M. A.; Wolf, J.; Huhn, T.; Zöllner, M. S.; Herrmann, C.; Scheer, E. "Large Magnetoresistance in Single-Radical Molecular Junctions." *Nano Lett.* **2016**, *16*, 4960-4967.

[36] Liu, J.; Zhao, X.; Al-Galiby, Q.; Huang, X.; Zheng, J.; Li, R.; Huang, C.; Yang, Y.; Shi, J.; Manrique, D. Z.; Lambert, C. J.; Bryce, M. R.; Hong, W. "Radical-Enhanced Charge Transport in Single-Molecule Phenothiazine Electrical Junctions." *Angew. Chem., Int. Ed.* **2017**, *56*, 13061-13065.

2. Tuning the Polarity of Charge Carriers Using Electron Deficient Thiophenes

Abstract: Thiophene-1,1-dioxide (TDO) oligomers have fascinating electronic properties. Previous work in our group used thermopower measurements to show that a change in charge carrier from hole to electron occurs with increasing length of TDO oligomers when single-molecule junctions are formed between gold electrodes. In this chapter, we show that the dominant conducting orbitals for thiophene/TDO oligomers of fixed length can be tuned by altering the strength of the electron acceptors incorporated into the backbone. We use the scanning tunneling microscope break-junction (STM-BJ) technique and apply a recently developed method to determine the dominant transport channel in single-molecule junctions formed with these systems. Through these measurements, we find that increasing the electron affinity of thiophene derivatives, within a family of pentamers, changes the polarity of the charge carriers systematically from holes to electrons, with some systems even showing mid-gap transport characteristics.

2.1 Preface

This chapter is based on a manuscript titled *Tuning the Polarity of Charge Carriers Using Electron Deficient Thiophenes* by Jonathan Z. Low, Brian Capozzi, Jing Cui, Sujun Wei, Latha Venkataraman, and Luis M. Campos published in *Chemical Science*.[1]

2.2 Introduction

The ability to control transport through molecules is vital to constructing electronic devices using molecular components.[2,3] Ideally, one would be able to draw each molecule that suits a desired purpose in a circuit, akin to manipulating molecular structure to induce p-type, n-type, or ambipolar transport in organic electronics.[4-11] However, where there exist robust strategies for tuning transport at the macroscale,[8-14] handles to tune transport at the molecular level are more limited in their effectiveness. Generally, vastly different families of molecules with different

linkers and hence different coupling to the gold electrodes are required to vary the polarity of the charge carriers. For example, pyridine terminated molecular backbones conduct through the lowest unoccupied molecular orbital (LUMO),[15] while amine terminated backbones conduct through the highest occupied molecular orbital (HOMO).[16]

Within these families of molecules (pyridine or amines), substituents added along the molecular backbone can modulate conductance but never change the frontier orbital that controls transport.[16-18] For example, amine-terminated phenyl rings derivatized with substituents that alter their ionization potentials by over 1eV show a variation in single-molecule conductance of around 50%, but do not show a change in dominant transport orbital.[16] Similarly, families of molecular wires of the same length only show deviations in conductance of a factor of three or less when substituents on the same backbone are varied.[17,18] In general, tuning transport characteristics within a family of molecules is a fundamental chemistry challenge; subtle chemical modifications do not generally lead to drastic changes in the conducting molecular orbitals or the polarity of the charge carriers.

Thiophene derivatives are an excellent platform for investigating single molecule transport as they display strong conductance signatures.[19-26] Recently, we reported that molecular length can be used to tune the polarity of charge carriers in single molecule junctions based on oxidized thiophene oligomers.[21] We found that molecules containing thiophene-1,1-dioxide have large contributions to conductance from both the HOMO and LUMO (Figure 2.1a), with the LUMO contribution increasing as successive thiophene-1,1-dioxide units are added. That is, the trimer TOT (where 'T' denotes a thiophene unit and 'O' denotes thiophene-1,1-dioxide) is HOMO-conducting, while the hexamer TOOOOT is LUMO-conducting. This is due to the LUMO resonance of the oligomers shifting closer to the Fermi energy (E_F) of gold with increasing

length.[21,22] In order to characterize the electronic properties of this family of materials, we obtained their Seebeck coefficients using thermopower measurements, which can provide information on how well the orbitals align to the gold E_F. We also recently developed a new strategy to experimentally determine the polarity of charge carriers in single molecule junctions by performing conductance measurements in a polar environment – a technique wherein the bias window is opened asymmetrically across the junction.[22,27] The method, used in this study, elucidates the dominant conducting orbital by mapping the molecular transmission functions in the region near to E_F.

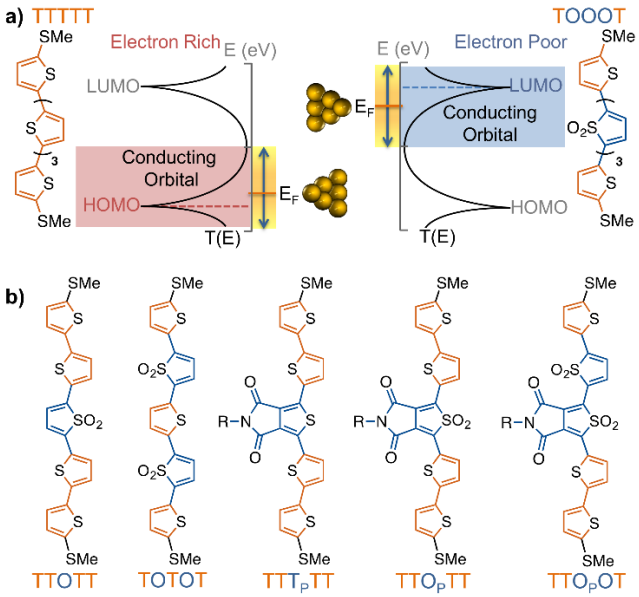

Figure 2.1. (a) Scheme showing how a HOMO-conducting pentathiophene (red highlight) can be tuned to be LUMO-conducting by changing the electronic structure of the monomers into electron deficient units (blue highlight), such as thiophene-1,1-dioxide (denoted by 'O'). (b) Pentamers with additional modulations made at the 3,4-positions of the thiophene moiety. The central units are thus thienopyrrolodione (T_P) and the oxidized version (O_P). Note that all structures have solubilizing alkyl chains which are omitted here for clarity; the full structures are available in the synthetic details section.

2.3 Results and discussion

Since the impact of molecular length of conjugated molecules on the narrowing the HOMO-LUMO gap is well understood,[28] we sought to investigate how molecules of a fixed length can be chemically manipulated to effectively change their charge carrier properties – a strategy that can be useful to connect electrodes of static dimensions. While oligothiophenes are known to be HOMO-conducting,[20] we explored their chemistry to obtain strongly electron-deficient monomers that increase their electron affinity, thus tuning their transport properties from HOMO, to mid-gap, and LUMO-conducting, all within pentameric thiophene derivatives (Figure 2.1b). Such a transition in oligomers of equal length is unprecedented and is only possible because of the dramatic change in electronic properties arising from the oxidation of thiophenes.

Here, we investigated seven pentamers where we varied the number of electron-deficient and electron-rich units. This was achieved by chemically modifying the thiophenes either at the 3,4-positions, as in the case of thienopyrrolodione (T_P), or at the 1-position to obtain derivatives of thiophene-1,1-dioxide (O). Synthetic details are available in section 2.6. We chose the T_P unit because it is a ubiquitous electron poor building block in high performance donor-acceptor type materials for organic electronics.[29-36] Moreover, we also highlight in Figure 2.2 that the use of the electrophilic oxygen in Rozen's reagent ($HOF{\cdot}CH_3CN$)[37-39] enabled the synthesis of an oxidized thienopyrrolodione (O_P). T_P is an extremely challenging unit to oxidize into O_P because the electron-withdrawing substituents at the 3,4-position make the sulfur weakly nucleophilic (Figure 2.2). Rozen's reagent was also vital in the synthesis of the most electron deficient pentamer TTO_POT (see section 2.6 for details). All the molecules are terminated by thiomethyl groups that have a strong binding affinity to undercoordinated gold atoms on the STM tip and substrate.

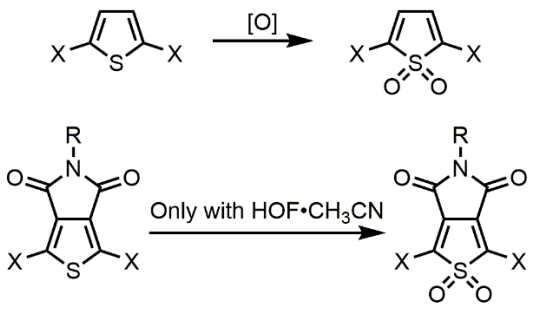

Figure 2.2. Thiophene oxidation can be carried out by [O] = peracids, dimethyldioxirane or HOF,[40,41] but the thienopyrrolodione moiety can only be oxidized by Rozen's reagent.

We use the solvent induced asymmetric bias window opening technique to measure the conductance of molecular junctions at different bias voltages in order to gain insight into the orbital that dominates transport. In this method, the molecular orbital alignment is pinned relative to the substrate potential; an increase in conductance with increasing (decreasing) tip bias thus implies HOMO (LUMO) dominated transport, as detailed previously.[27] The conductance of each of the seven thiophene pentamers was measured in propylene carbonate (PC) at more than ten different biases between -0.54 and +0.90 V. At each bias (applied to the tip), thousands of conductance versus displacement traces are collected, where an STM tip (coated with Apiezon Wax W) is repeatedly driven into and retracted from a gold substrate in a dilute solution of the molecules.[42,43] The conductance versus displacement traces for a compound at each bias are compiled into logarithmically binned histograms which are fit with a Gaussian; the peak value is the most probable conductance of the molecule. Figures 2.3a and b show the histograms at 2 (of the 15) biases for TTTTT and TOOOT respectively. TTTTT shows increasing conductance with increasing positive bias while the trend for TOOOT is reversed, demonstrating that the former is HOMO-conducting while the latter has transport dominated by the LUMO.

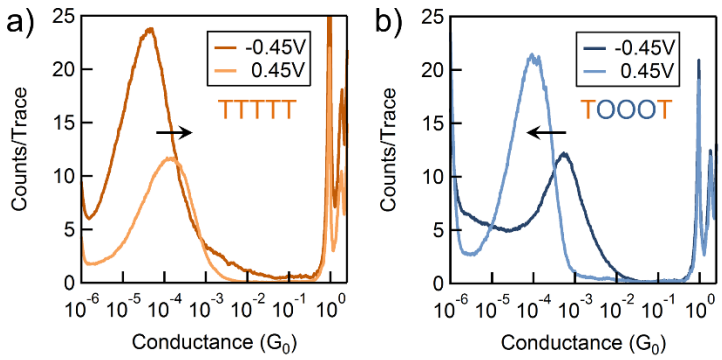

Figure 2.3. Conductance histograms at two tip-biases for (a) TTTTT and (b) TOOOT respectively measured in propylene carbonate. The arrows indicate increasingly positive biases.

The conductance versus voltage measurements for all the molecules are summarized in Figure 2.4. Each data point represents the peak conductance value from a histogram of thousands of measurements at a particular bias (see Figure 2.5, Figure 2.6, and Figure 2.7 for the histograms). The orange traces in Figure 2.4 represent TTTTT, TTT_PTT and TTOTT, which all unambiguously display HOMO-dominated conductivity, since conductance increases significantly with increasing positive voltage and decreases with increasing negative voltage. We were consistently unable to record histograms for TTT_PTT at biases higher than 0.45 V because no molecular junctions formed. TOTOT and TTO_PTT, in green, both show mid-gap transport around zero bias: conductance increases slightly as bias increases in either direction. We postulate this behavior arises because the LUMOs are moving closer to E_F and begin to contribute to conduction with a similar magnitude as the HOMO. E_F therefore lies in a flat region of the transmission function of these molecules. Again, we also emphasize that only one 'O_P' unit has comparable, even slightly more, electron withdrawing strength than two 'O' units.

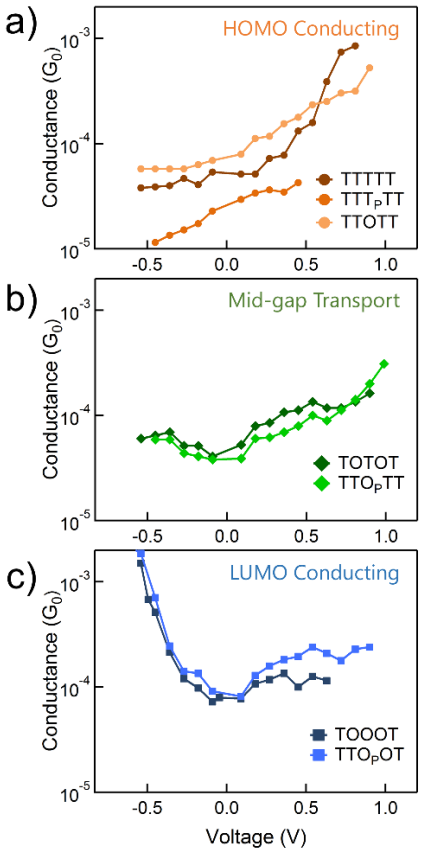

Figure 2.4. The variation of conductance versus voltage for the seven pentamers measured in propylene carbonate with an insulated STM tip in order to determine the dominant conducting orbitals. The molecules which show (a) HOMO-conduction, (b) mid-gap transport, or (c) LUMO-conduction are shown in different panels.

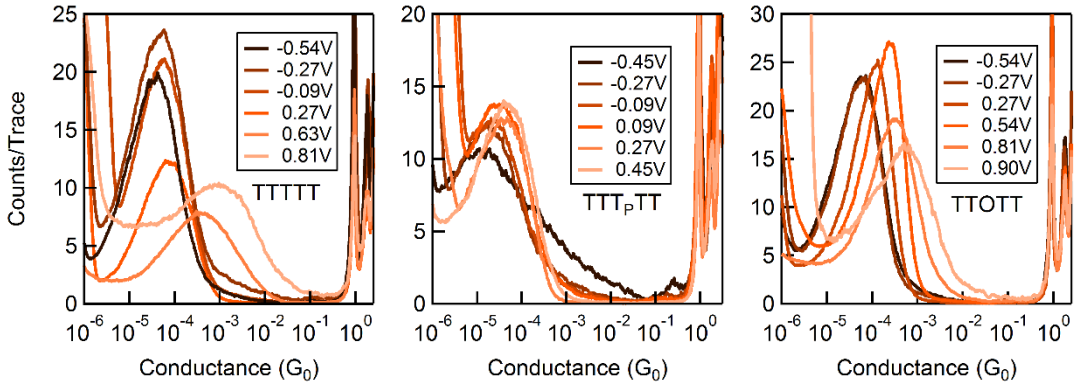

Figure 2.5. Selected conductance histograms for the HOMO-conducting molecules.

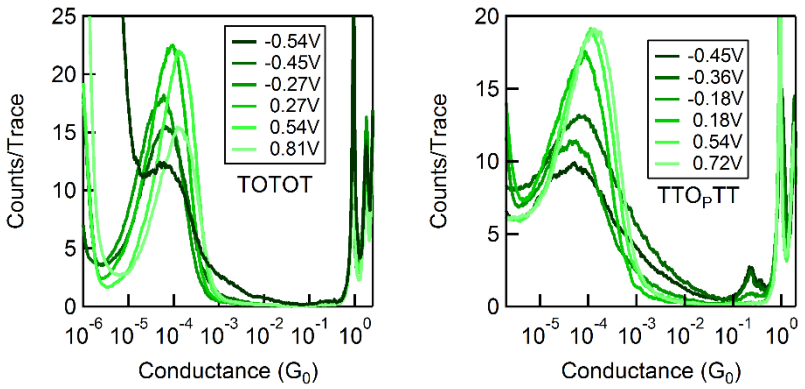

Figure 2.6. Selected conductance histograms for the ambipolar molecules.

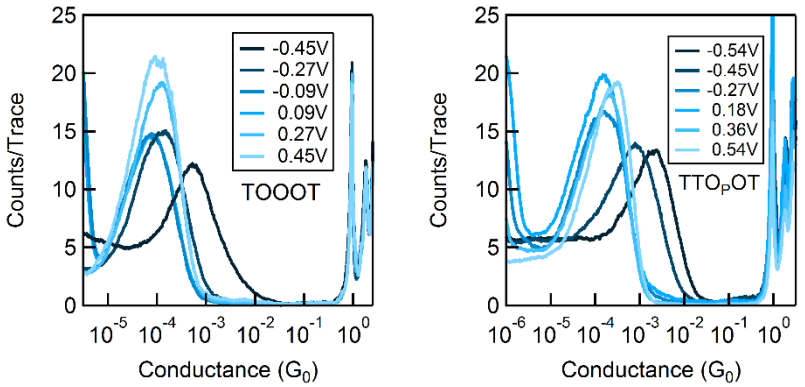

Figure 2.7. Selected conductance histograms for the LUMO-conducting molecules.

In contrast, TOOOT and TTO$_P$OT both show sharp increases in conductance at high negative tip biases. It is postulated that the LUMO energies are now low enough and close to the gold E_F to contribute significantly to conductance. Note that both molecules still show a very slight increase in conductance with increasing positive voltage, indicative of residual HOMO contributions. This HOMO contribution to conductance in TOOOT is not surprising; we previously reported that its Seebeck coefficients exhibited a distribution over positive and negative values, reflecting its contributions from both frontier molecular orbitals.[21] It is also noteworthy that the increase in conductance at high negative bias for these two molecules is very abrupt, indicating that the LUMO is very close in energy to the gold E_F. The corresponding gradual

increase at positive bias for the HOMO-conducting molecules shows that their HOMOs are not as close to E_F. Finally, despite the asymmetry in TTO_POT, no bimodal distribution of conductance was observed in the histograms (Figure 2.7), showing that conductance is insensitive to molecular orientation. Measurements of other fully conjugated asymmetric molecules also show a similar insensitivity.[44-46]

In order to understand how the fundamental electronic properties of the molecules affect the contributions of the conducting frontier molecular orbitals, we carried out UV-Vis absorption measurements and cyclic voltammetry (CV). The UV-Vis spectra of the compounds (Figure 2.8a) show a clear decrease in optical energy gap as the number and strength of electron withdrawing groups in the backbone increases. The spectra of all the pentamers are broad and show no vibronic fine structure, in contrast to fully oxidized thiophene-1,1-dioxide oligomers that have vibronic features due to their rigidity.[47] The cyclic voltammograms of all the pentamers show clear reduction and oxidation peaks, and have good redox stability over several cycles (Figure 2.9), apart from TTTTT which shows no reduction peak within the solvent window. The HOMO and LUMO levels were determined by calibrating the onsets of oxidation and reduction to the oxidation peak of ferrocene (details in section 2.5). These frontier energy levels are summarized in Figure 2.8b. The LUMO of TTTTT was estimated by adding the optical gap (taken from the onset of UV absorption, λ_{onset}) to its HOMO and this is therefore a lower-bound for the LUMO. For the other compounds, HOMO-LUMO gaps are estimated from CV, and the λ_{onset} follows the same trend. While we note that energy alignments with the gold E_F change when the molecules are bound in a junction, the frontier orbital energies offer an important correlation to the nature of the conducting orbitals, as we discuss below.

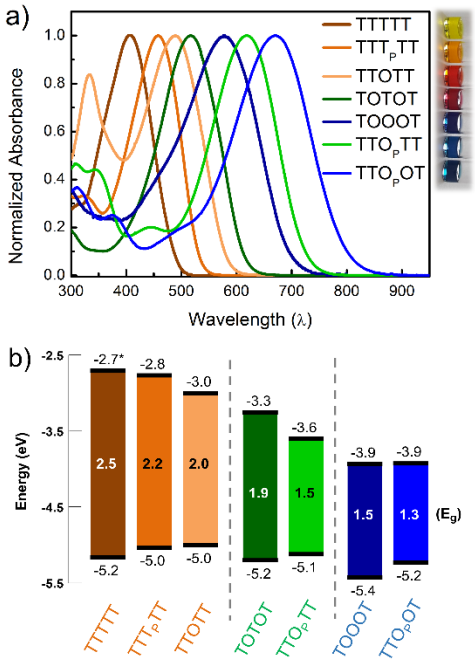

*Figure 2.8. (a) UV-Vis absorption spectra of the 7 pentamers studied, shown with a photo of the corresponding compounds in chloroform solution. (b) HOMO and LUMO levels of the pentamers obtained from cyclic voltammetry. The gray lines segregate the HOMO-conducting, mid-gap transport, and LUMO-conducting molecules respectively. *The LUMO of TTTTT was obtained by adding the band gap estimated from the onset of UV-Vis absorption since no reduction wave was observed.*

We find that adding a single electron-withdrawing group in the backbone has a twofold effect of slightly raising the HOMO and lowering the LUMO. Specifically, we observe that TTTPTT, TTOTT and TTOPTT have a higher HOMO and lower LUMO than the parent TTTTT. This may be due to the introduction of donor-acceptor interactions, which hybridize the frontier orbitals of the electron rich and electron poor moieties within the molecule[48] but a full discussion why the HOMO rises is beyond the scope of this paper. The extent of LUMO-lowering is representative of the strength of the electron withdrawing group: the pyrrolodione group only lowers the LUMO slightly, while thiophene dioxide has a stronger effect due to both the absence of aromaticity and the addition of the strongly electron-withdrawing oxygen atoms directly on sulfur. Combining both chemical modifications on the same central thiophene in TTOPTT lowers

the LUMO by almost 1eV compared to TTTTT even though the HOMO levels are similar. This LUMO-lowering effect is comparable to that of the commonly used cyano substitution strategy.[49]

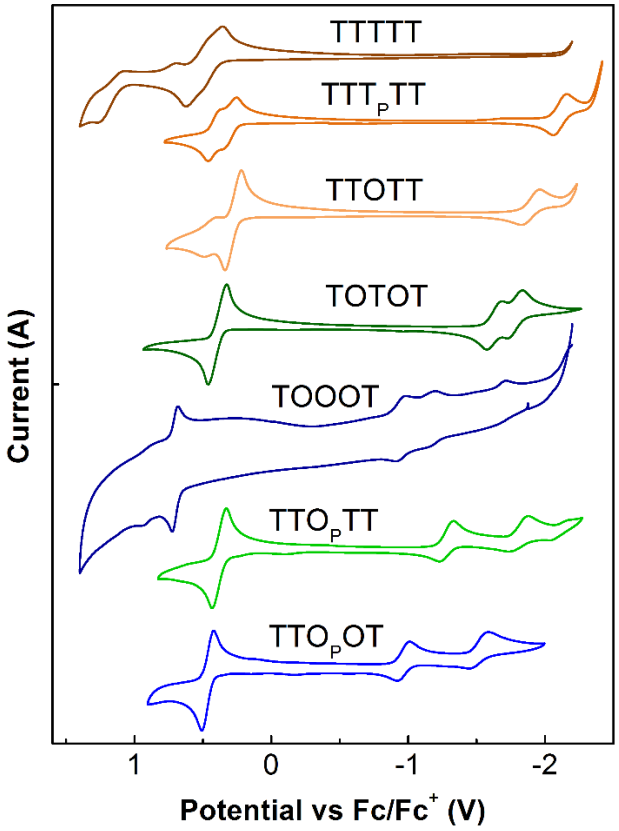

Figure 2.9. Cyclic voltammograms of the thiophene pentamers.

Comparing TTOTT, TOTOT and TOOOT, it is evident that increasing the number of 'O' units in the pentamers lowers both the HOMO and LUMO. However, the red shift in absorbance onset occurs because the LUMO energy is lowered by a much larger magnitude, since the LUMO is largely determined by acceptor strength in donor-acceptor systems.[49,50] This trend agrees well with our previous report showing that the LUMO energy decreases as thiophene-1,1-dioxide oligomer length increases while the HOMO energy remains largely unaffected.[21] Our results show the modularity of the T/O oligomer systems: HOMO-LUMO gaps can be tuned by length, but

should a fixed length be desired, then the gap can be adjusted controllably via the number of thiophene-1,1-dioxide units.

Correlating the electrochemistry results with the single-molecule measurements indicates that it is mainly the shift in the LUMO that dictates the conducting orbital in these systems. In all cases, the HOMO is nearly constant, between -5.0 and -5.2 eV, with the exception of TOOOT, at -5.4 eV. The compounds with a high LUMO (TTTTT, TTT_PTT, and TTOTT) are predominantly HOMO-conducting, as observed in Figure 2.4a. When the LUMO drops to -3.3 and -3.6 eV (TOTOT, and TTO_PTT, respectively), we observe contributions from both the HOMO and LUMO (mid-gap transport, Figure 2.4b). Finally, at the point where the electron affinity reaches -3.9 eV (in both TOOOT and TTO_POT), the molecules show predominantly LUMO transport (Figure 2.4c).

Here, we are able to experimentally determine the dominant transport channel and can qualitatively gauge the HOMO and LUMO contributions to conductance, albeit under a specific environment (solvent).[51] Thus, we can conclude that the LUMO starts to dominate conductance when its energy reaches somewhere between -3.6 eV (in TTO_PTT) and -3.9 eV (TOOOT and TTO_POT). Interestingly, there is a greater increase of conductance with increasing positive bias in TTO_POT compared to TOOOT. This could be because the HOMO of the former is higher and therefore contributes more to conductance than in the latter case. For all our molecules, even though the HOMO and LUMO are close to the gold E_F, we do not observe any crossing of molecular resonances at the voltages applied, since this would have led to charging effects, which alter the slope of the conductance versus bias plots.[27]

2.4 Conclusions

In conclusion, we have shown that the conducting orbitals of thiophene oligomers of an equal length can be tuned by varying the electron affinity of the units. Efficient chemical modification using strong electron withdrawing groups yields dramatic changes in the electronic structure, especially the conductance properties, in contrast to what has been observed in other molecular wires.[17,18] We demonstrate that an increase in the number of thiophene-1,1-dioxide units in the backbone causes a shift in the conducting orbital from HOMO to LUMO. The modified STM break-junction technique described here also enables the characterization of the HOMO and LUMO contributions to conductance, in contrast to previously-used thermopower measurements.[21] The ability to tune the electron affinity across such a wide range of energies within a family of molecules of a fixed length is important in understanding how to engineer molecular materials with tunable transport characteristics.

2.5 Experimental

UV-Vis spectra were recorded on a Shimadzu UV-1800 spectrophotometer with chloroform as the solvent. ^{1}H-NMR and ^{13}C-NMR were recorded on either a Bruker Avance III 400 (400MHz) or Avance III 500 (500MHz) spectrometer, in chloroform solution (residual solvent peak at δ = 7.26ppm) unless stated otherwise. Mass spectra were obtained at the Columbia University mass spectrometry facility using a JEOL JMSHX110A/110A tandem mass spectrometer.

Cyclic voltammetry was performed using single cell setup with a CH Instruments Electrochemical analyser potentiostat. The set up consisted of: a) platinum working electrode, b) platinum wire counter electrode, and c) Ag/AgCl reference electrode, all purchased from BASi. All measurements were carried out in dichloromethane solution containing 0.1 M of supporting

electrolyte, tetrabutylammoniumhexafluorophosphate ($TBAPF_6$), with ~1mg/mL of the desired compound. Oxidation and reduction potentials of the samples were referenced to the ferrocene / ferrocenium (Fc/Fc^+) redox system to obtain the HOMO and LUMO levels (details in section 3). A scan rate of $0.2Vs^{-1}$ was used throughout.

Using Figure 2.9 above, the reduction and oxidation onsets for the thiophene pentamers were obtained. These were converted to HOMO and LUMO levels by calibrating against the redox potential of ferrocene/ferrocenium (Fc/Fc^+), which is assumed to have an absolute energy level at -4.80eV relative to vacuum.[52] The following formulae were used:

$$\textbf{HOMO} = -e(E_{onset,Ox} + (-E_{Fc})) \text{ (eV)} \qquad \textbf{LUMO} = -e(E_{onset,Red} + (-E_{Fc})) \text{ (eV)}$$

The HOMO and LUMO values obtained from the onset of oxidation and reduction respectively are summarized in Table 1.

Table 1. Reduction and oxidation onsets (versus Fc/Fc^+) of the thiophene pentamers, along with the electrochemical and optical band gaps (taken from absorption onset).

Compound	Oxidation Onset (V)	Reduction Onset (V)	HOMO (eV)	LUMO (eV)	$E_{g,elec}$ (eV)	$E_{g,opt}$ (eV)
TTTTT	0.36	-	-5.2	-2.7*	-	2.5
TTT_PTT	0.24	-2.04	-5.0	-2.8	2.2	2.3
TTOTT	0.25	-1.80	-5.0	-3.0	2.0	2.1
TOTOT	0.35	-1.55	-5.2	-3.3	1.9	2.0
TOOOT	0.64	-0.87	-5.4	-3.9	1.5	1.8
TTO_PTT	0.33	-1.21	-5.1	-3.6	1.5	1.7
TTO_POT	0.42	-0.90	-5.2	-3.9	1.3	1.5

*LUMO of T5 was estimated by adding the optical gap to the HOMO.

2.6 Synthetic details

In this section, we describe the procedures used to synthesize the molecules in this chapter. To synthesize the various thiophene dioxides, we used Rozen's Reagent, HOF. The general procedure for the oxidation of thiophenes by HOF has been detailed elsewhere.[53,54] Briefly, a mixture of 20% F_2 in N_2 (commercially available) is bubbled through a mixture of acetonitrile and water (10:1 ratio, between 33-66mL) at -15°C for 2-3h. An aliquot of the resulting HOF solution is reacted with a saturated KI solution and the liberated iodine is titrated with 0.1M sodium thiosulfate solution to determine the concentration, which is usually between 0.15 to 0.40M.

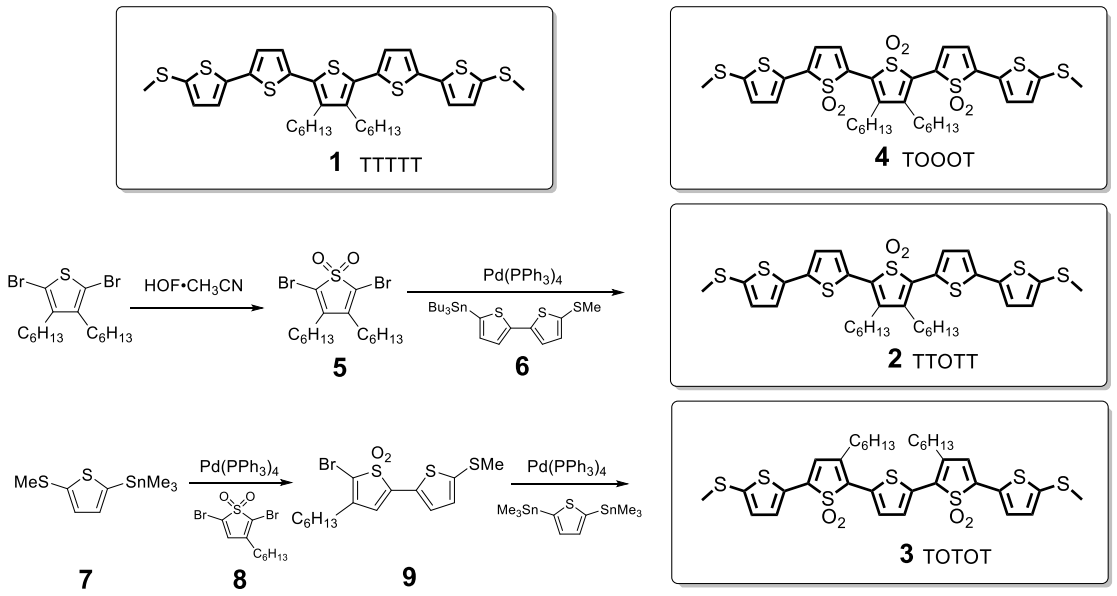

Figure 2.10. Full structures of all unsubstituted TDO-containing pentamers showing alkyl chains and synthetic routes to TTOTT and TOTOT.

Compounds **1**[20], **4**[21], **6**[20] and **8**[53,55] in Figure 2.10 were synthesized as previously reported. All other unlabeled compounds were commercially available. All palladium coupling and lithiation reactions were done in oven-dried glassware using dry solvents from a solvent still.

Compound 5 (*2,5-dibromo-3,4-dihexylthiophene-1,1-dioxide*)

This compound has been previously prepared using mCPBA as the oxidant.[56] Here we use Rozen's reagent. A solution of 2,5-dibromo-3,4-dihexylthiophene (138mg, 0.34mmol, 1eq) in DCM (15mL) was cooled to 0°C and a freshly prepared solution of $HOF{\cdot}CH_3CN$ (0.16M, 8.4mL, 1.35mmol, 4eq) was added dropwise. The reaction was allowed to warm to room temperature and stirred overnight, then quenched with saturated sodium bicarbonate solution. The mixture was extracted twice with DCM and the organic layer was washed with water and dried over $MgSO_4$. The crude product was purified by column chromatography (silica gel, 5% ethyl acetate in hexanes as eluent) to yield the product as a pale yellow oil (130mg, 87%). ^{1}H-NMR (300MHz, $CDCl_3$) δ 2.39 (t, 4H), 1.62-1.24 (m, 16H), 0.91 (t, 6H).

Compound 2 (TTOTT)

Compound **5** (26mg, 0.06mmol, 1eq), compound **6** (58mg, 0.12mmol, 2eq) and $Pd(PPh_3)_4$ (3.3mg, 0.0029mmol, 5%eq) were added to a sealed reaction vial which was evacuated and refilled with nitrogen. Dry DMF (2ml) was added and the solution was stirred at 80°C for 12h. The solution was subsequently poured into water and extracted with ether. The organic extracts were dried with $MgSO_4$. The solvent was removed and the crude product purified by column chromatography (silica gel, 50% DCM in hexanes as eluent) to yield a burgundy powder (25mg, 60%). ^{1}H-NMR (500MHz, $CDCl_3$) δ 7.63 (d, *J* = 4.0 Hz, 2H), 7.18 (d, *J* = 4.0 Hz, 2H), 7.09 (d, *J* = 3.7 Hz, 2H), 7.00 (d, *J* = 3.7 Hz, 2H), 2.68 (t, *J* = 8.3 Hz, 4H), 2.54 (s, 6H), 1.67-1.58 (m, 4H), 1.42-1.20 (m, 12H), 0.93 (t, 6H). ^{13}C-NMR (125MHz, $CDCl_3$) δ 139.55, 138.25, 138.07, 136.96, 131.44, 130.18,

129.73, 127.55, 124.78, 124.41, 31.34, 29.63, 28.51, 27.19, 22.55, 21.86, 14.05. HRMS (ESI+) Calculated for $C_{34}H_{40}O_2NaS_7$: 727.0971; Observed: 727.0973.

Compound 7 (*2-methylthio-5-trimethylstannylthiophene)*

2-(methylthio)thiophene (8.14g, 62.5mmol, 1eq) was placed in a schlenk flask which was evacuated and refilled with nitrogen. Dry THF (30mL) was added and the solution was cooled to -78°C. n-Butyl lithium (2.5M in hexanes, 26.3mL, 65.7mmol, 1.05eq) was added dropwise and the solution was stirred for 1h at -78°C, then half an hour at 0°C. The solution was cooled again to -78°C and trimethyltin chloride (13.1g, 65.7mmol, 1.05eq) was added in one portion and the reaction was allowed to warm to room temperature overnight. 5mL of water was then added to quench the reaction and the volatile solvents were removed. The residue was dissolved in DCM, washed with water and dried over $MgSO_4$. The solvent was removed and the product was obtained as a dark brown oil (17.8g, 97%). The crude product was used without further purification. ^{1}H-NMR (400MHz, $CDCl_3$) δ 7.15 (d, *J* = 3.2 Hz, 1H), 7.05 (d, *J* = 3.2 Hz, 1H), 2.50 (s, 3H) 0.36 (s, 9H). ^{13}C-NMR (125MHz, $CDCl_3$) δ 142.37, 141.18, 135.49, 131.37, 22.00, -8.22. HRMS (ASAP+) Calculated for $C_8H_{14}S_2Sn$: 293.9559; Observed: 293.9557.

Compound 9 (*5-bromo-4-hexyl-5'-(methylthio)-[2,2'-bithiophene] 1,1-dioxide)*

Compound **7** (573mg, 1.95mmol, 1eq), compound **8** (700mg, 1.95mmol, 1eq) and $Pd(PPh_3)_4$ (113mg, 5% eq) were placed in a sealed reaction vial which was evacuated and refilled with nitrogen. Dry toluene (10mL) was added and the reaction was stirred at 95°C for 2h. The solvent was removed and the residue was dissolved in DCM, washed with water and dried over $MgSO_4$.

After removal of solvent, the crude product was purified by column chromatography (silica gel, 50% DCM in hexanes as eluent). The product was isolated as a yellow oil (405mg, 51%). ^{1}H-NMR (400MHz, $CDCl_3$) δ 7.47 (d, *J* = 3.9 Hz, 1H), 6.98 (d, *J* = 3.9 Hz, 1H), 6.51 (s, 1H), 2.56 (s, 3H), 2.41(t, 2H), 1.62-1.53 (s, 2H), 1.42-1.26 (s, 6H), 0.90 (t, 3H). ^{13}C-NMR (125MHz, $CDCl_3$) δ 143.46, 141.80, 137.20, 129.80, 129.58, 119.45, 113.31, 31.43, 30.02, 28.84, 26.42, 22.46, 20.61, 14.02. HRMS (ASAP+) Calculated for $C_{15}H_{20}O_2S_3Br$: 406.9809; Observed: 406.9815.

Compound 3 (TOTOT)

Compound **9** (179mg, 0.44mmol, 2.3eq), 2,5-bis(trimethylstannyl)thiophene (78mg, 0.19mmol, 1eq) and $Pd(PPh_3)_4$ (11mg, 5% eq) were placed in a sealed reaction vial which was evacuated and refilled with nitrogen. Dry toluene (7mL) was added and the reaction was stirred at 110°C for 24h. The solvent was removed and the residue was dissolved in DCM, washed with water and dried over $MgSO_4$. After removal of solvent, the crude product was purified by column chromatography (silica gel, 80% DCM in hexanes as eluent). The product was isolated as a dark purple solid (73mg, 52%). ^{1}H-NMR (400MHz, $CDCl_3$) δ 7.69 (s, 2H), 7.51 (d, *J* = 3.9 Hz, 2H), 7.01 (d, *J* = 3.9 Hz, 2H), 6.59 (s, 2H), 2.67 (t, 4H), 2.57 (s, 6H), 1.66 (m, 4H), 1.51-1.39 (m, 4H), 1.38-1.28 (m, 8H), 0.91 (t, 6H). ^{13}C-NMR (125MHz, $CDCl_3$) δ 143.43, 137.05, 135.81, 130.91, 129.67, 129.14, 129.03, 128.95, 121.07, 31.57, 30.62, 29.37, 27.42, 22.55, 20.66, 14.07. HRMS (ESI+) Calculated for $C_{34}H_{41}O_4S_7$: 737.1050; Observed: 737.1028.

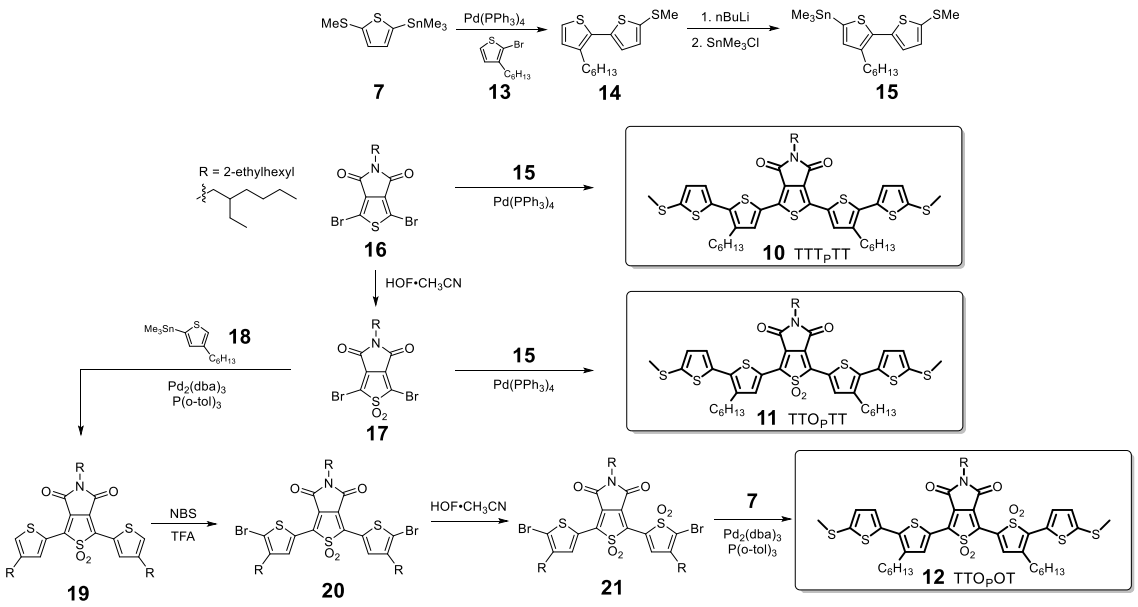

Figure 2.11. Synthesis of pentamers bearing the thienopyrrolodione unit.

Compounds **13**[57], **16**[58], and **18**[57] in Figure 2.11 were synthesized as previously reported. All other unlabeled compounds were commercially available. All palladium coupling and lithiation reactions were done in oven-dried glassware using dry solvents from a solvent still.

Compound 14 (*3-hexyl-5'-(methylthio)-2,2'-bithiophene)*

Compound **7** (2.53g, 8.67mmol, 1.02eq), compound **13** (2.10g, 8.50mmol, 1eq) and $Pd(PPh_3)_4$ (491mg, 5% eq) were placed in a sealed reaction vial which was evacuated and refilled with nitrogen. Dry toluene (30mL) was added and the reaction was stirred at 110°C for 24h. The solvent was removed and the residue was dissolved in DCM, washed with water and dried over $MgSO_4$. After removal of solvent, the crude product was purified by column chromatography (silica gel, hexanes as eluent). The product was isolated as a yellow oil (1.80g, 71%). ^{1}H-NMR (400MHz, $CDCl_3$) δ 7.16 (d, *J* = 5.2 Hz, 1H), 7.02 (d, *J* = 3.7 Hz, 1H), 6.94 (d, *J* = 3.7 Hz, 1H), 6.92 (d, *J* = 5.2 Hz, 1H), 2.73 (t, *J* = 7.6 Hz, 2H), 2.52 (s, 3H), 1.62 (m, 2H), 1.40 – 1.26 (m, 6H), 0.88 (t, 3H).

^{13}C-NMR (125MHz, $CDCl_3$) δ 139.84, 138.65, 136.81, 131.44, 130.28, 130.00, 126.05, 123.89, 31.68, 30.71, 29.22, 29.19, 22.64, 22.21, 14.13. HRMS (ASAP+) Calculated for $C_{15}H_{21}S_3$: 297.0805; Observed: 297.0808.

Compound 15 (*3-hexyl-5-trimethylstannyl-5'-(methylthio)-2,2'-bithiophene)*

Compound 14 (1.55g, 5.25mmol, 1eq) was placed in a schlenk flask which was evacuated and refilled with nitrogen. Dry THF (20mL) was added and the solution was cooled to -78°C. n-Butyl lithium (2.5M in hexanes, 2.20mL, 5.51mmol, 1.05eq) was added dropwise and the solution was stirred for 1h at -0°C. The solution was cooled again to -78°C and trimethyltin chloride (1.10g, 5.51mmol, 1.05eq) was added in one portion and the reaction was allowed to warm to room temperature overnight. 5mL of water was then added to quench the reaction and the volatile solvents were removed. The residue was dissolved in DCM, washed with water and dried over $MgSO_4$. The solvent was removed and the product was obtained as a dark brown oil (2.06g, 86%). The crude product was used for subsequent steps without further purification. ^{1}H-NMR (400MHz, $CDCl_3$) δ 7.02 (d, J = 3.7 Hz, 1H), 6.98 (s, 1H), 6.93 (d, J = 3.7 Hz, 1H), 2.74 (t, 2H), 2.51 (s, 3H), 1.63 (m, 2H), 1.44 – 1.25 (m, 6H), 0.89 (t, 3H), 0.37 (s, 9H). ^{13}C-NMR (125 MHz, $CDCl_3$) δ 140.96, 139.05, 138.29, 136.70, 136.46, 135.98, 131.49, 125.56, 31.66, 30.82, 29.35, 29.12, 22.62, 22.20, 14.09, -8.23. HRMS (ASAP+) Calculated for $C_{18}H_{29}S_3Sn$: 461.0453; Observed: 461.0448.

Compound 11 (TTT_PTT)

Compound **16** (150mg, 0.354mmol, 1eq), compound **15** (374mg, 0.815mmol, 2.3eq) and $Pd(PPh_3)_4$ (20.5mg, 5% eq) were placed in a sealed reaction vial which was evacuated and refilled

with nitrogen. Dry toluene (2mL) was added and the reaction was stirred at 110°C for 24h. The solvent was removed and the residue was dissolved in DCM, washed with water and dried over $MgSO_4$. After removal of solvent, the crude product was purified by column chromatography (silica gel, 50% chloroform in hexanes as eluent). The product was isolated as a red solid (146mg, 48%). ^{1}H-NMR (400MHz, $CDCl_3$) δ 7.84 (s, 2H), 7.05 (d, J = 3.8 Hz, 2H), 7.03 (d, J = 3.7 Hz, 2H), 3.56 (d, J = 7.4 Hz, 2H), 2.76 (t, 4H), 2.54 (s, 6H), 1.88 (m, 1H), 1.68 (m, 4H), 1.46 – 1.24 (m, 20H), 0.90 (t, 12H). ^{13}C-NMR (125MHz, $CDCl_3$) δ 162.87, 140.95, 138.52, 137.11, 135.89, 134.13, 132.83, 131.05, 130.03, 128.35, 126.77, 42.66, 38.16, 31.63, 30.56, 30.48, 29.42, 29.24, 28.56, 23.88, 23.09, 22.64, 21.91, 14.10, 10.49. HRMS (ASAP+) Calculated for $C_{44}H_{56}NO_2S_7$: 854.2356; Observed: 854.2352.

Compound 17 (Oxidized *1,3-dibromo-5-(2-ethylhexyl)-4H-thieno[3,4-c]pyrrole-4,6(5H)-dione)*

A solution of compound **16** (970mg, 2.29mmol, 1eq) in DCM (15mL) was cooled to 0°C and a freshly prepared solution of $HOF{\cdot}CH_3CN$ (0.66M, 21mL, 13.8mmol, 6eq) was added dropwise. The reaction was allowed to warm to room temperature and stirred overnight, then quenched with saturated sodium bicarbonate solution. The mixture was extracted twice with DCM and the organic layer was washed with water and dried over $MgSO_4$. The crude product was purified by column chromatography (silica gel, 50% DCM in hexanes as eluent) to yield the product as a pale, off-white solid (438mg, 42%). ^{1}H-NMR (400MHz, $CDCl_3$) δ 3.61 (d, J = 8.8 Hz, 2H), 1.80 (m, 1H), 1.40 – 1.20 (m, 8H), 0.92 (m, 6H). ^{13}C-NMR (125 MHz, $CDCl_3$) δ 159.56, 127.06, 119.86, 44.04, 38.12, 30.52, 28.41, 23.86, 22.89, 14.04, 10.27. HRMS (ASAP+) Calculated for $C_{14}H_{18}NO_4SBr_2$: 453.9303; Observed: 453.9313.

Compound 10 (TTO_PTT)

Compound **17** (75mg, 0.165mmol, 1eq), compound **15** (167mg, 0.363mmol, 2.2eq) and $Pd(PPh_3)_4$ (9.5mg, 5% eq) were placed in a sealed reaction vial which was evacuated and refilled with nitrogen. Dry toluene (7mL) was added and the reaction was stirred at 110°C for 24h. The solvent was removed and the residue was dissolved in chloroform, washed with water and dried over $MgSO_4$. After removal of solvent, the crude product was purified by column chromatography (silica gel, 30% chloroform in hexanes as eluent). The product was isolated as a dark blue solid (36mg, 25%). ^{1}H-NMR (400MHz, $CDCl_3$) δ 8.02 (s, 2H), 7.22 (d, J = 3.8 Hz, 2H), 7.04 (d, J = 3.8 Hz, 2H), 3.66 (d, J = 7.4 Hz, 2H), 2.83 (m, 4H), 2.57 (s, 6H), 1.91 (m, 1H), 1.71 (m, 4H), 1.51 – 1.20 (m, 20H), 0.91 (m, 12H). ^{13}C-NMR (125MHz, $CDCl_3$) δ 163.06, 141.45, 141.20, 140.96, 136.73, 136.07, 133.67, 130.50, 128.09, 125.53, 114.92, 43.57, 38.08, 31.57, 30.57, 30.20, 29.42, 29.21, 28.50, 23.91, 23.03, 22.61, 21.48, 14.07, 10.41. HRMS (ESI+) Calculated for $C_{44}H_{55}NO_4S_7$: 908.2074; Observed: 908.2094.

Compound 19

Compound **18** (299mg, 0.905mmol, 2.3eq), $Pd_2(dba)_3$ (18mg, 5% eq) and $P(o\text{-}tol)_3$ (12mg, 10% eq) were placed in a sealed reaction vial which was evacuated and refilled with nitrogen. Separately, compound **17** was dissolved in dry chlorobenzene (5mL) under nitrogen. This solution of compound **17** was transferred to the reaction vial via syringe and the reaction was stirred at 120°C for 24h. The solvent was removed and the residue was dissolved in chloroform, washed with water and dried over $MgSO_4$. After removal of solvent, the crude product was purified by column chromatography (silica gel, 30% dichloromethane in hexanes as eluent). The product was

isolated as a viscous red liquid (172mg, 69%). ^{1}H-NMR (500MHz, $CDCl_3$) δ 8.06 (d, J = 1.2 Hz, 2H), 7.42 (d, J = 1.0 Hz, 2H), 3.66 (d, J = 7.4, 2H), 2.69 (t, 4H), 1.89 (m, 1H), 1.67 (m, 4H), 1.43 – 1.21 (m, 20H), 0.98 – 0.82 (m, 12H). ^{13}C-NMR (125MHz, CDCl3) δ 162.88, 145.70, 134.94, 134.80, 130.69, 127.52, 115.34, 43.54, 38.10, 31.59, 30.58, 30.34, 30.15, 28.91, 28.48, 23.93, 23.00, 22.58, 14.06, 10.40. HRMS (ASAP+) Calculated for $C_{34}H_{48}NO_4S_3$: 630.2745; Observed: 630.2756.

Compound 20

Compound **19** (172mg, 0.273mmol, 1eq) was dissolved in a mixture of trifluoroacetic acid (15mL) and chloroform (15mL). The solution was protected from light and N-bromosuccinimide (102mg, 0.573mmol, 2.1eq) was added portion-wise over 1h. The reaction was stirred overnight and water was subsequently added to quench it. The organic layer was extracted with chloroform, washed with water and dried over $MgSO_4$. The crude product was purified by column chromatography (silica gel, 30% dichloromethane in hexanes as eluent) to yield a red viscous liquid (206mg, 96%). ^{1}H-NMR (500MHz, $CDCl_3$) δ 7.82 (s, 2H), 3.64 (d, J = 7.3 Hz, 2H), 2.64 (t, 4H), 1.87 (m, 1H), 1.64 (m, 4H), 1.45 – 1.20 (m, 20H), 0.99 – 0.82 (m, 12H). ^{13}C-NMR (125MHz, CDCl3) δ 162.85, 144.81, 134.12, 133.45, 127.68, 122.02, 115.45, 43.64, 38.16, 31.51, 30.60, 29.49, 29.43, 28.88, 28.50, 23.93, 23.00, 22.57, 14.05, 10.38. HRMS (ASAP+) Calculated for $C_{34}H_{46}NO_4S_3Br_2$: 788.0937; Observed: 788.0936.

Compound 21

A solution of compound **20** (206mg, 0.262mmol, 1eq) in chloroform (3mL) was cooled to 0°C and a freshly prepared solution of HOF·CH_3CN (0.47M, 4.5mL, 2.09mmol, 8eq) was added dropwise. The reaction was allowed to warm to room temperature and stirred overnight, then quenched with saturated sodium bicarbonate solution. The mixture was extracted twice with DCM and the organic layer was washed with water and dried over $MgSO_4$. The crude product was purified by column chromatography (silica gel, 60% DCM in hexanes as eluent) to yield the product as a red solid (7mg, 3%). ^{1}H-NMR (500MHz, $CDCl_3$) δ 7.89 (s, 1H), 7.72 (s, 1H), 3.65 (d, J = 7.4 Hz, 2H), 2.64 (t, 2H), 2.48 (t, 2H), 1.89 (m, 1H), 1.62 (m, 4H), 1.45 – 1.15 (m, 20H), 0.98 – 0.79 (m, 12H). ^{13}C-NMR (125MHz, CDCl3) δ 162.39, 160.92, 145.60, 140.21, 136.03, 136.00, 135.40, 130.59, 127.59, 125.82, 125.35, 124.47, 121.28, 114.61, 44.04, 38.02, 31.48, 31.38, 30.52, 29.76, 29.71, 29.44, 29.41, 28.85, 28.39, 26.45, 23.87, 23.00, 22.55, 22.45, 14.04, 10.30. HRMS (ESI+) Calculated for $C_{34}H_{45}Br_2NO_6S_3Na$: 842.0655; Observed: 842.0601.

Compound 12 (TTO_POT)

Compound **21** (7mg, 0.00854mmol, 1eq), compound **7** (5.7mg, 0.0196mmol, 2.3eq), $Pd_2(dba)_3$ (0.39mg, 5% eq) and P(o-tol)$_3$ (0.26mg, 10% eq) were placed in a sealed reaction vial which was evacuated and refilled with nitrogen. Dry chlorobenzene (3mL) was added and the reaction was stirred at 120°C for 24h. The solvent was removed and the residue was purified by preparative TLC (silica gel, 75% DCM in hexanes) to yield the product as a dark blue solid (4mg, 51%). ^{1}H-NMR (500MHz, CD_2Cl_2) δ 8.08 (s, 1H), 7.96 (s, 1H), 7.72 (d, J = 4.0 Hz, 1H), 7.30 (d, J = 3.8 Hz, 1H), 7.11 (d, J = 3.9 Hz, 1H), 7.07 (d, J = 3.9 Hz, 1H), 3.64 (d, J = 7.3 Hz, 2H), 2.86 (t, 2H), 2.73

(t, 2H), 2.65 (s, 3H), 2.59 (s, 3H), 1.86 (m, 1H), 1.71 (m, 4H), 1.53 – 1.18 (m, 20H), 0.99 – 0.79 (m, 12H). ^{13}C-NMR (125MHz, CD_2Cl_2) δ 162.59, 161.60, 147.09, 143.50, 142.37, 142.03, 138.34, 135.57, 135.44, 134.21, 132.10, 131.58, 130.02, 128.98, 128.65, 128.44, 128.30, 126.02, 125.27, 122.91, 114.47, 43.64, 38.18, 31.54, 31.49, 30.54, 30.19, 30.06, 29.68, 29.39, 29.21, 29.13, 28.48, 27.29, 23.89, 23.00, 22.58, 22.51, 20.97, 19.95, 13.81, 10.15. HRMS (ESI+) Calculated for $C_{44}H_{55}NO_6S_7Na$: 940.1972; Observed: 940.1969.

2.7 Acknowledgements

This work was supported primarily by the National Science Foundation grant DMR-1507440. J. Z. Low thanks the A*STAR Graduate Academy in Singapore for a graduate fellowship.

2.8 References

(1) Low, J. Z.; Capozzi, B.; Cui, J.; Wei, S.; Venkataraman, L.; Campos, L. M. *Chemical Science* **2017**, *8*, 3254-3259.

(2) Tao, N. J. *Nat. Nanotechnol.* **2006**, *1*, 173-181.

(3) Sun, L.; Diaz-Fernandez, Y. A.; Gschneidtner, T. A.; Westerlund, F.; Lara-Avila, S.; Moth-Poulsen, K. *Chem. Soc. Rev.* **2014**, *43*, 7378-7411.

(4) Yuen, J. D.; Wudl, F. *Energy Environ. Sci.* **2013**, *6*, 392-406.

(5) Zhong, Y.; Kumar, B.; Oh, S.; Trinh, M. T.; Wu, Y.; Elbert, K.; Li, P.; Zhu, X.; Xiao, S.; Ng, F.; Steigerwald, M. L.; Nuckolls, C. *J. Am. Chem. Soc.* **2014**, *136*, 8122-8130.

(6) Yamashita, Y.; Hinkel, F.; Marszalek, T.; Zajaczkowski, W.; Pisula, W.; Baumgarten, M.; Matsui, H.; Müllen, K.; Takeya, J. *Chem. Mater.* **2016**, *28*, 420-424.

(7) Jongwan, C.; Heeseok, S.; Nakjoong, K.; Felix Sunjoo, K. *Semicond. Sci. Technol.* **2015**, *30*, 064002.

(8) Yuen, J. D.; Fan, J.; Seifter, J.; Lim, B.; Hufschmid, R.; Heeger, A. J.; Wudl, F. *J. Am. Chem. Soc.* **2011**, *133*, 20799-20807.

(9) Meng, Q.; Hu, W. *Phys. Chem. Chem. Phys.* **2012**, *14*, 14152-14164.

(10) Gao, X.; Hu, Y. *J. Mater. Chem. C* **2014**, *2*, 3099-3117.

(11) Stalder, R.; Puniredd, S. R.; Hansen, M. R.; Koldemir, U.; Grand, C.; Zajaczkowski, W.; Müllen, K.; Pisula, W.; Reynolds, J. R. *Chem. Mater.* **2016**, *28*, 1286-1297.

(12) Klauk, H. *Chem. Soc. Rev.* **2010**, *39*, 2643-2666.

(13) Nielsen, C. B.; Turbiez, M.; McCulloch, I. *Adv. Mater.* **2013**, *25*, 1859-1880.

(14) Sirringhaus, H. *Adv. Mater.* **2014**, *26*, 1319-1335.

(15) Quek, S. Y.; Kamenetska, M.; Steigerwald, M. L.; Choi, H. J.; Louie, S. G.; Hybertsen, M. S.; Neaton, J. B.; Venkataraman, L. *Nat. Nanotechnol.* **2009**, *4*, 230-234.

(16) Venkataraman, L.; Park, Y. S.; Whalley, A. C.; Nuckolls, C.; Hybertsen, M. S.; Steigerwald, M. L. *Nano Lett.* **2007**, *7*, 502-506.

(17) Frisenda, R.; Perrin, M. L.; Valkenier, H.; Hummelen, J. C.; van der Zant, H. S. J. *Phys. Status Solidi B* **2013**, *250*, 2431-2436.

(18) Zhao, X.; Huang, C.; Gulcur, M.; Batsanov, A. S.; Baghernejad, M.; Hong, W.; Bryce, M. R.; Wandlowski, T. *Chem. Mater.* **2013**, *25*, 4340-4347.

(19) Ie, Y.; Endou, M.; Lee, S. K.; Yamada, R.; Tada, H.; Aso, Y. *Angew. Chem., Int. Ed.* **2011**, *50*, 11980-11984.

(20) Capozzi, B.; Dell, E. J.; Berkelbach, T. C.; Reichman, D. R.; Venkataraman, L.; Campos, L. M. *J. Am. Chem. Soc.* **2014**, *136*, 10486-10492.

(21) Dell, E. J.; Capozzi, B.; Xia, J.; Venkataraman, L.; Campos, L. M. *Nat. Chem.* **2015**, *7*, 209-214.

(22) Capozzi, B.; Xia, J.; Adak, O.; Dell, E. J.; Liu, Z.-F.; Taylor, J. C.; Neaton, J. B.; Campos, L. M.; Venkataraman, L. *Nat. Nanotechnol.* **2015**, *10*, 522-527.

(23) Xiang, L.; Hines, T.; Palma, J. L.; Lu, X.; Mujica, V.; Ratner, M. A.; Zhou, G.; Tao, N. *J. Am. Chem. Soc.* **2016**, *138*, 679-687.

(24) Leary, E.; Höbenreich, H.; Higgins, S. J.; van Zalinge, H.; Haiss, W.; Nichols, R. J.; Finch, C. M.; Grace, I.; Lambert, C. J.; McGrath, R.; Smerdon, J. *Phys. Rev. Lett.* **2009**, *102*, 086801.

(25) Yamada, R.; Kumazawa, H.; Noutoshi, T.; Tanaka, S.; Tada, H. *Nano Lett.* **2008**, *8*, 1237-1240.

(26) Lee, S. K.; Yamada, R.; Tanaka, S.; Chang, G. S.; Asai, Y.; Tada, H. *ACS Nano* **2012**, *6*, 5078-5082.

(27) Capozzi, B.; Low, J. Z.; Xia, J.; Liu, Z.-F.; Neaton, J. B.; Campos, L. M.; Venkataraman, L. *Nano Lett.* **2016**, *16*, 3949-3954.

(28) Hoffmann, R. *Angew. Chem., Int. Ed.* **1987**, *26*, 846-878.

(29) Yuan, M.-C.; Chiu, M.-Y.; Liu, S.-P.; Chen, C.-M.; Wei, K.-H. *Macromolecules* **2010**, *43*, 6936-6938.

(30) Zou, Y.; Najari, A.; Berrouard, P.; Beaupré, S.; Réda Aïch, B.; Tao, Y.; Leclerc, M. *J. Am. Chem. Soc.* **2010**, *132*, 5330-5331.

(31) Piliego, C.; Holcombe, T. W.; Douglas, J. D.; Woo, C. H.; Beaujuge, P. M.; Fréchet, J. M. J. *J. Am. Chem. Soc.* **2010**, *132*, 7595-7597.

(32) Su, M.-S.; Kuo, C.-Y.; Yuan, M.-C.; Jeng, U. S.; Su, C.-J.; Wei, K.-H. *Adv. Mater.* **2011**, *23*, 3315-3319.

(33) Amb, C. M.; Chen, S.; Graham, K. R.; Subbiah, J.; Small, C. E.; So, F.; Reynolds, J. R. *J. Am. Chem. Soc.* **2011**, *133*, 10062-10065.

(34) Chu, T.-Y.; Lu, J.; Beaupré, S.; Zhang, Y.; Pouliot, J.-R.; Wakim, S.; Zhou, J.; Leclerc, M.; Li, Z.; Ding, J.; Tao, Y. *J. Am. Chem. Soc.* **2011**, *133*, 4250-4253.

(35) Small, C. E.; Chen, S.; Subbiah, J.; Amb, C. M.; Tsang, S.-W.; Lai, T.-H.; Reynolds, J. R.; So, F. *Nat. Photonics* **2012**, *6*, 115-120.

(36) Jo, J.; Pron, A.; Berrouard, P.; Leong, W. L.; Yuen, J. D.; Moon, J. S.; Leclerc, M.; Heeger, A. J. *Adv. Energy Mater.* **2012**, *2*, 1397-1403.

(37) Amir, E.; Rozen, S. *Angew. Chem., Int. Ed.* **2005**, *44*, 7374-7378.

(38) Rozen, S. *Acc. Chem. Res.* **1996**, *29*, 243-248.

(39) Rozen, S. *Acc. Chem. Res.* **2014**, *47*, 2378-2389.

(40) Dell, E. J.; Campos, L. M. *J. Mater. Chem.* **2012**, *22*, 12945-12952.

(41) Nakayama, J.; Sugihara, Y. In *Organosulfur Chemistry II*; Page, P. C. B., Ed.; Springer: Berlin, Heidelberg, 1999, p 131-195.

(42) Xu, B.; Tao, N. J. *Science* **2003**, *301*, 1221-1223.

(43) Venkataraman, L.; Klare, J. E.; Tam, I. W.; Nuckolls, C.; Hybertsen, M. S.; Steigerwald, M. L. *Nano Lett.* **2006**, *6*, 458-462.

(44) Xia, J.; Capozzi, B.; Wei, S.; Strange, M.; Batra, A.; Moreno, J. R.; Amir, R. J.; Amir, E.; Solomon, G. C.; Venkataraman, L.; Campos, L. M. *Nano Lett.* **2014**, *14*, 2941-2945.

(45) Díez-Pérez, I.; Hihath, J.; Lee, Y.; Yu, L.; Adamska, L.; Kozhushner, M. A.; Oleynik, I. I.; Tao, N. *Nat. Chem.* **2009**, *1*, 635-641.

(46) Hihath, J.; Bruot, C.; Nakamura, H.; Asai, Y.; Díez-Pérez, I.; Lee, Y.; Yu, L.; Tao, N. *ACS Nano* **2011**, *5*, 8331-8339.

(47) Oliva, M. M.; Casado, J.; Navarrete, J. T. L.; Patchkovskii, S.; Goodson, T.; Harpham, M. R.; Seixas de Melo, J. S.; Amir, E.; Rozen, S. *J. Am. Chem. Soc.* **2010**, *132*, 6231-6242.

(48) Duan, C.; Huang, F.; Cao, Y. *J. Mater. Chem.* **2012**, *22*, 10416-10434.

(49) Casey, A.; Dimitrov, S. D.; Shakya-Tuladhar, P.; Fei, Z.; Nguyen, M.; Han, Y.; Anthopoulos, T. D.; Durrant, J. R.; Heeney, M. *Chem. Mater.* **2016**, *28*, 5110-5120.

(50) Kim, B.-G.; Ma, X.; Chen, C.; Ie, Y.; Coir, E. W.; Hashemi, H.; Aso, Y.; Green, P. F.; Kieffer, J.; Kim, J. *Adv. Funct. Mater.* **2013**, *23*, 439-445.

(51) Kotiuga, M.; Darancet, P.; Arroyo, C. R.; Venkataraman, L.; Neaton, J. B. *Nano Lett.* **2015**, *15*, 4498-4503.

(52) You, J.; Dou, L.; Yoshimura, K.; Kato, T.; Ohya, K.; Moriarty, T.; Emery, K.; Chen, C.-C.; Gao, J.; Li, G.; Yang, Y. *Nat. Commun.* **2013**, *4*, 1446.

(53) Amir, E.; Amir, R. J.; Campos, L. M.; Hawker, C. J. *J. Am. Chem. Soc.* **2011**, *133*, 10046-10049.

(54) Wei, S.; Xia, J.; Dell, E. J.; Jiang, Y.; Song, R.; Lee, H.; Rodenbough, P.; Briseno, A. L.; Campos, L. M. *Angew. Chem., Int. Ed.* **2014**, *53*, 1832-1836.

(55) Busby, E.; Xia, J.; Wu, Q.; Low, J. Z.; Song, R.; Miller, J. R.; Zhu, X. Y.; Campos, Luis M.; Sfeir, M. Y. *Nat. Mater.* **2015**, *14*, 426-433.

(56) Barbarella, G.; Favaretto, L.; Sotgiu, G.; Zambianchi, M.; Arbizzani, C.; Bongini, A.; Mastragostino, M. *Chem. Mater.* **1999**, *11*, 2533-2541.

(57) Hagemann, O.; Jørgensen, M.; Krebs, F. C. *J. Org. Chem.* **2006**, *71*, 5546-5559.

(58) Graham, K. R.; Cabanetos, C.; Jahnke, J. P.; Idso, M. N.; El Labban, A.; Ngongang Ndjawa, G. O.; Heumueller, T.; Vandewal, K.; Salleo, A.; Chmelka, B. F.; Amassian, A.; Beaujuge, P. M.; McGehee, M. D. *J. Am. Chem. Soc.* **2014**, *136*, 9608-9618.

3. Highly Conducting Organic Mixed-Valence Molecular Wires

Abstract: Charge transport across molecular wires in the non-resonant, low-bias regime typically decreases exponentially with distance. Much research in the field of single molecule electronics is therefore focused on developing classes of materials that are able to transport charge efficiently even at long distances. Here, we explore the length-dependent transport of mixed-valence compounds. We measure the single molecule conductance of a series of bis(triarylamine) wires in which the two nitrogen centers are bridged by 1-3 phenyl rings. In the neutral state, their conductance shows an exponential decay as the number of phenyls in the backbone increases, as has been demonstrated for a range of systems. By contrast, in an oxidized state, generated by using a one-electron chemical oxidant, we find that all three molecules become highly conducting at a low applied bias; the longest molecule increases in conductance by more than three orders of magnitude. Importantly, in this oxidized mixed-valence radical state, these molecular wires display an increase in conductance with increasing length. Our work thus demonstrates a new class of highly conductive molecular wires, created by utilizing mixed-valence radical cations, that can be used for long range transport.

3.1 Preface

This chapter is based on a manuscript in preparation titled *Highly Conducting Organic Mixed-Valence Molecular Wires* by Xiaodong Yin, Jonathan Z. Low, Suman Gunasekaran, Luis M. Campos and Latha Venkataraman.

3.2 Introduction

The drive to miniaturize electronic components has led to an increased interest in studying the conduction of molecular scale devices in recent years.[1-3] A challenge in the field has been to design molecular wires that can remain highly conductive over long length scales since, in general,

low-bias off-resonant conductance is attenuated exponentially as the wires are made longer. Many design principles have been proposed to create highly conductive molecular backbones such as increasing their antiaromatic character[4-6], utilizing constructive quantum interference effects,[7-12] or even increasing interatom coupling through sigma conjugation.[13] Another less explored strategy is to introduce mixed-valence character into a system. Mixed-valence compounds are molecules that contain two redox centers in different oxidation states. Single molecule conductance studies on mixed-valence inorganic compounds with multiple metal centers suggest that they can be highly conducting due to strong coupling between the metal atoms.[14,15] However, although many organic mixed-valence compounds are known,[16-18] there have been no reports of their length dependent conductance being measured in molecular junctions thus far. This may be due to the difficulty in trapping molecules in the mixed-valence state between electrodes, since organic mixed-valence molecules are by definition open shell radicals.[17]

Here, we work with bis(triarylamines), which are the archetypal organic mixed-valence molecules in their radical cation (1+) oxidation state.[18-22] In these types of molecules, two or more redox-active sites with a conjugated bridge between them behave as a donor-acceptor pair. Indeed, Lambert and Nöll determined that bis(triarylamines) undergo ultrafast photoinduced electron transfer between the two nitrogen atoms separated by up to 2 nm, indicating strong electronic coupling of these atoms.[19] Such strong intramolecular coupling could lead to efficient electron transport. We thus sought to investigate the single molecule conductance of these compounds in their mixed-valence state. We synthesized three bis(triarylamine) molecular wires with phenyl backbones of increasing length (B1-B3) and measured their single molecule conductance using the scanning tunneling microscope break-junction (STM-BJ) method.[23] In the neutral state, the conductance decreased with increasing length, with an exponential decay constant β of ~1.7 per

phenyl (~0.4 $Å^{-1}$), in agreement with what has been observed before.[24,25] In the chemically oxidized radical cation states, all molecular junctions showed an increased conductance. The longest one, B3, showed a 1600-fold increase while B1 showed a 9-fold increase. Remarkably, in the radical cation state, the conductance increased with increasing length yielding a negative β of -0.9 per phenyl (about -0.2 $Å^{-1}$) at a low bias of 45 mV. Our results therefore have important ramifications on the design of highly conductive molecular wires.

3.3 Results and discussion

We first characterize the optoelectronic properties of the thioanisole-terminated bis(triarylamine) wires B1, B2, and B3 (Figure 3.1a) to determine their oxidation potentials so as to select the appropriate chemical oxidant necessary to generate the radical cations for the conductance measurements. These wires were synthesized via the Buchwald-Hartwig cross coupling reaction as detailed in section 3.7.[26,27] Figure 3.1b shows the cyclic voltammograms of B1-B3. All three molecules show stable and reversible oxidation waves at low positive potential, but no reduction waves even when the voltage is swept to -1.8 V. B1 shows two well-resolved oxidation peaks ($E_{1/2}$ = 0.08 and 0.53 V). In B2, the onset of oxidation is higher, and there are also two distinct peaks that appear closer to each other ($E_{1/2}$ = 0.26 and 0.45 V). The two peaks in B1 and B2 correspond to two separate one-electron oxidation waves at each nitrogen redox center. As the number of phenyl rings between the nitrogen atoms increases to three in B3, these two peaks coalesce into one unresolvable 2-electron oxidation peak ($E_{1/2}$ = 0.37 V), implying that the nitrogen centers behave as independent redox entities. The cyclic voltammetry data therefore shows that the coupling between the nitrogen centers decreases with increasing molecular length.[19,21,28]

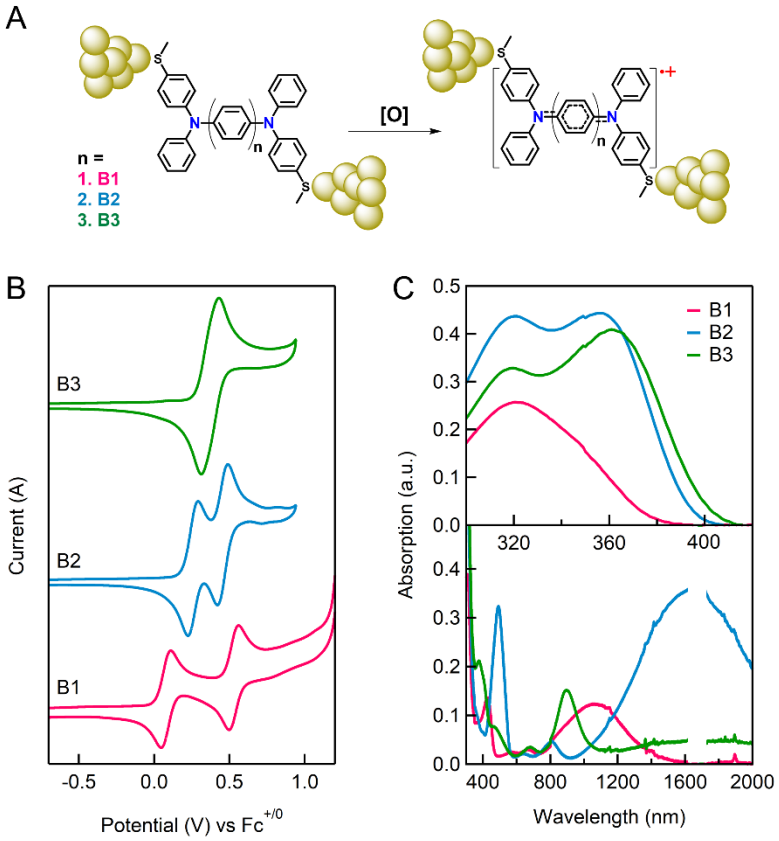

Figure 3.1. (a) Schematic representation showing the structure of the neutral or oxidized bis(triarylamine) wires in the STM break-junction. (b) Cyclic voltammograms showing the oxidation wave of the bis(triarylamine) series. (b) UV-Vis spectra of the molecules in their neutral (top panel) and radical cation (bottom panel) states. The excised region in the bottom panel of (c) is where the detector switches, leading to a spike in the noise.

Next, we use UV-Vis spectroscopy to show that the radical cation and dication states formed through chemical oxidation of the neutral molecules are stable in solution. The top panel of Figure 3.1c shows the absorption spectrum of the neutral molecules in dichloromethane. The absorption onsets fall between 410 nm (3.0 eV) to 380 nm (3.3 eV); molecules with such large optical gaps should show off-resonant transport. To obtain solutions of the oxidized species, we use the oxidant tris(4-bromophenyl)ammoniumyl hexachloroantimonate (BAHA) since it has an oxidizing potential of 0.7 V versus the ferrocene/ferrocenium redox couple (higher than all the oxidation potentials for this series). Upon addition of 1 equivalent of BAHA, low energy

absorption bands with peaks above ~1150 nm appear in all the molecules as shown in Figure 3.1c (bottom panel). These very low energy transitions are due to the intervalence charge transfer bands typical of mixed-valence states in bis(triarylamine) systems.[19,21] The absorption bands of the radical cations are corroborated by time-dependent density functional theory (TD-DFT) as detailed in section 3.6. As one additional equivalent of BAHA is added, there is a slight blue-shift and new bands appear in the 800 – 1200 nm region of all 3 absorption spectra (Figure 3.2), indicative of a transition from the open shell radical cation to the closed-shell dication species. These results show that the oxidation state of the bis(triarylamines) can be controlled through the addition of appropriate equivalents of BAHA. From an experimental perspective, each oxidation state of the molecules yields different colored solutions that are unambiguously identifiable.

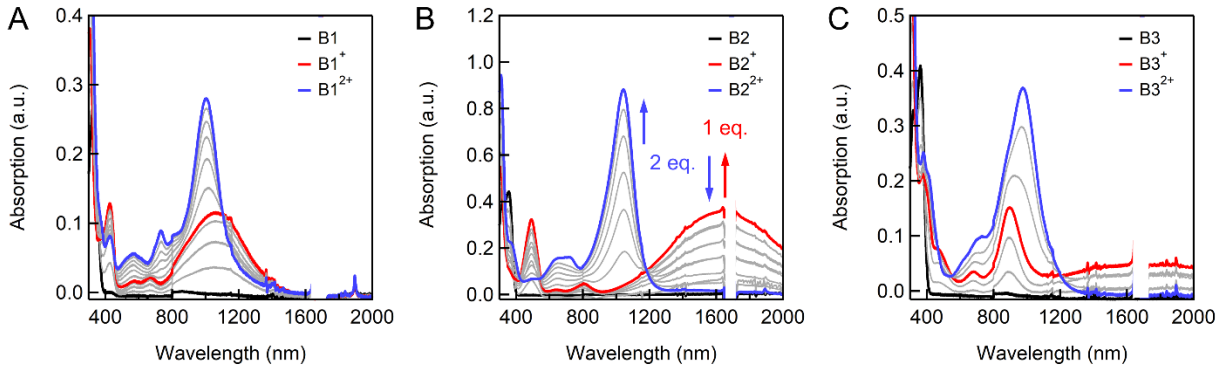

Figure 3.2. UV-Vis plots of oxidative titration of bis(triarylamine) compounds in dichloromethane, with the spectra of the neutral (black), radical cation (red), and dication (blue) compounds highlighted. The blue arrow in (b) shows the direction of peak grown as up to 1 equivalent of BAHA is added, and the red arrow shows peaks that attenuate or grow as the 2nd equivalent of BAHA is added.

We characterize the conductance of single-molecule junctions formed with B1-B3 using the scanning tunneling microscope break junction (STM-BJ) technique.[23] In this method, a gold STM tip is driven into a gold substrate and retracted while the conductance is recorded as a function of the displacement. During the retraction, a gold point-contact is formed with a

conductance close to 1 G_0 (= $2e^2/h$ = 77.48 μS). When this contact is broken in a solution of molecules terminated with gold binding groups such as the thioanisole groups used here, molecular conductance plateaus are observed below 1 G_0. The process is repeated thousands of times, and the individual traces are logarithmically binned without data selection to produce the conductance histograms.

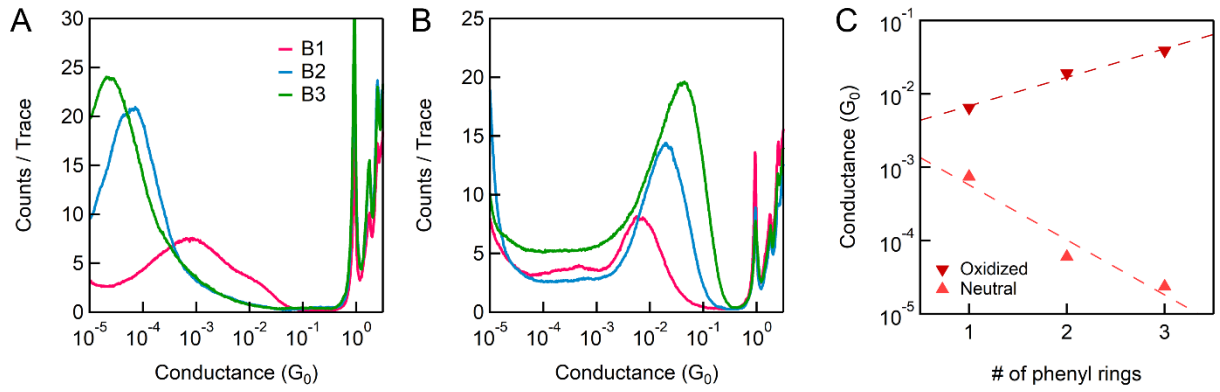

Figure 3.3. (a-b) Conductance histograms of the bis(triarylamine) wires in their (a) neutral and (b) radical cation states in bromonaphthalene measured at a bias of 45 mV. (c) Conductance decay of the molecules with increasing length for both states. The β values in bromonaphthalene are 1.7 and -0.9 per phenyl for the neutral and oxidized series respectively.

Figure 3.3a shows the conductance histograms for B1-B3 measured at a 45 mV bias in bromonaphthalene. All three histograms show clear conductance peaks. The histograms are rather broad due to the conformational freedom in these long molecules and the rotational degrees of freedom of the thioanisole linking groups; these factors yield a conductance that decreases as the molecular junctions are elongated. The conductance plateaus of these molecular junctions are therefore slightly sloped, as seen in the 2D conductance histograms constructed by overlaying all the individual conductance traces (Figure 3.4). Additionally, the histograms of B2 and B3 show only one peak in the histogram, while B1 has a small shoulder at higher conductance which we attribute to the conductance through oxidized molecules. We fit the main peak in B1 and the peaks

in B2 and B3 with a Gaussian to determine their most probable conductance. We see an exponential decrease in conductance as molecular length increases with a decay constant β of ~1.7 per ring or ~0.4 $Å^{-1}$ as shown in Figure 3.3c (see also Figure 3.5 for a description of how molecular length was determined, as well as conductance versus length plots). This decay is in agreement with what has been measured previously for polyphenylene-based molecular junctions.[24,25]

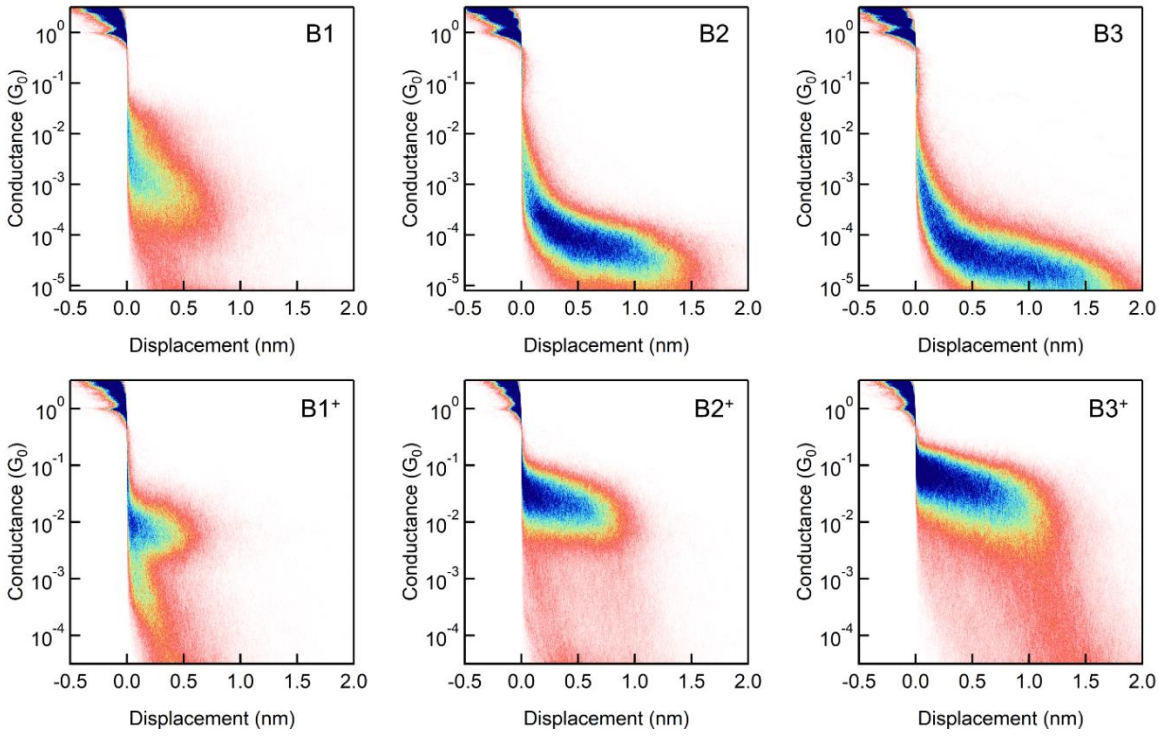

Figure 3.4. 2D conductance histograms of B1-B3 (top row) and $B1^+$ to $B3^+$ (bottom row) in bromonapthhalene.

We next measure the conductance of the radical cation which we generate by adding 1 equivalent of BAHA to the solution of the molecules. Since BAHA is only sparingly soluble in pure bromonaphthalene, we use a 1:3 mixture of dichloromethane and bromonaphthalene as the solvent. Figure 3.3b shows the conductance histograms of the three radical cations recorded at a bias of 45 mV where clear peaks are again visible. These data indicate first that the molecule in the junction retains its oxidation state despite the low bias used in the measurements since the

conductance is clearly different for the two species at the same bias. The histogram of B1 shows a little contribution from the neutral species slightly below 10^{-3} G_0. Across this series of molecular wires, the conductances of the mono-oxidized species are all higher than the neutral species. In particular, B3 goes from ~2.4×10^{-5} G_0 in the neutral state to ~ 4×10^{-2} G_0 in the radical cation state – a 1600-fold increase in conductance. We note further that 4×10^{-2} G_0 is an exceptionally high conductance for a molecule that is ~2.6 nm in length, especially considering the low bias used in the measurements.[24,25,29-31] This high conductance is not a result of gold binding directly to the amines, as control measurements with an analogous molecule that has only one thioanisole anchor does not show any molecular conductance signature (Figure 3.6). The key result in our measurement of the oxidized bis(triarylamines) is that the conductance increases with increasing length, resulting in a negative β of ~-0.9 per phenyl ring or around -0.2 $Å^{-1}$ (Figure 3.3c). This result is not solvent dependent. The negative β of the oxidized bis(triarylamines) is retained when the measurements are performed in trichlorobenzene instead, albeit at a slightly lower value of around -0.4 per phenyl likely due to a solvent gating effect (Figure 3.7).

While several groups have reported low β values of 0.1 $Å^{-1}$ or less before,[31-35] a negative β system is unexpected. Furthermore, the magnitude of negative β for bis(triarylamines) reported herein is large. To rationalize these findings, we first note that the transport across radical cations could be very close to or in the resonant transport regime; an exponential decrease in conductance with increasing length (positive β values) are expected only for an off-resonant tunneling model.[36] Second, the oxidation of the molecules introduces radical states that lie close to the Fermi level of gold. Since the second oxidation potential gets lower with increasing length, these states are likely to get closer to the Fermi level as the wires are made longer. Such an enhancement of conductance by radical states has been observed experimentally before.[37,38]

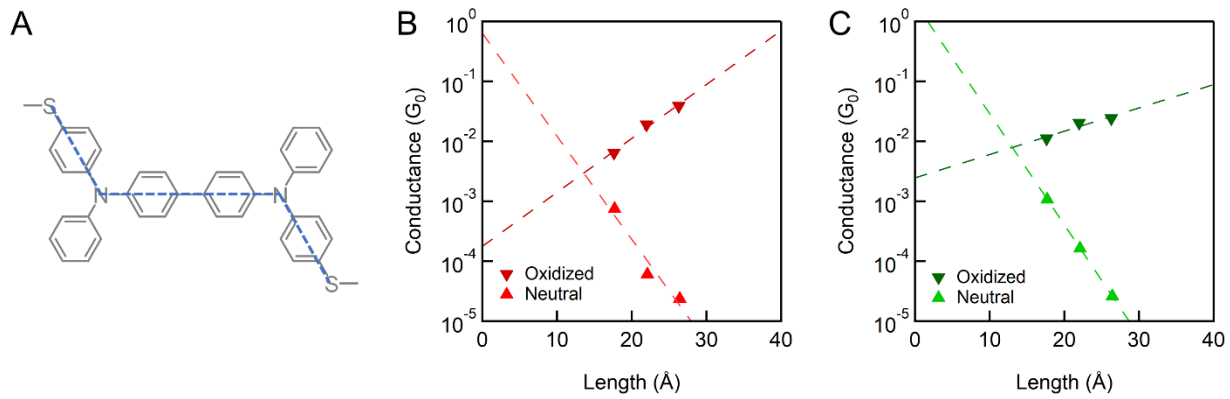

Figure 3.5. (a) Scheme depicting how the sulfur-sulfur length was determined for B2. The lengths were obtained from DFT optimized structures. (b) Conductance decay with molecular length for measurements in bromonaphthalene. β is ~0.40 and ~-0.21 Å^{-1} for the neutral and oxidized species respectively. (c) Conductance decay with molecular length for measurements in trichlorobenzene. β is ~0.43 and ~-0.09 Å^{-1} for the neutral and oxidized species respectively.

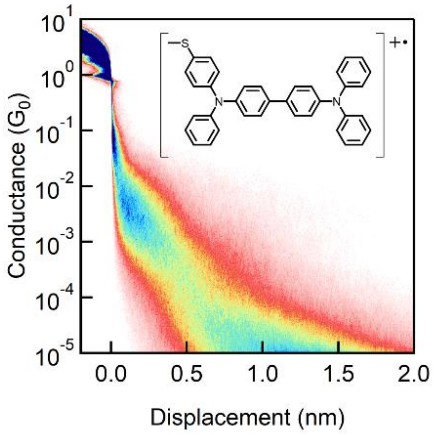

Figure 3.6. 2D conductance histogram of mono-B2, that shows no clear molecular peak.

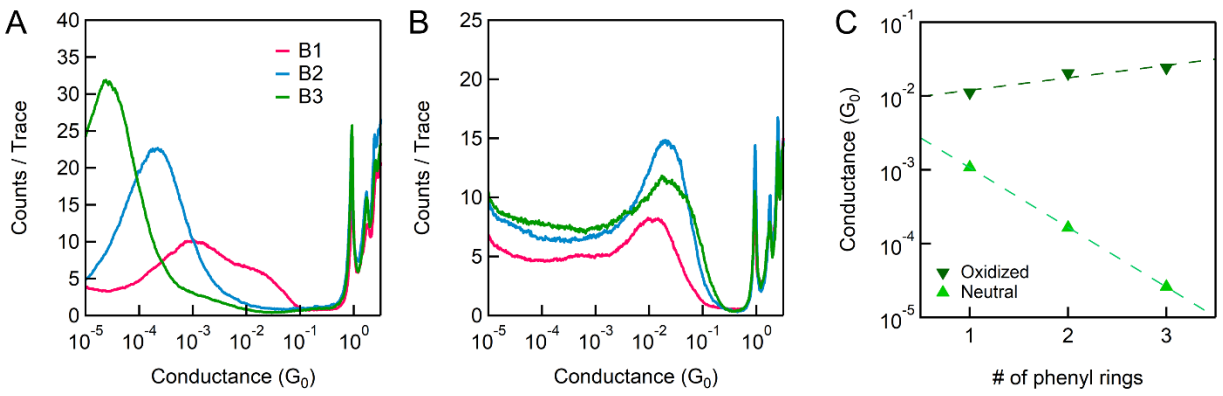

Figure 3.7. (a-b) Conductance histograms of the bis(triarylamine) wires in their (a) neutral state at 90 mV and (b) radical cation state at 45 mV in trichlorobenzene. A larger bias was used for the measurement of the neutral molecules since the histogram peak of B3 at 45 mV was obscured by the noise floor. (c) Conductance decay of the molecules with increasing length for both states. The β values in trichlorobenzene are 1.9 and -0.4 per phenyl for the neutral and oxidized series respectively.

3.4 Conclusions

In conclusion, we report a straightforward method to generate the mixed-valence states of a series of bis(triarylamine) molecular wires and measure their single molecule conductance. These mixed-valence states, which are radical cations, display remarkably high conductance for their length. Moreover, we find that the conductance of the molecules increases with increasing length, with a high negative β of ~-0.9 per phenyl ring. While it remains to be seen whether the high conductance and negative β are a general feature of organic mixed-valence molecular wires, the approach we describe will hopefully encourage more research into this class of compounds for applications in the molecular electronics field.

3.5 General experimental

All reactions and manipulations were carried out under an atmosphere of pre-purified nitrogen or argon using Schlenk techniques. All solvents used for experiments were purified using a solvent purification system. All reagents used in the experiments were purchased from Sigma-

Aldrich, and directly used without purification. 4-(methylthio)-*N*-phenylaniline was prepared according to literature.[39]

^{1}H-NMR were recorded on a Bruker Avance III 400 (400 MHz) and ^{13}C-NMR were recorded on a Bruker Avance III 500 (500 MHz) spectrometer, in acetone-d6 (residual solvent peak at δ = 2.05 ppm for ^{1}H-NMR, and at δ = 29.84, 206.13 ppm for ^{13}C-NMR).

Mass spectra were obtained at the Columbia University mass spectrometry facility using a XEVO G2-XS Waters® equipped with a QTOF detector with multiple inlet and ionization capabilities including electrospray ionization (ESI), atmospheric pressure chemical ionization (APCI), and atmospheric solids analysis probe (ASAP). The base peaks were usually obtained as $[M]^+$ or $[M+H]^+$ ions.

UV-Vis absorption data were acquired on a Varian Cary 5000 UV-Vis/NIR spectrophotometer. Cyclic voltammograms (CVs) were recorded on a CHI 66 electrochemical workstation using Pt plate electrode as working electrode, Pt wire as counter electrode, and Ag/AgCl electrode as the reference electrode at room temperature.

Oxidative titration of the bis(triarylamine) compounds was conducted in solutions of dichloromethane with concentrations of 7×10^{-6} M for B1, and 1×10^{-5} M for both B2 and B3. 3 mL of these solutions were placed in a UV-Vis cuvette and the one electron oxidant tris(4-bromophenyl)ammoniumyl hexachloroantimonate (BAHA) was added in several steps. The concentration of BAHA solution was 5×10^{-4} M in dichloromethane. Therefore, 42 μL of BAHA corresponds to 1 eq of oxidant for B1, and 60 μL of BAHA corresponds to 1 eq of oxidant of B2 and B3.

3.6 Calculation of UV-vis spectra of cations

Time-dependent DFT (TD-DFT) was conducted at B3LYP/6-311+G** level of theory based on the optimized structures using Gaussian09.[40] TD-DFT gives the relative oscillator strengths of the excited state absorptions in order to corroborate the UV-Vis spectra obtained experimentally.

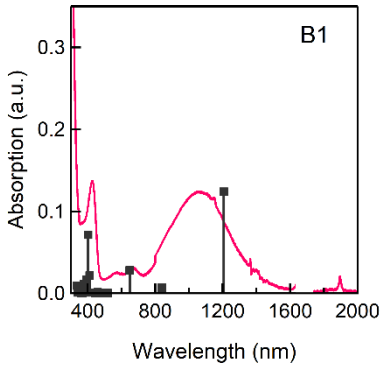

Figure 3.8. UV-Vis spectra of the B1 radical cation in DCM shown with drop lines from TD-DFT.

Excited state transitions of B1 with oscillator strength (f) higher than 0.01:

λ (nm)	Oscillator strength f	Assignment	Probability	λ (nm)	Oscillator strength f	Assignment	Probability
1206.65	f=0.4784	132B→133B	0.740	377.00	f=0.0441	132A→137A	0.092
839.46	f=0.0260	131B→133B	0.986			133A→134A	0.064
648.70	f=0.1079	130B→133B	0.970			133A→136A	0.325
411.25	f=0.0835	133A→134A	0.062			131B→135B	0.048
		133A→135A	0.115			132B→137B	0.142
		133A→136A	0.027	340.01	f=0.0259	132A→134A	0.197
		124B→133B	0.702			132A→139A	0.022
		132B→137B	0.014			133A→137A	0.032
401.08	f=0.2758	132A→137A	0.018			133A→138A	0.292
		132A→142A	0.023			132B→134B	0.360
		133A→134A	0.326			132B→139B	0.019
		133A→135A	0.290				
		124B→133B	0.226				
392.63	f=0.0633	133A→134A	0.461				
		133A→135A	0.428				

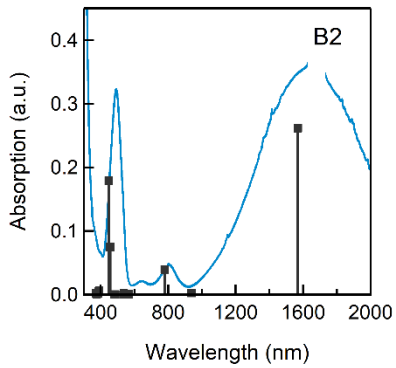

Figure 3.9. UV-Vis spectra of the B2 radical cation in DCM shown with drop lines from TD-DFT.

Excited state transitions of B2 with oscillator strength (f) higher than 0.01:

λ (nm)	Oscillator strength f	Assignment	Probability	λ (nm)	Oscillator strength f	Assignment	Probability
1567.70	f=0.6987	153A→154A	0.010	448.13	f=0.4772	153A→154A	0.646
		152B→153B	0.988			143B→153B	0.190
779.80	f=0.1059	150B→153B	0.981	389.93	f=0.0156	152A→157A	0.144
455.50	f=0.1988	151A→154A	0.012			153A→158A	0.189
		153A→154A	0.175			151B→154B	0.064
		143B→153B	0.749			152B→157B	0.223
		144B→153B	0.020				

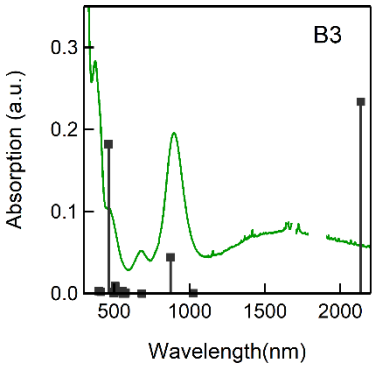

Figure 3.10. UV-Vis spectra of the B3 radical cation in DCM shown with drop lines from TD-DFT.

Excited state transitions of B3 with oscillator strength (f) higher than 0.01:

λ (nm)	Oscillator strength f	Assignment	Probability	λ (nm)	Oscillator strength f	Assignment	Probability
2133.96	f=0.7349	172B→173B	0.415	(399.10)	(f=0.0103)	172A→177A	0.025
874.38	f=0.1381	170B→173B	0.988			172A→179A	0.070
507.26	f=0.0285	162B→173B	0.106			173A→175A	0.054
		163B→173B	0.784			173A→178A	0.110
		166B→173B	0.090			173A→185A	0.014
464.23	f=0.5719	171A→174A	0.064			159B→173B	0.039
		173A→174A	0.705			171B→174B	0.057
		171B→174B	0.056			171B→178B	0.018
399.10	f=0.0103	171A→174A	0.034			172B→176B	0.148
		171A→178A	0.012			172B→177B	0.066

3.7 Synthetic details

N,N'-bis(4-(methylthio)phenyl)-N,N'-diphenylbenzene-1,4-diamine (B1)

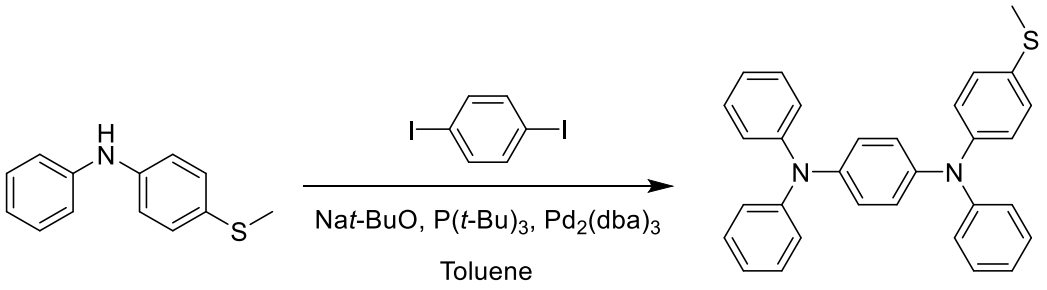

Figure 3.11. Synthetic scheme of B1.

4-(methylthio)-*N*-phenylaniline (96mg, 0.45mmol), 1,4-diiodobenzene (74mg, 0.22mmol), and sodium *t*-butoxide (64mg, 0.67mmol) were charged into a 25mL Schlenk tube and 10mL toluene was added. After stirring 10 min under argon atmosphere, tri-*t*-butylphosphine (1M, 0.02mL) and tris(dibenzylideneacetone)dipalladium(0) (12mg, 0.013mmol) were added into the mixture in one portion. This mixture was kept stirring for 5h at room temperature, then washed with water and brine. The remaining organic phase was dried over sodium sulfate and all volatile components were removed on a rotary evaporator. Purification by column chromatography (silica gel, 25%

DCM in hexanes as eluent) gave the product as white solid (60mg, 0.16mmol, 72%). ^{1}H-NMR (400 MHz, Acetone-d6) δ 7.28 (dd, *J* = 8.5, 7.4 Hz, 4H), 7.25 – 7.20 (m, 4H), 7.06 (dd, *J* = 8.6, 1.0 Hz, 4H), 7.04 – 6.98 (m, 10H), 2.46 (s, 6H). ^{13}C-NMR (125 MHz, Acetone-d6) δ 148.64, 146.39, 143.81, 132.74, 130.22, 129.18, 126.27, 125.18, 124.35, 123.51, 16.47. HRMS [M+H^{+}] $C_{32}H_{29}N_2S_2$ Calculated: 505.1772; Found: 505.1776.

N,N'-bis(4-(methylthio)phenyl)-N,N'-diphenyl-[1,1'-biphenyl]-4,4'-diamine (B2)

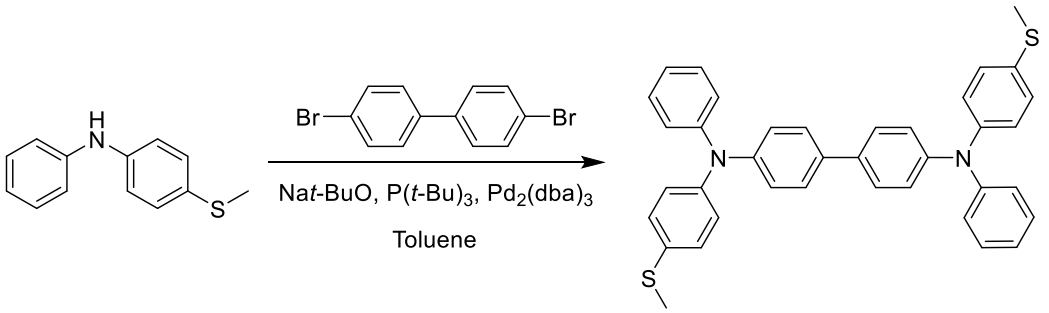

Figure 3.12. Synthetic scheme of B2.

4-(methylthio)-*N*-phenylaniline (200mg, 0.93 mmol), 4,4'-dibromo-1,1'-biphenyl (145mg, 0.46mmol), and sodium *t*-butoxide (134mg, 1.4 mmol) were charged into a 25mL Schlenk tube and 10mL toluene was added. After stirring 10 min under argon atmosphere, tri-*t*-butylphosphine (1M, 0.028mL) and tris(dibenzylideneacetone)dipalladium(0) (25mg, 0.028mmol) were added into the mixture in one portion. This mixture was kept stirring for 5h at room temperature then washed with water and brine. The remaining organic phase was dried over sodium sulfate, and all volatile components were removed on a rotary evaporator. Purification by column chromatography (silica gel, 25% DCM in hexanes as eluent) gave the product as white solid (150mg, 0.26mmol, 56.5%). ^{1}H-NMR (500 MHz, Acetone-d6) δ 7.60 – 7.55 (m, 4H), 7.32 (dd, *J* = 8.3, 7.5 Hz, 4H), 7.28 – 7.23 (m, 4H), 7.11 – 7.02 (m, 14H), 2.48 (s, 6H). ^{13}C-NMR (125 MHz, Acetone-d6) δ

147.58, 146.72, 145.24, 134.56, 132.48, 129.42, 128.19, 127.22, 124.92, 124.11, 123.73, 123.07, 15.46. HRMS [M+H$^+$] $C_{38}H_{33}N_2S_2$ Calculated: 581.2085; Found: 581.2084.

N,N'-bis(4-(methylthio)phenyl)-N,N'-diphenyl-[1,1':4',1''-terphenyl]-4,4''-diamine (B3)

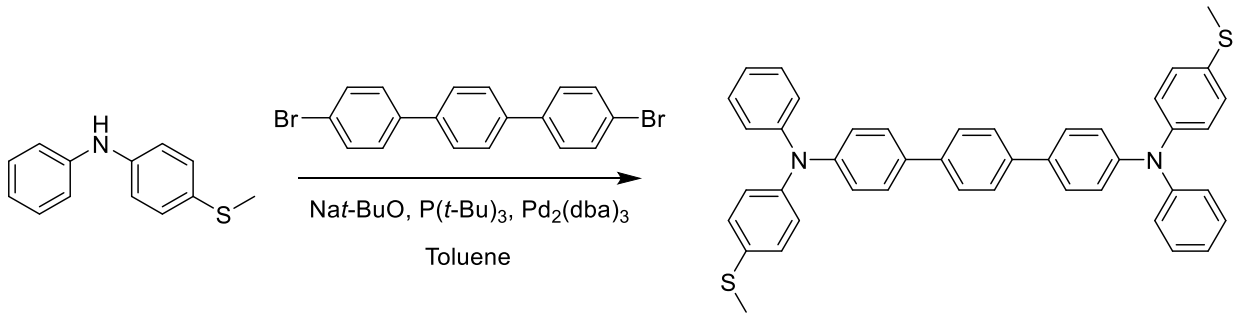

Figure 3.13. Synthetic scheme of B3.

4-(methylthio)-*N*-phenylaniline (200mg, 0.93mmol), 4,4"-dibromo-1,1':4',1"-terphenyl (180mg, 0.46mmol), and sodium *t*-butoxide (134mg, 1.4mmol) were charged into a 25mL Schlenk tube and 10mL toluene was added. After stirring 10 min under argon atmosphere, tri-*t*-butylphosphine (1M, 0.028 mL) and tris(dibenzylideneacetone)dipalladium(0) (25mg, 0.028mmol) were added into the mixture in one portion. This mixture was stirred for 5h at room temperature, then washed with water and brine. The remaining organic phase was dried over sodium sulfate, and all volatile components were removed on a rotary evaporator. Purification by column chromatography (silica gel, 25% DCM in hexanes as eluent) gave the product as white solid (180mg, 0.273 mmol, 59.5%). ^{1}H-NMR (400 MHz, Acetone-d6) δ 7.74 (s, 4H), 7.69 – 7.62 (m, 4H), 7.33 (dd, *J* = 8.5, 7.4 Hz, 4H), 7.30 – 7.24 (m, 4H), 7.16 – 7.02 (m, 14H), 2.49 (s, 6H). ^{13}C-NMR (125 MHz, Acetone-d6) δ 148.44, 148.08, 146.08, 139.70, 135.27, 133.54, 130.35, 129.08, 128.38, 127.66, 125.96, 125.15, 124.46, 124.09, 16.33. HRMS [M+H$^+$] $C_{44}H_{37}N_2S_2$ Calculated: 657.2398; Found: 657.2391.

N-(4-(methylthio)phenyl)-N,N',N'-triphenyl-[1,1'-biphenyl]-4,4'-diamine (B2-mono)

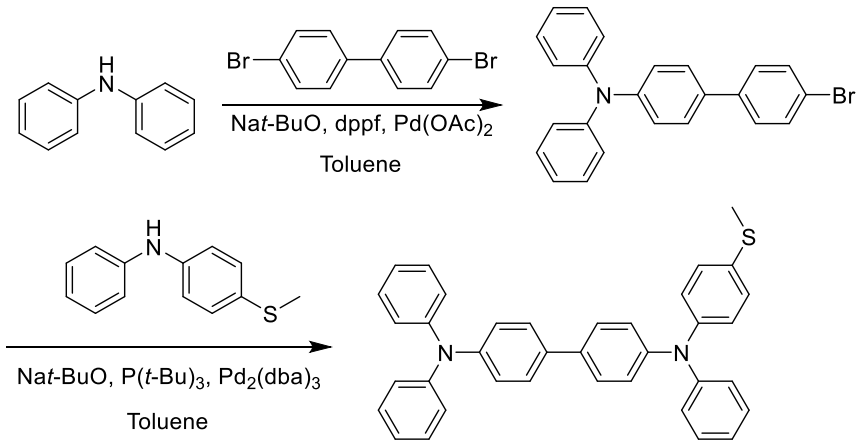

Figure 3.14. Synthetic scheme of B2-mono.

4'-bromo-*N*,*N*-diphenylbiphenyl-4-amine was synthesized according to literature starting from 4,4'-dibromobiphenyl and diphenylamine, with $Pd(OAc)_2$, 1,1'-bis(diphenyphosphino)ferrocene (dppf), and sodium tert-butoxide.[41] 4'-bromo-*N*,*N*-diphenylbiphenyl-4-amine (78mg, 0.2mmol) and 4-(methylthio)-*N*-phenylaniline (50mg, 0.23mmol) was dissolved in 10mL dry toluene in a 25mL Schlenk tube. Sodium *t*-butoxide (25mg, 0.25mmol) was added into the flask under nitrogen atmosphere and the mixture was stirred for 20 min. Then, tri-*t*-butylphosphine (0.2M, 20μL) and tris(dibenzylideneacetone)dipalladium(0) (5mg, 0.004mmol) were added into the mixture in one portion. This mixture was kept stirring for 5h at room temperature, then washed with water and brine. The remaining organic phase was dried over sodium sulfate, and all volatile components were removed on a rotary evaporator. Purification by column chromatography (silica gel, 25% DCM in hexanes as eluent) gave the product as white solid (85mg, 0.16mmol, 80%). ^{1}H-NMR (400 MHz, Methylene Chloride-d_2) δ 7.46 (d, J = 8.8 Hz, 4H), 7.31 – 7.23 (m, 6H), 7.19 (d, J = 8.6 Hz, 2H), 7.14 – 7.07 (m, 10H), 7.07 – 7.00 (m, 5H), 2.46 (s, 3H). ^{13}C-NMR (125 MHz, Methylene Chloride-d_2) δ 147.92, 147.74, 147.03, 146.81, 145.55, 134.90, 134.79, 132.23, 129.44,

128.51, 127.38, 125.07, 124.50, 124.35, 124.19, 124.08, 123.08, 16.71. HRMS [M+H$^+$] $C_{37}H_{31}N_2S$ Calculated: 535.2208; Found: 535.2214.

3.8 Acknowledgements

J.Z.L. thanks the A*STAR Graduate Academy in Singapore for a graduate fellowship.

We thank Brandon Fowler for mass spectrometry.

3.9 References

(1) Chen, F.; Hihath, J.; Zhifeng, H.; Li, X.; Tao, N. J. *Annu. Rev. Phys. Chem.* **2007**, *58*, 535-564.

(2) Xiang, D.; Wang, X.; Jia, C.; Lee, T.; Guo, X. *Chem. Rev.* **2016**, *116*, 4318-4440.

(3) Nichols, R. J.; Higgins, S. J. *Annu. Rev. Anal. Chem.* **2015**, *8*, 389-417.

(4) Chen, W.; Li, H.; Widawsky, J. R.; Appayee, C.; Venkataraman, L.; Breslow, R. *J. Am. Chem. Soc.* **2014**, *136*, 918-920.

(5) Fujii, S.; Marqués-González, S.; Shin, J.-Y.; Shinokubo, H.; Masuda, T.; Nishino, T.; Arasu, N. P.; Vázquez, H.; Kiguchi, M. *Nat. Commun.* **2017**, *8*, 15984.

(6) Yin, X.; Zang, Y.; Zhu, L.; Low, J. Z.; Liu, Z.-F.; Cui, J.; Neaton, J. B.; Venkataraman, L.; Campos, L. M. *Sci. Adv.* **2017**, *3*.

(7) Markussen, T.; Stadler, R.; Thygesen, K. S. *Nano Lett.* **2010**, *10*, 4260-4265.

(8) Guédon, C. M.; Valkenier, H.; Markussen, T.; Thygesen, K. S.; Hummelen, J. C.; van der Molen, S. J. *Nat. Nanotechnol.* **2012**, *7*, 305.

(9) Arroyo, C. R.; Tarkuc, S.; Frisenda, R.; Seldenthuis, J. S.; Woerde, C. H. M.; Eelkema, R.; Grozema, F. C.; van der Zant, H. S. J. *Angew. Chem., Int. Ed.* **2013**, *52*, 3152-3155.

(10) Pedersen, K. G. L.; Borges, A.; Hedegård, P.; Solomon, G. C.; Strange, M. *J. Phys. Chem. C* **2015**, *119*, 26919-26924.

(11) Yoshizawa, K.; Tada, T.; Staykov, A. *J. Am. Chem. Soc.* **2008**, *130*, 9406-9413.

(12) Tada, T.; Yoshizawa, K. *Phys. Chem. Chem. Phys.* **2015**, *17*, 32099-32110.

(13) Su, T. A.; Li, H.; Klausen, R. S.; Kim, N. T.; Neupane, M.; Leighton, J. L.; Steigerwald, M. L.; Venkataraman, L.; Nuckolls, C. *Acc. Chem. Res.* **2017**, *50*, 1088-1095.

(14) Liu, I. P. C.; Bénard, M.; Hasanov, H.; Chen, I. W. P.; Tseng, W. H.; Fu, M. D.; Rohmer, M. M.; Chen, C. h.; Lee, G. H.; Peng, S. M. *Chem. - Eur. J.* **2007**, *13*, 8667-8677.

(15) Chen, C.-P.; Luo, W.-R.; Chen, C.-N.; Wu, S.-M.; Hsieh, S.; Chiang, C.-M.; Dong, T.-Y. *Langmuir* **2013**, *29*, 3106-3115.

(16) Hankache, J.; Wenger, O. S. *Chem. Rev.* **2011**, *111*, 5138-5178.

(17) Heckmann, A.; Lambert, C. *Angew. Chem., Int. Ed.* **2012**, *51*, 326-392.

(18) Launay, J.-P. *Chem. Soc. Rev.* **2001**, *30*, 386-397.

(19) Lambert, C.; Nöll, G. *J. Am. Chem. Soc.* **1999**, *121*, 8434-8442.

(20) Nelsen, S. F. *Chem. - Eur. J.* **2000**, *6*, 581-588.

(21) Low, P. J.; Paterson, M. A. J.; Puschmann, H.; Goeta, A. E.; Howard, J. A. K.; Lambert, C.; Cherryman, J. C.; Tackley, D. R.; Leeming, S.; Brown, B. *Chem. - Eur. J.* **2003**, *10*, 83-91.

(22) Coropceanu, V.; Gruhn, N. E.; Barlow, S.; Lambert, C.; Durivage, J. C.; Bill, T. G.; Nöll, G.; Marder, S. R.; Brédas, J.-L. *J. Am. Chem. Soc.* **2004**, *126*, 2727-2731.

(23) Xu, B.; Tao, N. J. *Science* **2003**, *301*, 1221-1223.

(24) Zang, Y.; Pinkard, A.; Liu, Z.-F.; Neaton, J. B.; Steigerwald, M. L.; Roy, X.; Venkataraman, L. *J. Am. Chem. Soc.* **2017**, *139*, 14845-14848.

(25) Venkataraman, L.; Klare, J. E.; Nuckolls, C.; Hybertsen, M. S.; Steigerwald, M. L. *Nature* **2006**, *442*, 904-907.

(26) Li, T.; Tan, G.; Shao, D.; Li, J.; Zhang, Z.; Song, Y.; Sui, Y.; Chen, S.; Fang, Y.; Wang, X. *J. Am. Chem. Soc.* **2016**, *138*, 10092-10095.

(27) Su, Y.; Wang, X.; Wang, L.; Zhang, Z.; Wang, X.; Song, Y.; Power, P. P. *Chem. Sci.* **2016**, *7*, 6514-6518.

(28) Richardson, D. E.; Taube, H. *Inorg. Chem.* **1981**, *20*, 1278-1285.

(29) Lu, Q.; Liu, K.; Zhang, H.; Du, Z.; Wang, X.; Wang, F. *ACS Nano* **2009**, *3*, 3861-3868.

(30) Chen, I. W. P.; Fu, M.-D.; Tseng, W.-H.; Chen, C.-h.; Chou, C.-M.; Luh, T.-Y. *Chem. Commun.* **2007**, 3074-3076.

(31) Kolivoška, V.; Valášek, M.; Gál, M.; Sokolová, R.; Bulíčková, J.; Pospíšil, L.; Mészáros, G.; Hromadová, M. *J. Phys. Chem. Lett.* **2013**, *4*, 589-595.

(32) Xing, Y.; Park, T.-H.; Venkatramani, R.; Keinan, S.; Beratan, D. N.; Therien, M. J.; Borguet, E. *J. Am. Chem. Soc.* **2010**, *132*, 7946-7956.

(33) Yamada, R.; Kumazawa, H.; Noutoshi, T.; Tanaka, S.; Tada, H. *Nano Lett.* **2008**, *8*, 1237-1240.

(34) Sedghi, G.; Sawada, K.; Esdaile, L. J.; Hoffmann, M.; Anderson, H. L.; Bethell, D.; Haiss, W.; Higgins, S. J.; Nichols, R. J. *J. Am. Chem. Soc.* **2008**, *130*, 8582-8583.

(35) Wang, C.; Batsanov, A. S.; Bryce, M. R.; Martín, S.; Nichols, R. J.; Higgins, S. J.; García-Suárez, V. M.; Lambert, C. J. *J. Am. Chem. Soc.* **2009**, *131*, 15647-15654.

(36) Choi, S. H.; Frisbie, C. D. In *Charge and Exciton Transport through Molecular Wires*; Siebbeles, L. D. A., Grozema Ferdinand, C., Eds.; Wiley: Weinheim, Germany, 2011, p 61-91.

(37) Yuan, L.; Franco, C.; Crivillers, N.; Mas-Torrent, M.; Cao, L.; Sangeeth, C. S. S.; Rovira, C.; Veciana, J.; Nijhuis, C. A. *Nat. Commun.* **2016**, *7*, 12066.

(38) Liu, J.; Zhao, X.; Al-Galiby, Q.; Huang, X.; Zheng, J.; Li, R.; Huang, C.; Yang, Y.; Shi, J.; Manrique, D. Z.; Lambert, C. J.; Bryce, M. R.; Hong, W. *Angew. Chem., Int. Ed.* **2017**, *56*, 13061-13065.

(39) Madrid, P. B.; Polgar, W. E.; Toll, L.; Tanga, M. J. *Bioorg. Med. Chem. Lett.* **2007**, *17*, 3014-3017.

(40) Frisch, M. J.; Trucks, G. W.; Schlegel, H. B.; Scuseria, G. E.; Robb, M. A.; Cheeseman, J. R.; Scalmani, G.; Barone, V.; Mennucci, B.; Petersson, G. A.; Nakatsuji, H.; Caricato, M.; Li, X.; Hratchian, H. P.; Izmaylov, A. F.; Bloino, J.; Zheng, G.; Sonnenberg, J. L.; Hada, M.; Ehara, M.; Toyota, K.; Fukuda, R.; Hasegawa, J.; Ishida, M.; Nakajima, T.; Honda, Y.; Kitao, O.; Nakai, H.; Vreven, T.; Montgomery, J. A.; Peralta, J. E.; Ogliaro, F.; Bearpark, M.; Heyd, J. J.; Brothers, E.; Kudin, K. N.; Staroverov, V. N.; Kobayashi, R.; Normand, J.; Raghavachari, K.; Rendell, A.; Burant, J. C.; Iyengar, S. S.; Tomasi, J.; Cossi, M.; Rega, N.; Millam, J. M.; Klene, M.; Knox, J. E.; Cross, J. B.; Bakken, V.; Adamo, C.; Jaramillo, J.; Gomperts, R.; Stratmann, R. E.; Yazyev, O.; Austin, A. J.; Cammi, R.; Pomelli, C.; Ochterski, J. W.; Martin, R. L.; Morokuma, K.; Zakrzewski, V. G.; Voth, G. A.; Salvador, P.; Dannenberg, J. J.; Dapprich, S.; Daniels, A. D.; Farkas; Foresman, J. B.; Ortiz, J. V.; Cioslowski, J.; Fox, D. J. Gaussian 09, Revision D.01, Gaussian, Inc., Wallingford CT, 2009.

(41) Chen, Z.; Liu, X.-K.; Zheng, C.-J.; Ye, J.; Liu, C.-L.; Li, F.; Ou, X.-M.; Lee, C.-S.; Zhang, X.-H. *Chem. Mater.* **2015**, *27*, 5206-5211.

4. The Anomalous Behavior of the Blatter Radical at the Metal-Molecule Interface

Abstract: Stable organic radicals have potential applications for building organic spintronic devices. To fulfill this potential, the interface between organic radicals and metal electrodes must be well characterized. Here, through a combined effort that includes synthesis, X-ray spectroscopy and single-molecule conductance measurements, we probe the electronic interaction between gold metal electrodes and a benchtop stable radical – the Blatter radical. We find that charge transfer can occur between the radical and the gold electrode in two directions (oxidation and reduction), depending on the environment around molecule. Under ultra-high vacuum conditions, charge transfer occurs from gold to the molecules in contact with the surface, with subsequent layers retaining their radical character. In solution-based single molecule conductance measurements, the radical character is lost through oxidation, with charge transfer occurring from the molecule to metal instead. Such a change in charge states indicates that the close proximity of half-filled states to the Fermi energy of the metal can cause the occupancy of these states to be very sensitive to the environment around the molecule.

4.1 Preface

This chapter is based on a manuscript in preparation titled *The Anomalous Behavior of the Blatter Radical at the Metal-Molecule Interface* by Jonathan Z. Low, Gregor Kladnik, Giacomo Lovat, Elango Kumarasamy, Luis M. Campos, Dean Cvetko, Alberto Morgante and Latha Venkataraman.

4.2 Introduction

Organic radicals are open-shell systems that contain one unpaired electron, making them ideal for organic materials for spintronics applications.[1-4] Typically, they are transient species and must be stabilized either by protecting the reactive site sterically or through electronic delocalization of the lone, unpaired electron.[5-7] However, less is known about the stability of radicals when interfaced with conducting electrodes and metal substrates. The rich variety of radicals and substrates available ensures that there is much interfacial physics and chemistry to explore. Several groups have already demonstrated that there are radicals that are amenable to various spectroscopic studies to probe their electronic structure on different substrates. For example, the sterically protected perchlorinated triphenylmethyl (PTM) radicals retain their radical character on a variety of configurations and surfaces,[2] and the radical states can be probed by X-ray spectroscopy.[8] Even electronically stabilized TEMPO[9] and nitronyl-nitroxide[10-12] based radicals are stable to X-ray irradiation. It is therefore not surprising that these three classes of radicals are also good candidates for performing single molecule transport measurements using gold electrodes. Molecular junctions formed with PTM radicals can show Kondo resonances[13] and enhanced conductance[14], while TEMPO and nitronyl-nitroxide based junctions have demonstrated positive[15] and negative[16] magnetoresistance respectively. In these systems, the singly occupied molecular orbitals (SOMOs) of the radicals are all localized at specific sites of the molecule. These orbitals are therefore not strongly coupled to the electrodes.

One class of radicals with large, delocalized SOMOs are 1, 2, 4-benzotriazin-4-yl radicals (Figure 4.1a). The first example of a benzotriazinyl radical was synthesized by Blatter in 1968,[17] and now bears his name. The lone electron is not confined to the nitrogen as depicted in Figure 4.1a but delocalizes across both the triazinyl ring and the fused benzene. This radical is

extraordinarily stable and can be stored in ambient conditions for months; some derivatives can persist for even longer.[18] Much credit must go to Koutentis and Constantinides for developing a rich variety of methods to synthesize a library of related compounds as well as studying some of their electronic and magnetic properties, paving the way for this radical to be used in organic electronics.[18-23] Indeed, one of the earliest reports of the Blatter radical was its use as a pressure sensitive semiconductor in a charge transfer complex with TTF.[24] More recently, Ciccullo et al. explored the possibility of using a Blatter derivative as an organic magnet, showing that it is feasible to create thin films that retain their radical properties because the molecule is only weakly physisorbed on the insulating SiO_2 substrate.[25] Crucially, their report demonstrated that the triazinyl radical moiety can also be probed by X-ray spectroscopy.

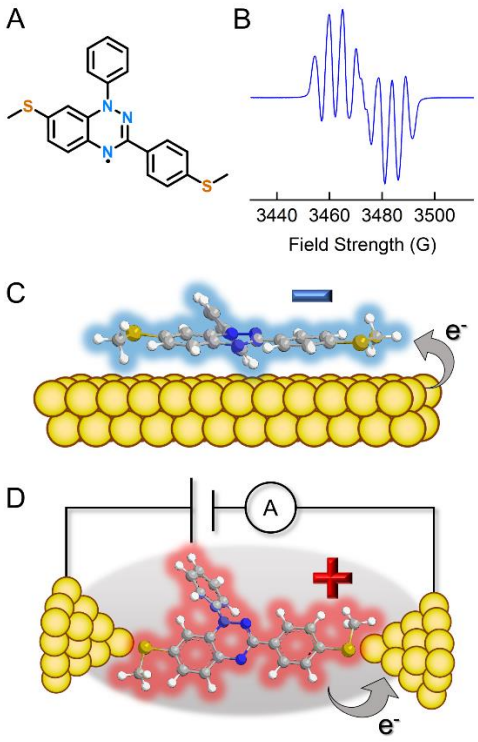

Figure 4.1. (a) The structure of the Blatter radical. (b) EPR spectrum of the Blatter radical. (c) Illustration of charge transfer from a gold substrate to the radical in vacuum. (d) Illustration of a single-molecule junction where the molecule is positively charged.

Here, we explore the electronic characteristics of the Blatter radical bound to gold by characterizing the metal-molecule interface and measuring its single-molecule transport properties. We probe the metal-molecule interface through X-ray photoelectron spectroscopy (XPS) and near edge X-ray absorption fine structure (NEXAFS) measurements under ultra-high vacuum (UHV) conditions. We find that while the first layer of radical deposited on gold extracts an electron from the substrate to form a closed shell species (Figure 4.1c), subsequent layers retain their open-shell radical character. By contrast, in solution-based single molecule conductance measurements performed using the scanning tunneling microscope break junction (STM-BJ) method,[26] electron transfer occurs in the opposite direction – from molecule to metal – and the radical is oxidized instead (Figure 4.1d). These results highlight the importance of the environment on the stability of an open shell system interacting with a metal electrode.

4.3 Results and discussion

We synthesized a novel derivative of the Blatter radical with two gold-binding thiomethyl groups (Figure 4.1a) according to a reported procedure as detailed in section 4.17.[19] The electron paramagnetic resonance (EPR) spectrum shows the expected 7 line splitting pattern (Figure 4.1b) due to the unpaired electron coupling to 3 of the spin 1 nitrogen nuclei. For the X-ray spectroscopic measurements, films of the radical were created by evaporating the molecule onto a pristine Au(111) surface in UHV (see section 4.6 for details). By controlling the evaporation time and substrate temperature, either a monolayer or a multilayer could be obtained. The terminal thiomethyl groups allow the molecule to bind to the gold electrodes for the STM-BJ measurements performed in solution. Density functional theory (DFT) calculations (details in section 4.8) were used to support our experimental observations.

We first describe the results from XPS measurements that are sensitive to the electronic and chemical environment around the atoms present in the radical. Figure 4.2a shows the XPS spectrum of a multilayer film. The expected peaks in the nitrogen 1s (N 1s), carbon 1s (C 1s), and sulfur 2p (S 2p) binding energy regions are present (see section 4.7 for more details). Figure 4.2b shows the fit of the N 1s region of the monolayer and multilayer films. In both films, there are multiple N 1s peaks indicating that the nitrogen atoms in the molecule are indeed distinct. For the multilayer, we fit the spectrum with 3 main peaks that have a 1:1:1 ratio (black traces), and a secondary doublet that consists of peaks in a 2:1 ratio (light gray). The 3 main peaks can be assigned according to Ciccullo et al.,[25] and also corroborated with our DFT calculations (section 4.8). The presence of the lowest binding energy peak (398.7 eV) indicates that the radical nitrogen (N4, Figure 4.2b inset) is present and this derivative of the Blatter radical retains its unpaired electron in the multilayer. The other two peaks at 399.7 eV and 401.5 eV are assigned to N2 and N1 respectively as indicated. There is also a small peak at the high binding energy side of the spectrum (dashed line) which is assigned to shake-up transitions.[25] We ascribe the secondary doublet to a species that arises from beam damage to the pristine molecules, as detailed in the section 4.7. By contrast, the N 1s peak for the monolayer film is much narrower and can be fit by a doublet in a 2:1 ratio. The difference in the two spectra indicates that the core N1s electrons of the molecules in a monolayer film have a different environment when compared with those of the multilayer.

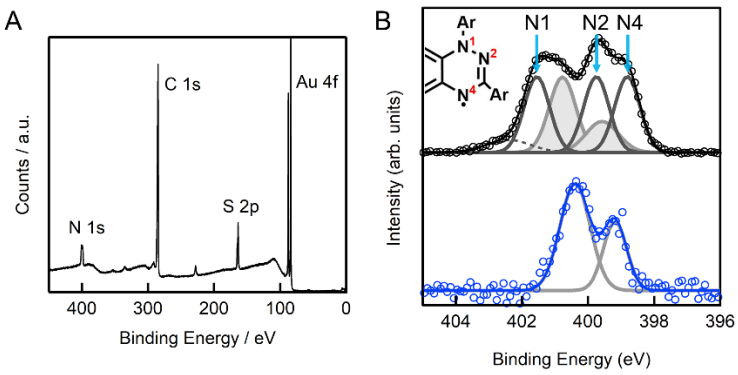

Figure 4.2. (a) Wide energy range XPS scan of a multilayer of the Blatter radical derivative. (b) Nitrogen 1s XPS spectra of the multilayer (top, black) and monolayer (bottom, blue) along with the fits. For the multilayer, peaks are assigned to the nitrogen atoms as indicated and a partial structure of the Blatter radical with the nitrogen atoms labelled is shown in the inset. The shaded light gray peaks in the multilayer spectrum are due to a second, damaged species present in the sample (details in main text).

Next, we examine the N 1s (K-edge) NEXAFS spectra which probes the electronic structure of the unoccupied states and can therefore elucidate the existence of a singly unoccupied molecular orbital (SUMO) which should be present if the open-shell structure is unperturbed. Figure 4.3a shows the N 1s NEXAFS spectrum of the multilayer sample in black. There are 3 peaks in this region – 2 shorter peaks and a taller one – which arise from electronic transitions from the N 1s core to the lowest unoccupied states in the radical. To assign these peaks, we turn to DFT calculations of the NEXAFS spectrum (see section 4.8). The peaks at 396.8, 397.8 and 399.7 eV indicated by the green arrows correspond to transitions from 3 different initial atoms (N4, N2, and N1 respectively) into the same final state. This final state is the SUMO, since this orbital has significant electron density on all three nitrogen atoms. A schematic of these transitions, along with the calculated molecular orbitals are shown in Figure 4.3b. Furthermore, these peak assignments follow the energetic order determined from XPS: the N4 (N1) atom has the lowest (highest) XPS binding energy and therefore gives rise to the lowest (highest) energy absorption feature in the NEXAFS. The energy spacing between the 3 nitrogen peaks in XPS and NEXAFS

are also equal. The 399.7 eV peak has a higher intensity because it overlaps with a second peak, visible as a shoulder and indicated by the orange arrow on the spectrum. This shoulder peak can be assigned to a transition from one of the N atoms to the doubly-unoccupied LUMO. There is only a single peak because this orbital only has significant electron density on the N2 atom (Figure 4.3b).

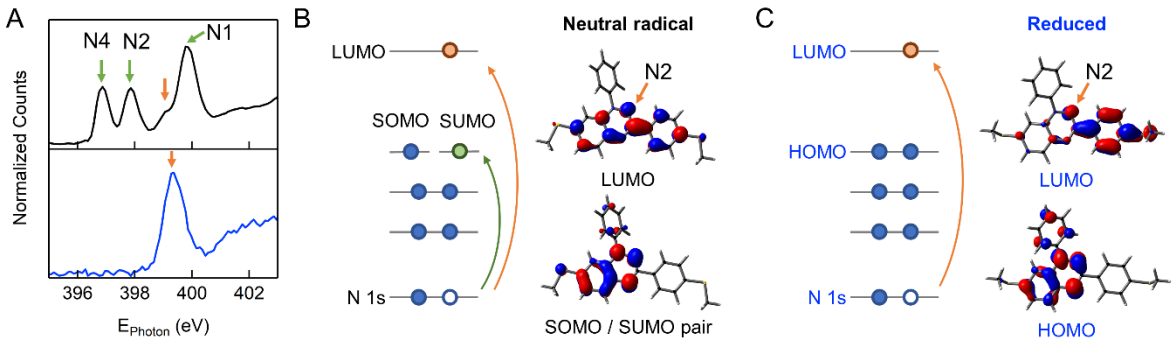

Figure 4.3. (a) Nitrogen 1s NEXAFS spectra of a multilayer (black) and monolayer (blue) of the Blatter radical derivative. The peaks are labelled by the individual nitrogen atoms that cause the absorption features. (b) Schematic of the electronic transitions associated with the NEXAFS peaks in the multilayer (neutral radical), along with the frontier unoccupied orbitals involved from gas-phase DFT calculations. The green and orange arrows show the transitions corresponding to the peaks indicated in (a). Note that in the DFT of the radical, the α and β spin orbitals are treated separately and only the α orbitals are shown in here. The β orbitals are qualitatively similar and can be found in Figure 4.9. (c) The transition that leads to the NEXAFS peak in the monolayer (reduced radical), along with selected frontier orbitals.

The NEXAFS spectrum of a monolayer film is very different. There is only a single clear peak (~399.3 eV) which again points to a loss of radical character in this film. We hypothesize that the SUMO level is no longer available for a transition and the LUMO – which only has orbital density on N2 – becomes the first available unoccupied state (Figure 4.3c). We propose that this loss is due to charge transfer from the underlying gold substrate to the monolayer, which fills the SUMO of the radical. This first layer, which lies nearly flat on the substrate (see section 4.9), prevents subsequent layers from interacting with the substrate, so they retain their unpaired spin.

The loss of radical character could also have resulted from an oxidation with an electron transfer from molecule to substrate instead, but this possibility can be eliminated by examining the LUMO of the oxidized species (see section 4.8). If the molecule is oxidized, the new LUMO still has electron density on all three N atoms. We would therefore expect that the lowest N 1s to LUMO transition of an oxidized species in a monolayer to also result in three peaks, similar to the three peaks that originate from the N 1s to SUMO transitions of the intact radical molecules in the multilayer. Furthermore, valence band XPS measurements (see section 4.10) and DFT calculations to simulate the NEXAFS spectrum (section 4.8) corroborate that the radical in the monolayer has gained, rather than lost, an electron.

We now turn to solution based single molecule conductance measurements carried out using the STM-BJ method.[26] In this method, a gold STM tip is driven into contact with a gold substrate and slowly retracted while in a solution of molecules with gold binding groups. A small bias is applied between the tip and substrate, and the conductance is recorded as a function of relative tip/substrate displacement. As the tip is withdrawn, a gold-gold point contact with a conductance around 1 G_0 (= $2e^2/h$ = 77.48 μS) is formed. Further retraction of the tip breaks the gold point contact and a molecule can bind between the electrodes, creating plateaus below the 1 G_0 feature in the conductance versus displacement graphs. These plateaus are the conductance signatures of individual molecular junctions. The data from thousands of individual traces can be collected and compiled into logarithmically binned 1D conductance histograms to identify the conductance peaks (Figure 4.4a). No data selection is performed.

The 1D histogram of the Blatter radical is shown as the brown trace in Figure 4.4a. Two clear conductance features are visible – a sharp, high conductance peak at around 3.2×10^{-3} G_0, and a broad peak near 3.2×10^{-5} G_0 which is ~100 times lower in conductance. In the 2D

conductance histogram which is created by overlaying the individual conductance vs displacement traces (Figure 4.4b), the lower conductance peak is slightly offset to longer displacements than the high conductance peak, indicating that this low conductance feature appears only after the tip is retracted further and the high conductance plateau ruptures. We attribute the higher conductance peak to a molecular junction with both thiomethyl linkers bound to the gold electrodes, while the lower conductance peak is a dimer junction where only one end of each molecule binds to the gold electrode and conduction occurs through the interaction of the two π systems.[27-29] The nature of the two peaks was established by analyzing conductance noise according to a previously reported method and detailed in section 4.11.

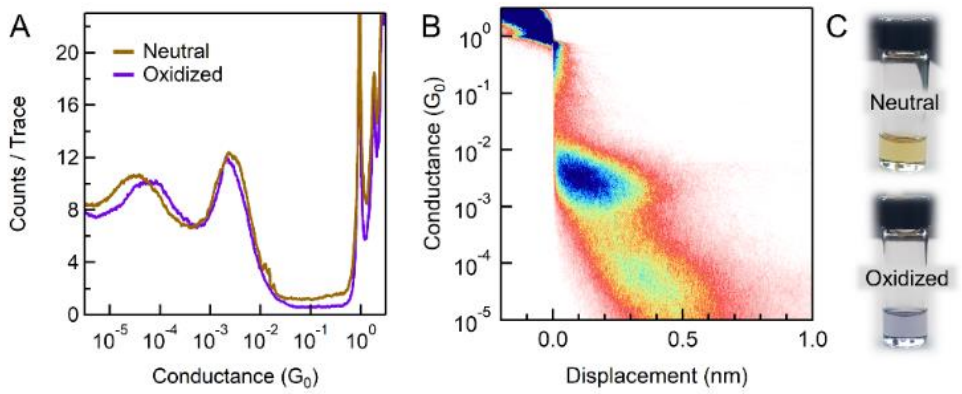

Figure 4.4. (a) 1D conductance histogram of the neutral radical (brown) and chemically oxidized radical (purple) measured at 200 mV and compiled from 3000 traces. (b) 2D conductance histogram of the neutral radical created from the same traces used for the 1D histogram shown in (a). (c) Photos of the different colored solutions of the neutral and oxidized species.

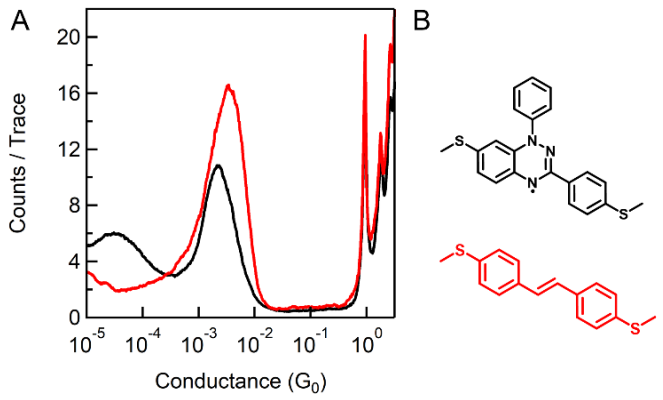

Figure 4.5. (a) Conductance histogram of the Blatter radical derivative (black trace) compared to 4,4'-di(methylthio)stilbene (red trace). The measurements were performed in trichlorobenzene at a concentration of 10 μM and an applied bias of 100mV. The main conductance peaks coincide, indicating that the radical has been converted into a closed shell species. The stilbene shows no low conductance peak. (b) Structure of the Blatter radical derivative and 4,4'-di(methylthio)stilbene in the colors corresponding to the traces in (a).

Surprisingly, the high conductance peak of the radical is very similar in magnitude to that of 4,4'-di(methylthio)stilbene (Figure 4.5). Both these molecules have 11 bonds along the conductance pathway. This result is contrary to the expectation that the conductance of an open shell radical should be high due to the availability of a low-lying orbital for electron transfer.[30] Thus, the fact that the Blatter derivative had a conductance similar to that of a closed shell stilbene hinted at the possibility that the radical loses its open shell character in a single-molecule junction. We therefore tested the redox stability of the radical in solution by performing cyclic voltammetry (CV) in the STM-BJ setup (details in section 4.12). Figure 4.6a shows that with gold electrodes, the molecule is oxidized at very low potentials. The reduction wave, although visible in the platinum electrode CV (Figure 4.6b), is never observed in the voltammogram recorded on gold. This led us to investigate the conductance of a chemically oxidized Blatter radical derivative.

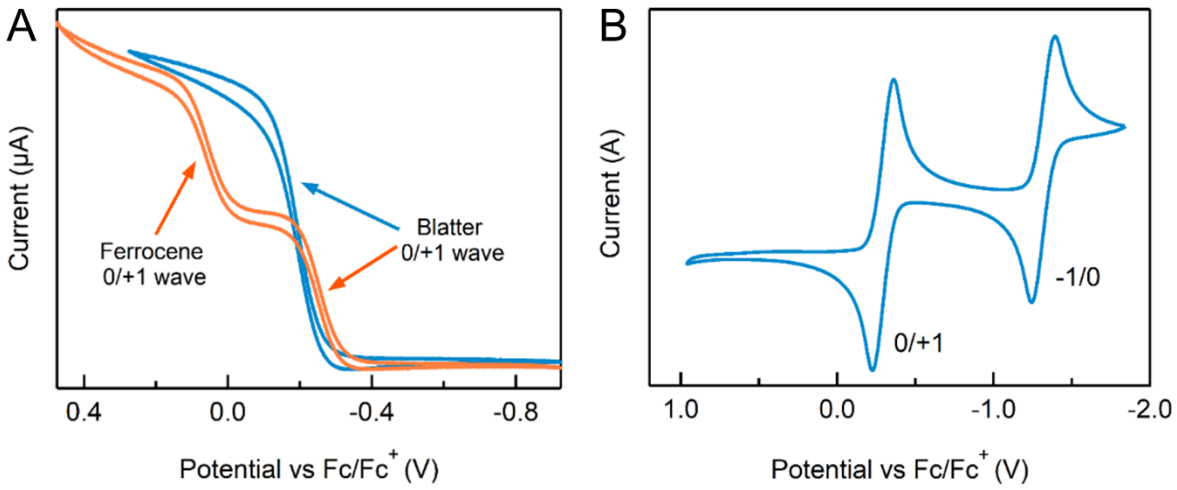

Figure 4.6. (a) In-situ cyclic voltammogram of the Blatter radical derivative (blue) and of both the radical and ferrocene (orange) in anhydrous propylene carbonate using gold electrodes. The potential is calibrated to the onset of the Fc/Fc+ oxidation wave. (b) Platinum electrode cyclic voltammogram of the Blatter radical derivative calibrated to the $E_{1/2}^{Ox}$ *of ferrocene, which is set at 0 V. The oxidation and reduction potentials of the radical are* $E_{1/2}^{Ox}$ *= -0.29 V and* $E_{1/2}^{Red}$ *= -1.32 V.*

We performed the STM-BJ measurement with a solution of the chemically oxidized Blatter derivative (details in section 4.15). The solution of the radical turns from brown to purple upon oxidation (Figure 4.4c), and it can be characterized by UV and NMR as it is a closed shell species (see section 4.14). The conductance histogram of the oxidized species is the purple trace in Figure 4.4a, which is nearly identical to the histogram of the neutral radical. This strongly suggests that the neutral radical gets oxidized spontaneously in the junction, and the conductance traces generated are those of the closed-shell oxidized species. We stress that the oxidation only occurs in the junction at the metal-molecule interface, since the color of the solution of neutral molecules is the same before and after the experiment.

Taken together, we observe dramatic, unexpected differences in the chemical behavior of the Blatter radical at metal-molecule interfaces: a) at room temperature in UHV, the lack of XPS and NEXAFS peaks associated with the radical state and supporting DFT calculations point

unambiguously to the SUMO being filled, that is, reduction of the molecule, and b) in solution-based STM measurements, the radical is spontaneously oxidized instead, readily losing the electron in its SOMO. To reconcile the vastly different behavior of the radical on gold in two different environments, we consider three key differences between the UHV and STM-BJ measurements. First, the level alignment at the interface is likely to be very sensitive to the environment; the SOMO could thus be closer to the Fermi energy (E_F) of gold in a molecular junction in solution while SUMO could be close to E_F in UHV. Second, undercoordinated gold adatoms which the molecules bind to in the STM-BJ (Figure 4.1d) are slightly electron deficient;[31,32] this could facilitate the oxidation of a low-lying SOMO. Finally, the optimized structures from DFT show that the neutral and oxidized molecule adopt a similar conformation, while the reduced molecule has its terminal sulfur-carbon bond of the thiomethyl group rotated out of plane of the π system (see section 4.8). This indicates a larger reorganization energy when reducing the radical, which is further increased in solution since the solvent molecules have to realign their dipoles. Thus, reduction is more facile in UHV than in solution.

4.4 Conclusions

In conclusion, we have investigated how the Blatter radical interacts with gold electrodes. Using X-ray spectroscopy, we showed that the SUMO is filled when interacting with an Au(111) surface in UHV. Only molecules in contact with the gold substrate undergo charge transfer and get reduced, and multilayer films retain their radical character. In single molecule conductance measurements performed in solution, we demonstrate that the conductance signature arises from an oxidized radical. We propose that this behavior stems from the proximity of both the SOMO and SUMO to the E_F of gold, allowing either reduction or oxidation to occur based on small changes in the surrounding conditions. Our work shows that radicals with their half-filled orbitals

close to the Fermi level can behave very differently even with the same substrate under different environments and illustrates the importance of metal-molecule coupling to the stability of radicals on metal surfaces.

4.5 General experimental

^{1}H-NMR and ^{13}C-NMR were performed using a Bruker Avance III 400 (400 MHz) or Avance III 500 (500 MHz) NMR spectrometer. Mass spectra were recorded on a XEVO G2-XS Waters® Mass Spectrometer with a QTOF detector at the Columbia University Mass Spec Facility. Either electrospray ionization (ESI), atmospheric pressure chemical ionization (APCI), or atmospheric solids analysis probe (ASAP) were used for ionization as indicated. Absorption spectra were recorded on a Shimadzu UV 1800 UV-Vis spectrophotometer. X-band Electron paramagnetic resonance (EPR) spectra were recorded on a Bruker EMX spectrometer using a modulation amplitude of 0.50 G. The sample was dissolved in toluene and placed in quartz tubes with 4 mm inner diameter. Argon was bubbled through the solution prior to sealing the tube.

4.6 X-ray measurement details and sample preparation

The X-ray spectroscopic measurements (XPS and NEXAFS) were all performed at the ALOISA beamline at the Elettra Synchrotron in Trieste. The radical films were prepared by evaporating the molecule from a crucible heated to ~170°C in a preparation chamber at a pressure of 10^{-7} to 10^{-8} mbar with a base pressure lower than 10^{-9} mbar. The deposition times varied between 30 to 180 s to obtain different film coverages. The measurement chamber was kept under ultrahigh-vacuum at a pressure lower than 10^{-10} mbar with the sample at ambient temperature.

The clean Au(111) surface was prepared by cycles of Ar^{+} sputtering (1.5 keV) and annealing up to ~750 K. After each cleaning cycle, the surface was checked for cleanness by XPS in the carbon, nitrogen, oxygen and sulfur regions. The photoemission signal was detected by a

hemispherical electron analyzer in normal emission geometry, with grazing (4°) photon beam incidence angle. The overall energy resolution was about 200 meV for the core-level XPS taken at a nominal photon energy of 515 eV and about 100 meV for the valence-band measurements taken at a nominal photon energy of 140 eV. The binding energy of the spectra was calibrated to the Au $4f_{7/2}$ peak at 84.0 eV or the Fermi edge at 0 eV.

4.7 Core-level XPS measurements

The nitrogen region of the XPS was discussed in section 4.3. Here, we comment on the difference between the multilayer and monolayer in the XPS spectra of the sulfur 2p (S 2p) region. In the multilayer (Figure 4.7c), there is one sulfur doublet with peaks at 165.1 and 164.0 eV, corresponding to only one sulfur environment, as expected for an uncoupled multilayer. In contrast, the monolayer shows a triplet with peaks at 164.8, 163.6, and 162.5 eV, corresponding to two overlapping sulfur doublets. There are two possible reasons for the different sulfur environments. First, only one of the sulfur atoms may form a strong interaction to gold while the other remains unbound due to lattice constraints, with the unbound sulfur showing the higher binding energy.[33-35] Second, since the molecule is long, a slight tilt can cause a difference in the sulfur-gold distance at both ends, causing the shift in binding energy observed due to different screening.[36]

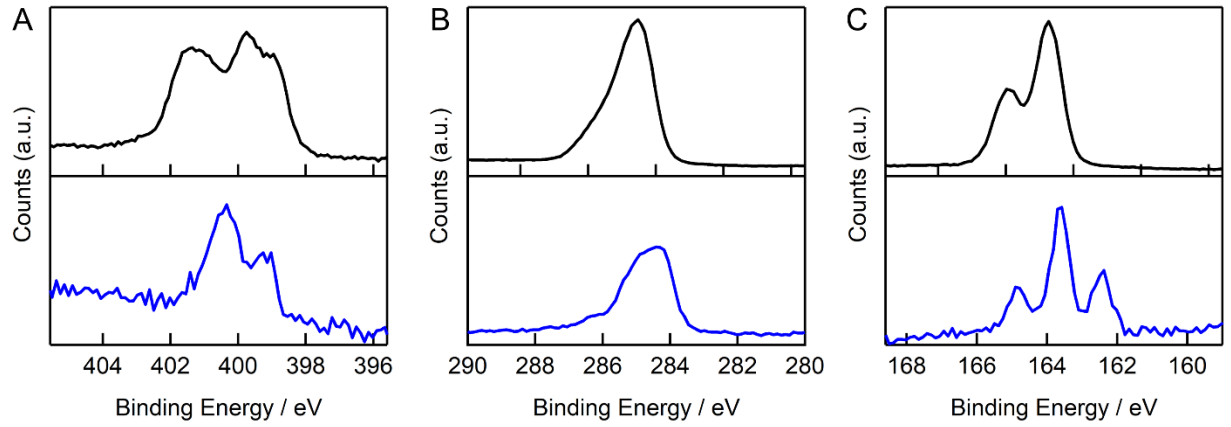

Figure 4.7. XPS of the (a) carbon 1s and (b) sulfur 2p regions for the multilayer (black) and monolayer (blue) films.

We also comment on the secondary doublet that appears in the N 1s region the multilayer film that was ascribed to a damaged radical species in section 4.3. In Figure 4.8, we show 3 other N 1s XPS spectra that arise from different exposure times to the X-ray irradiation due to successive scans on the same spot. This series of spectra can be fit with the same set of peaks arising from the pristine (black traces) and damaged (light gray) molecules. With increasing exposure time, it can be seen that the intensity of the signals from the pristine molecules decreases, while the signal intensity from the damaged molecules increases. We did not attempt to further characterize the damaged molecules, although we note that the peak shape is very similar to the reduced radical in the monolayer films (Figure 4.2).

Beam damage to the radical films was also noted by Ciccullo et al.,[25] which resulted in a secondary feature in the same ~400.5 eV region that we show here. However, the damage they reported was much less than what we observed. This is probably due to the higher photon flux of the synchrotron radiation we used, and also the different energy of incident beam used. In our measurement, the incident beam of 515 eV is closer to the resonance of nitrogen, which would produce more secondary electrons that can damage the film. Since we were aware of the beam

damage from the outset of the experiments, we ensured that all spectra presented in this work were measured on pristine spots of the films.

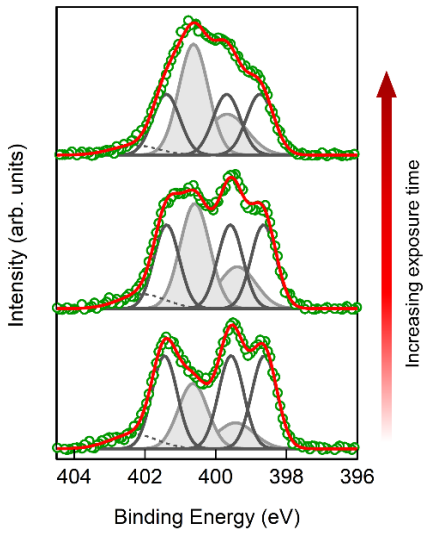

Figure 4.8. Evolution of the nitrogen 1s XPS spectrum with increasing exposure time on the same spot.

4.8 Density functional theory calculations

The geometry optimization of the isolated molecule was performed using DFT calculations with Gaussian09.[37] The B3LYP functional and 6-31G** basis set were used. The optimized geometry then served as input to GPAW, a DFT Python code based on the projector-augmented wave (PAW) method to calculate the N 1s core electron binding energies (CEBEs) as well as the N 1s (K-edge) X-ray absorption spectra.[38-40]

The calculated ground state molecular orbitals of the neutral, reduced and oxidized radical in the gas phase are shown in Figure 4.9. They are very similar to the orbitals calculated for the Blatter without any thiomethyl groups.[41] Note that for the neutral radical, unrestricted DFT calculates the spin α and spin β orbitals separately. The SOMO (α) and SUMO (β) pair are identical since they are essentially the same orbital. The orbitals above and below these are paired

up as well. Also note that the HOMO of the reduced species, the SOMO (α) and SUMO (β) of the neutral species, and LUMO of the oxidized species are all similar because when the neutral radical gains an electron, this is the orbital that becomes doubly occupied. When the radical is oxidized, this is the orbital that is emptied.

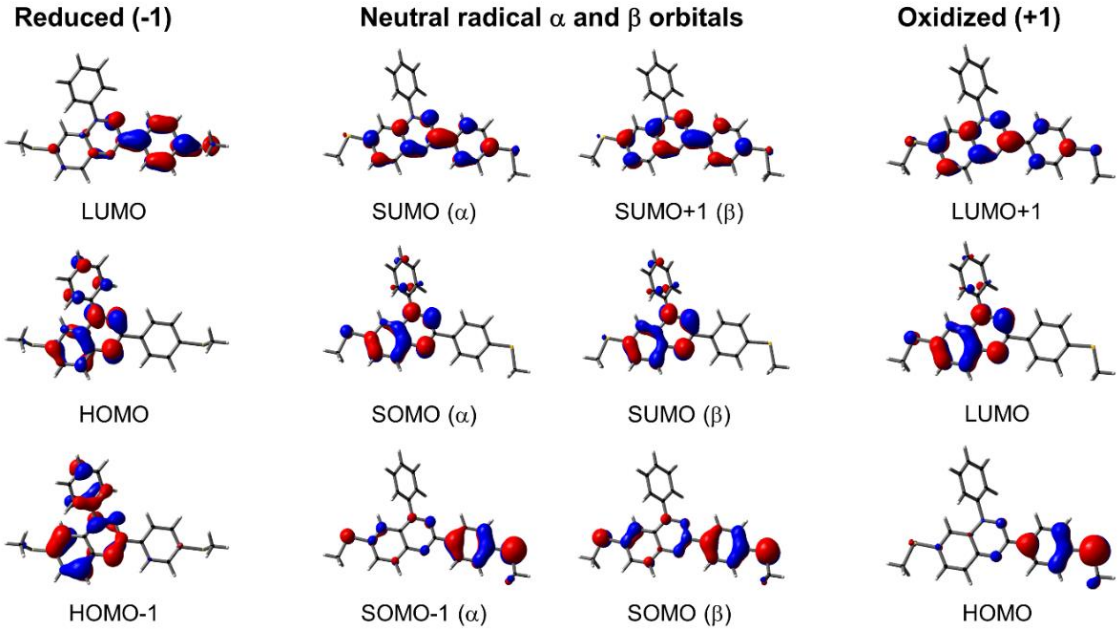

Figure 4.9. Orbitals of the reduced, neutral, and oxidized Blatter derivative visualized with an isovalue of 0.04.

We next calculated the N 1s CEBEs of all three inequivalent nitrogen sites for the neutral radical with the PBE functional with a cell size of 25.6 Å and grid spacing of 0.2 Å using the delta Kohn-Sham scheme. The full core-hole PAW setups were created with GPAW and default parameter values. All calculations were spin-polarized due to the open-shell nature of the radical. Figure 4.10 shows the comparison of the calculated CEBEs and the experimental N 1s XPS spectrum of the multilayer film fit with 3 main peaks for the pristine molecule and a doublet for the damaged species present in the film (see section 4.7 for details). The calculated CEBEs were rigidly shifted to match the position of the lowest binding energy peak. The calculated core-level

shifts match nicely with the fits of the three main peaks, which allows us to confirm the peak assignments from highest to lowest binding energy as N1, N2, and N4 as shown in Figure 4.10b.

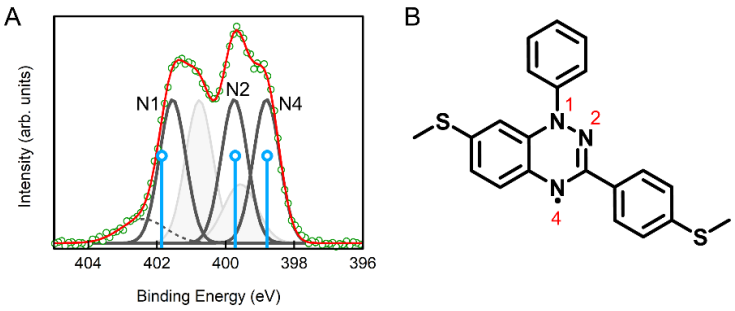

Figure 4.10. (a) Neutral radical multilayer N 1s XPS data (green circles) is shown fitted with three main peaks (dark gray traces) and an additional 2:1 doublet (light shaded gray). The blue sticks correspond to the DFT calculated core electron binding energies (CEBEs) of the three inequivalent nitrogen sites, which show good agreement with the experimental data. (b) Structure of the Blatter radical derivative with the corresponding nitrogen atoms labelled.

We also calculate the N 1s (K-edge) absorption spectra for both the neutral and reduced (charge -1) radicals, which correspond to the species probed in the multilayer and monolayer films respectively. The X-ray absorption spectra were simulated for each inequivalent nitrogen atom separately using the half core-hole transition potential method as implemented in GPAW. The calculation parameters were the same as for the CEBE calculations described above. The absolute excitation energies were calculated by adding the delta Kohn-Sham calculated energy of the first (lowest energy) excitation (core $\rightarrow$ SUMO / LUMO) to account for the initial state effect of the different inequivalent nitrogen atoms. The NEXAFS spectra were then obtained by combining all transitions from the different initial states and convoluting with a gaussian with a full width half maximum of 0.6 eV. An additional rigid shift was employed to match the simulated NEXAFS spectra with the experimental data for better comparison. For both the multilayer and monolayer film, the experimental and calculated data are in very good agreement.

Figure 4.11a shows the experimental and calculated N 1s absorption spectrum for the neutral (multilayer) radical. The colored bars arise from the transitions from the correspondingly colored nitrogen atoms in Figure 4.11b. The dark and light bars of the same color differentiate transitions from the α and β spins respectively. There are 3 transitions in the neutral radical that are core transitions from the 3 inequivalent nitrogen atoms to the singly unoccupied molecular orbital (SUMO). As mentioned in section 4.3, the transitions in the calculated NEXAFS agree with the XPS results because the atom with the lowest (highest) XPS binding energy N4 (N1) is responsible for the lowest (highest) energy absorption feature in the NEXAFS. There is also a feature at ~399.2 eV, which we assign to the N2 $\rightarrow$ LUMO transition. In contrast to the core $\rightarrow$ SUMO transitions which have contribution from the β spins (since the α orbital is occupied), the N2 $\rightarrow$ LUMO transition has contribution from both α and β spins. The N2 $\rightarrow$ LUMO and the N1 $\rightarrow$ SUMO transitions overlap to form the highest intensity X-ray absorption feature in this region.

Figure 4.11c shows the experimental and calculated spectrum for the reduced (monolayer) radical. Since the SUMO is now occupied, the first available transitions are from the core to the next higher unoccupied level which is the LUMO. Here, the orbitals have very little weight on N1 and N4 (Figure 4.11d), and the peak intensity arises from mainly the N2 $\rightarrow$ LUMO transition, with some small contribution from N4.

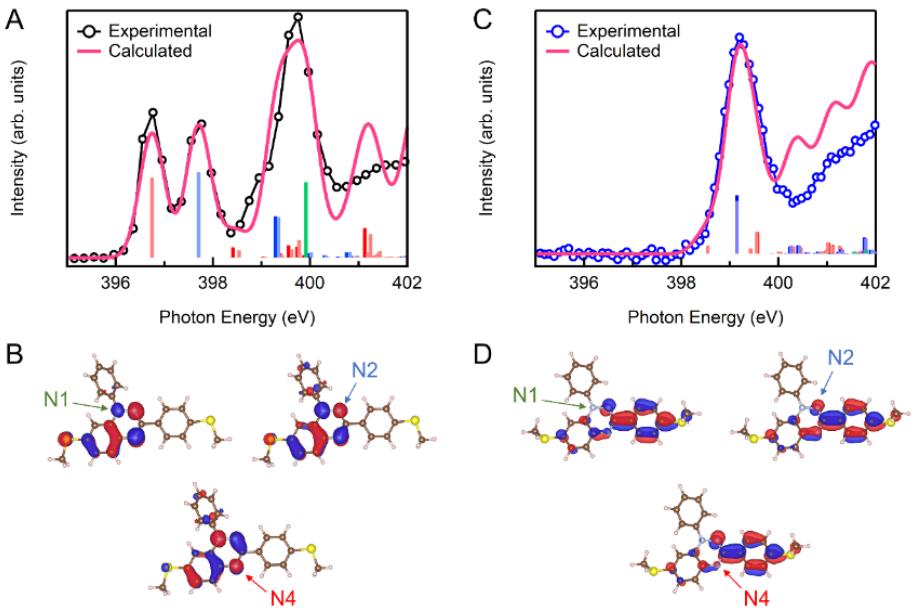

Figure 4.11. Calculated spin polarized half core-hole N 1s NEXAFS transitions. In (a), the experimental spectrum of the neutral radical (multilayer film, black trace) is compared to the calculated absorption spectrum (pink trace and colored bars) obtained from DFT transition potential calculations. Transitions from the individual N atoms indicated on the SUMOs in (b) are calculated and shown as the corresponding colored bars in (a). In (c), the same analysis is performed for the reduced species present in the monolayer, with the corresponding LUMO orbitals shown in (d).

4.9 Polarization-dependent NEXAFS

Near-edge X-ray absorption fine structure (NEXAFS) spectra were collected at a photon incident angle of 6° in partial electron yield by a wide acceptance angle channeltron. The polarization of the incident light was either parallel (*p-pol*) or perpendicular (*s-pol*) to the sample normal.

Polarization dependent nitrogen K-edge NEXAFS measurements show that the fused benzotriazinyl core of the molecules in the monolayer lie flat on the gold surface, with the π system perpendicular to the substrate. The 399.3 eV peak, which is a transition to the π* LUMO (see DFT calculations in section 4.8 for assignment details), is strongest when the incident light is polarized perpendicular (*p-pol*) to the substrate but is suppressed when light is polarized parallel (*s-pol*) to

the substrate (Figure 4.12a).[42,43] The carbon K-edge *p-pol* and *s-pol* NEXAFS spectra (Figure 4.12b) show a less pronounced dichroism of the main π* resonances at around 285 eV, most probably because the two pendant phenyl rings bound with a single bond to the fused benzotriazinyl core are able to rotate freely out of the perpendicular plane as portrayed in Figure 4.1c.

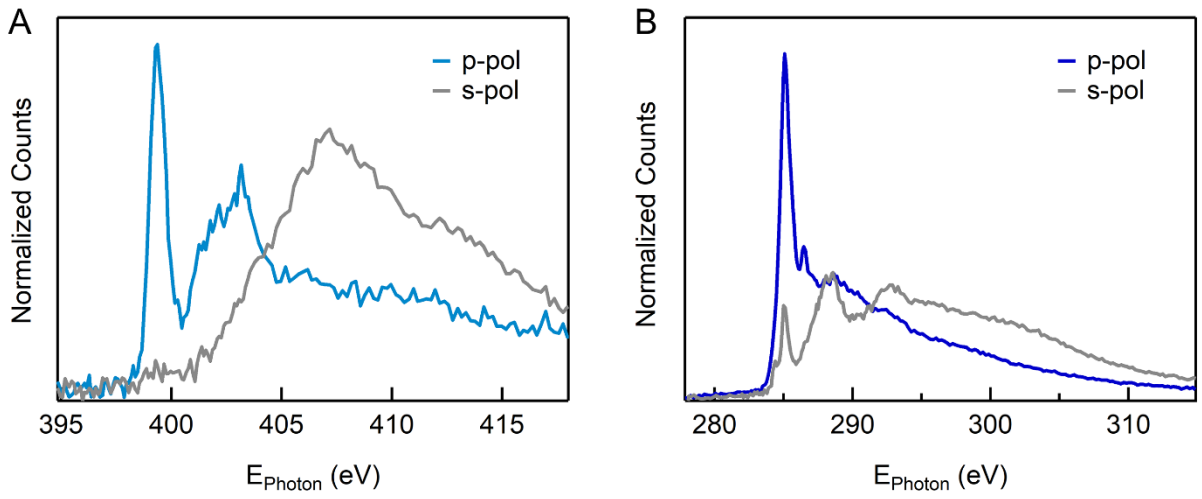

Figure 4.12. Nitrogen K-edge (a) and carbon K-edge (b) NEXAFS spectra of the Blatter radical derivative. Both p- and s-pol spectra are shown.

4.10 Valence band XPS

We measured the valence band spectra of the multilayer (neutral) and monolayer (reduced) Blatter radical films in order to determine the relative energies and occupancy of the singly occupied molecular orbitals (SOMO) and highest occupied molecular orbitals (HOMO). The spectra both show features arising from the SOMO and HOMO of the neutral and reduced species respectively, along with occupied states related to the valence band of the gold substrate. Figure 4.13 shows the raw valence band spectra of clean gold and the two radical films with the Shirley type background subtracted. A normalization factor was then calculated as a ratio of the intensities

of the best resolvable molecular orbital peaks with binding energies 12-18 eV (shown in the inset of Figure 4.13), to account for different coverages of the two films.

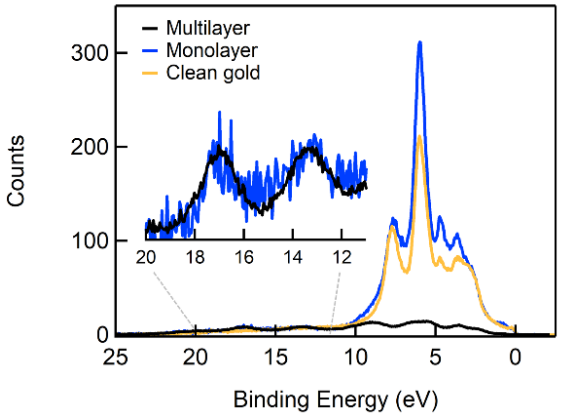

Figure 4.13. Measured valence band spectra with Shirley type background subtracted. The inset shows a zoom-in of the peaks employed for the intensity normalization.

Next, we obtained a high resolution narrow band (0-10 eV binding energy) spectrum of the clean gold substrate (Figure 4.14a) and fit this with 2 components: 1) a Fermi step-like background which includes inelastic scattered electrons modelled with a polynomial (purple trace), and 2) molecular states from the gold substrate (pink trace). This two components were also used to fit the high-resolution spectrum of the monolayer (Figure 4.14b), in order to identify the molecular peak arising from the LUMO state (blue shaded trace). In the case of the multilayer film (Figure 4.14c), no substrate related features were visible, and the data was fit with a Shirley type background (light blue trace) and the molecular features (shaded gray trace and light gray trace). Here, the peak from the highest occupied state (shaded gray trace) is due to the SOMO. The intensities of the fitted peaks (HOMO and SOMO) were then normalized using the normalization factor found from the first step of the analysis (obtained from Figure 4.13). The ratio of the normalized peak intensities of the SOMO (in the multilayer) to HOMO (in the monolayer) is

approximately 0.4:1, which is consistent with the SOMO being half-filled compared to the HOMO, assuming that the HOMO of the reduced species is fully occupied.

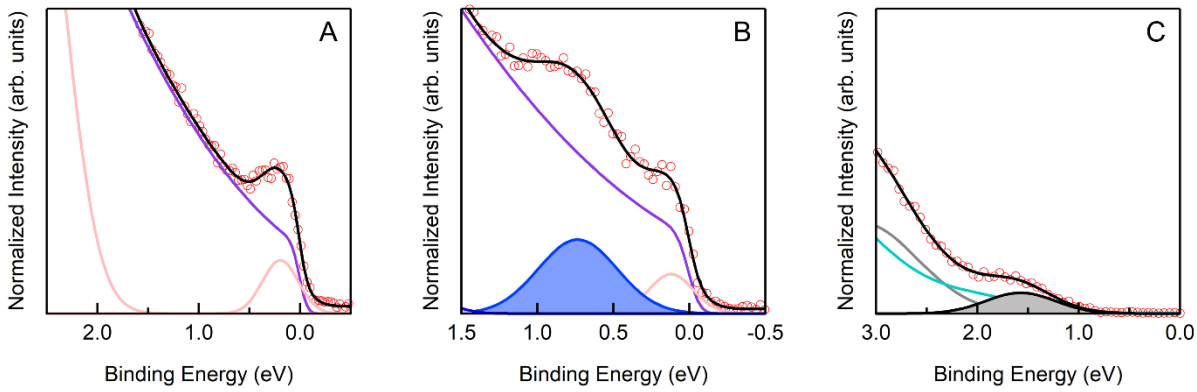

Figure 4.14. Valence band fits of (a) the clean gold substrate, (b) monolayer in which the radical is reduced, and (c) multilayer film where the radical remains neutral. The fit components in (a) and (b) are the Fermi background (purple trace), the gold molecular features (pink trace) and the LUMO feature from the Blatter states (blue shaded trace). In (c), there is no contribution from the gold substrate, and the data is fit with a Shirley type background (light blue trace) and two molecular states – the SOMO state (gray shaded trace) and a deeper molecular state (light gray). The ratio of the LUMO:SOMO feature in the monolayer and multilayer is 1:0.4.

4.11 Conductance noise measurements

We characterized the conductance noise of the molecular junctions to differentiate between through-bond and through-space charge transport using the method described by Adak et al.[44] In order to measure the noise, we modify the STM-BJ measurement technique as follows. We first form a contact between the tip and substrate in an environment of the molecules and then break the contact by withdrawing the tip from the substrate at a speed of 20 nm/s. After a fixed elongation of 2.3 nm, we hold the junction for 150 ms and record the conductance with a 100 kHz sampling rate applying a bias voltage of 200 mV. We select traces that sustain a molecular junction during the hold period and calculate the discrete Fourier transform of this data. Out of a total of 71,000 traces measured using this modified ramp, 1749 sustained a high-conducting junction during the

150 ms hold period (Figure 4.15b) while 2378 sustained a low conducting junction (Figure 4.15c). These traces were selected for analysis.

Two quantities are calculated from the measured conductance while the junction is held for each of these traces: the average conductance (G) and the normalized noise power (power spectrum density (PSD)/G). The PSD is obtained from the square of the integral of the discrete Fourier transform of the measured conductance between 100 Hz to 1000 Hz. The lower frequency limit is constrained by the mechanical stability of the setup. The upper limit is determined by the input noise of the current amplifier. Using these quantities, we create 2D histograms of the normalized noise power against the average conductance. The relation between noise power and conductance is extracted by determining the exponent *n* for which PSD/G and G are not correlated. We have previously shown that the relationship between flicker noise power (PSD) and junction conductance (G) follows a power law dependence ($PSD \sim G^n$) with the scaling exponent (*n*) being indicative of the electronic coupling type: *n*=1 is characteristic of through-bond coupling while *n*=2 is characteristic for through-space coupled junctions. Details of these derivations are presented in Adak et al.[44]

From our data, we find that the high-conductance junctions have an exponent *n*=1.1 (Figure 4.15e). This indicates that the thiomethyl-terminated molecular junctions are coupled through an Au-S bond, as depicted on top in Figure 4.15d. In contrast, the data in Figure 4.15f for the low conducting junctions have an exponent *n*=1.8. This indicates that conductance involves through-space transport as detailed further in the work of Magyarkuti et al., and as depicted on the bottom of Figure 4.15d.[29]

As a second control, we also synthesized a derivative of the Blatter radical that has only one gold-binding thiomethyl linker; this molecule shows a single conductance peak (Figure 4.16a),

demonstrating the strong propensity for this family of radicals to form dimer junctions. The synthesis of this molecule is reported in section 4.17. We find that the propensity for the Blatter radicals to form these dimer junctions is so strong that lowering the concentration by a factor of 1000 does not lower the probability of their formation (Figure 4.16b). At the lowest concentration we observed the monomer peak (1 μM), we also observed the dimer peak. From previous investigations of dimer junctions, lower concentration was found to lower the probability of dimer formation.[29]

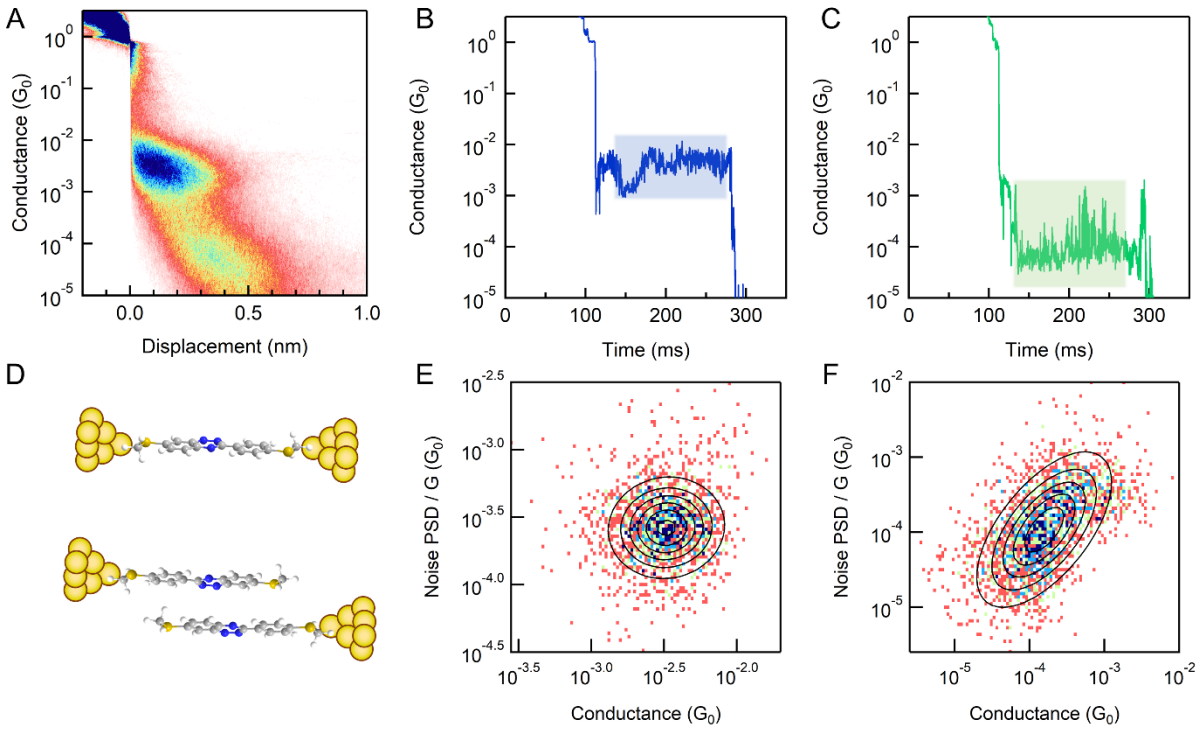

Figure 4.15. (a) 2D conductance histogram of the Blatter radical derivative. Individual traces from the fixed-hold experiments for (b) the high conductance and (c) low conductance peaks. (d) Representation of the monomer and dimer junctions formed. Normalized noise power versus conductance histograms for the (e) high conductance and (f) low conductance peaks. See text for details.

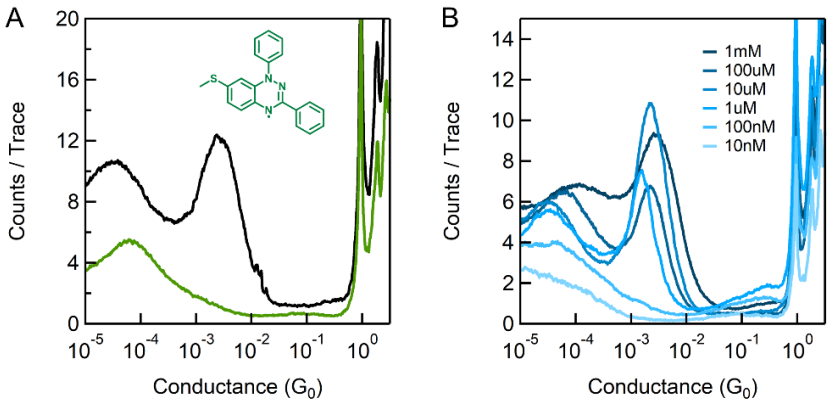

Figure 4.16. (a) Conductance histogram of the Blatter radical derivative with two thiomethyl linkers (black trace, see Figure 4.1a for structure), along with the histogram of the radical with only one thiomethyl linker (green). The structure of the radical with only one linker is shown inset. (b) Conductance histograms of the Blatter radical derivative (with two thiomethyl linkers) at varying concentrations. At concentrations below 1 μM, no conductance peaks are visible.

4.12 In-situ cyclic voltammetry with gold electrodes

To check the redox stability of the Blatter radical in the gold junction, we perform cyclic voltammetry in the STM-BJ setup. For these measurements, we used a tip coated with Apiezon Wax W to ensure a small tip area to reduce background capacitive current.[45] A 1 mM solution of the Blatter radical derivative in anhydrous propylene carbonate with 0.1 M tetrabutylammonium perchlorate (TBAP) as supporting electrolyte was prepared. The radical solution was dropped onto the gold substrate, and 1000 conductance traces were obtained to ensure that the molecule is indeed present. Then, the tip is retracted to ~1 μm above the substrate, and the cyclic voltammetry sweep is performed, i.e. the current at the tip is monitored as the voltage is swept.

Since there is no reference electrode, we referenced the results to the ferrocene oxidation wave. Figure 4.6a shows the cyclic voltammetry sweep of the Blatter radical derivative in blue. The orange trace shows a solution of 1 mM radical with 0.5 mM ferrocene and 0.1 M TBAP in

solution. Clearly, the radical is more easily oxidized than ferrocene by ~0.2 V, which agrees with the bulk cyclic voltammetry measurement on platinum disk (Figure 4.6b).

4.13 Platinum electrode cyclic voltammetry

Cyclic voltammetry was performed using single cell setup with a CH Instruments Electrochemical Analyser Potentiostat. The set up consists of: a) platinum working electrode, b) platinum wire counter electrode, and c) Ag/AgCl reference electrode, all purchased from BASi. Figure 4.6b shows the cyclic voltammogram of the Blatter radical derivative. The measurement was carried out in dichloromethane solution containing 0.1 M of supporting electrolyte, tetrabutylammoniumhexafluorophosphate ($TBAPF_6$), with ~1 mg/mL of the desired compound. A scan rate of 0.1 Vs^{-1} was used. Both redox processes are reversible over several cycles.

4.14 Chemical oxidation study – UV-Vis and NMR

To chemically oxidize the Blatter radical derivative, we use 1 electron oxidants with sufficient oxidation potential. Tris(4-bromophenyl)ammoniumyl hexachloroantimonate (BAHA) has an oxidation potential of 0.70 V vs ferrocene, while silver hexafluoroantimonate ($AgSbF_6$) has an oxidation of 0.65 V vs ferrocene.[46]

For the UV titration, a 10 μM solution of the Blatter radical derivative in dichloromethane (3 mL) was placed in a UV cuvette. A 100 μM solution of BAHA oxidant was added in 50 μL aliquots. Therefore, an addition of 6 aliquots results in a 1:1 ratio of radical to oxidant, leading to full conversion of the radical into its cation. Figure 4.17a shows the resulting UV-Vis spectra after addition of up to 2 equivalents of BAHA. The black and purple traces in both graphs are the neutral radical and closed shell cation respectively. In Figure 4.17b, it can be seen that the addition of BAHA beyond 1 equivalent only increases the peak heights in regions where BAHA absorbs. The

UV-Vis spectrum of BAHA is shown in blue for reference. Therefore, there is no further oxidation occurring.

For the NMR oxidation, a 3 mM solution of the Blatter derivative with 1 equivalent of $AgSbF_6$ in deuterated dichloromethane was prepared. The peaks are reported as follows: ^{1}H-NMR (400 MHz, CD_2Cl_2) δ 8.44 (d, *J* = 8.8 Hz, 2H), 8.28 (d, *J* = 9.2 Hz, 1H), 8.13 (dd, *J* = 9.6, 2.0 Hz, 1H), 7.94 – 7.81 (m, 5H), 7.45 (d, *J* = 8.8 Hz, 2H), 7.35 (d, *J* =2.0 Hz, 1H), 2.60 (s, 3H), 3.58 (s, 3H). The NMR spectrum is shown in Figure 4.18.

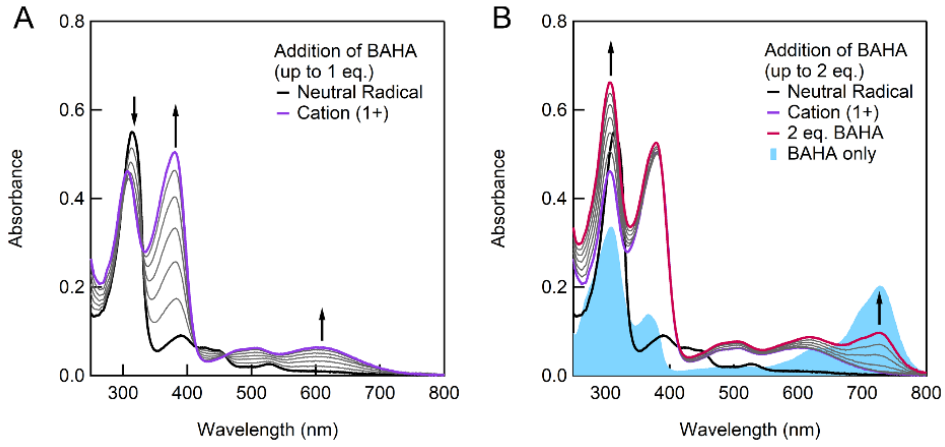

Figure 4.17. (a) Evolution of UV-Vis spectrum of the Blatter radical derivative as 1 equivalent of BAHA is added in six steps. The spectrum of the neutral radical is the bold black trace, with the cation in purple. (b) Evolution of the UV-Vis spectrum as 1 additional equivalent of BAHA is added in six steps. The end point is shown in red. The shaded light blue graph is the spectrum of the BAHA oxidant.

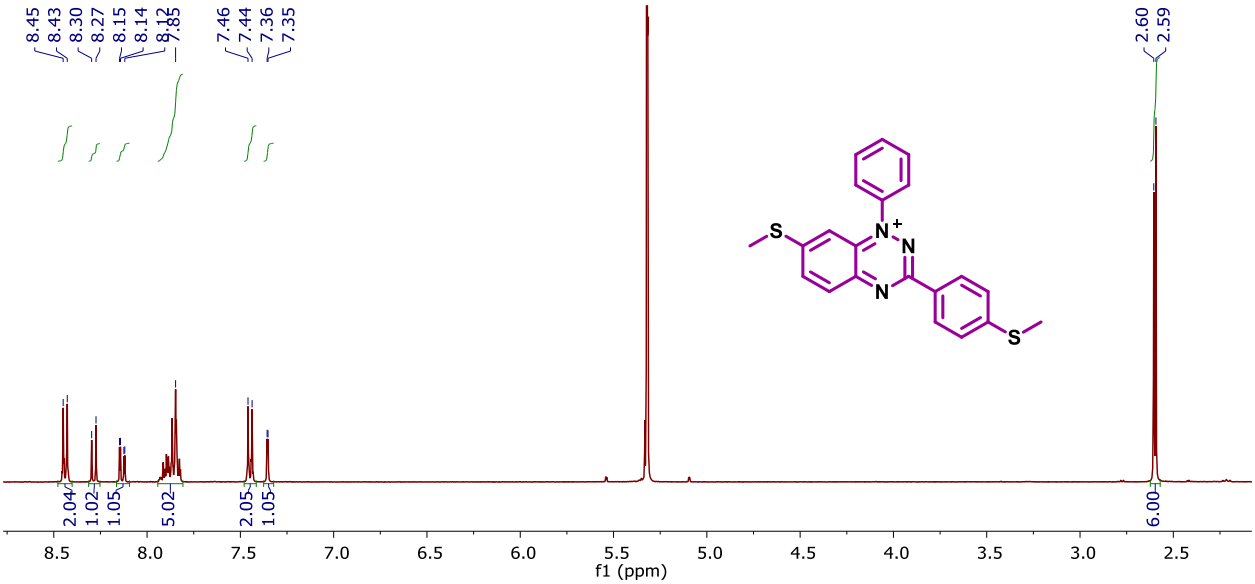

Figure 4.18. NMR spectrum of the oxidized Blatter radical derivative.

4.15 Conductance measurement of the oxidized radical

To obtain the conductance trace of the oxidized the radical shown in Figure 4.4a, we used tris(4-bromophenyl)ammoniumyl hexachloroantimonate (BAHA) to chemically generate the oxidized species. A 0.4 mM solution of the Blatter radical derivative with 1 equivalent of BAHA in dry dichloromethane was prepared. The solution was stirred for 10 min at room temperature and diluted to 0.1 mM with trichlorobenzene. This solution of 0.1 mM cation in 1:3 dichloromethane to trichlorobenzene mixture was then dropped directly onto the gold substrate in the STM setup, and break junction measurements were performed.

4.16 Optimized coordinates for gas phase DFT calculations

Reduced radical (-1)

Center Number	Element	Coordinates (angstroms)			Center Number	Element	Coordinates (angstroms)		
		X	Y	Z			X	Y	Z
1	C	-3.786300	-1.858783	-0.309028	23	S	-5.500697	-2.048258	-0.782692
2	C	-3.076037	-2.932258	0.236982	24	C	-6.381212	-1.381491	0.688217
3	C	-1.725770	-2.794776	0.554798	25	S	6.964980	-0.543820	-0.438082
4	C	-1.041531	-1.575809	0.370162	26	C	7.457820	0.213230	1.160332
5	C	-1.805802	-0.458214	-0.090453	27	H	-3.580840	-3.881209	0.396908
6	C	-3.124967	-0.623322	-0.496089	28	H	-1.152566	-3.634223	0.937793
7	N	0.309745	-1.491724	0.565992	29	H	-3.668864	0.207981	-0.929649
8	C	0.871377	-0.378626	0.043820	30	H	2.509084	-2.367438	0.723275
9	N	0.296925	0.718365	-0.403110	31	H	5.012224	-2.459045	0.551455
10	N	-1.098474	0.771078	-0.132574	32	H	5.002365	1.483847	-1.153678
11	C	2.361339	-0.402994	-0.091048	33	H	2.518781	1.555262	-0.947459
12	C	-1.642986	2.037648	-0.004023	34	H	-3.493174	1.426292	0.947157
13	C	3.077796	-1.534340	0.325934	35	H	-4.389918	3.686304	1.185681
14	C	4.467200	-1.577116	0.226523	36	H	-3.089393	5.673398	0.403217
15	C	5.173191	-0.486997	-0.298037	37	H	-0.831241	5.302970	-0.601725
16	C	4.461447	0.641507	-0.731533	38	H	0.078290	3.020090	-0.839937
17	C	3.074495	0.683647	-0.621662	39	H	-7.454411	-1.456891	0.487964
18	C	-2.914305	2.264467	0.580706	40	H	-6.121662	-0.333023	0.853356
19	C	-3.413988	3.554169	0.722546	41	H	-6.139142	-1.962230	1.581763
20	C	-2.687429	4.669915	0.295489	42	H	8.550975	0.230256	1.184405
21	C	-1.425919	4.454919	-0.266990	43	H	7.088146	-0.378890	2.000536
22	C	-0.902583	3.175303	-0.413259	44	H	7.080417	1.235274	1.238846

Neutral radical

Center Number	Element	Coordinates (angstroms)			Center Number	Element	Coordinates (angstroms)		
		X	Y	Z			X	Y	Z
1	C	-3.842082	-1.645845	-0.055901	23	S	-5.614615	-1.610149	-0.228363
2	C	-3.088226	-2.821407	0.117179	24	C	-6.071817	-3.369878	-0.352785
3	C	-1.707704	-2.750194	0.225738	25	S	6.978972	0.036893	-0.089750
4	C	-1.028295	-1.518319	0.187647	26	C	7.586046	-1.679264	-0.016575
5	C	-1.808494	-0.329896	0.064402	27	H	-3.572630	-3.789496	0.156644
6	C	-3.196154	-0.403518	-0.088256	28	H	-1.107039	-3.647269	0.332136
7	N	0.336771	-1.489615	0.237451	29	H	-3.775193	0.498574	-0.242789
8	C	0.905742	-0.284373	0.103747	30	H	2.618903	-2.347988	0.147887
9	N	0.276076	0.892999	0.013108	31	H	5.080523	-2.301332	0.070690
10	N	-1.088367	0.867030	0.067380	32	H	4.964069	2.005589	-0.104971
11	C	2.387732	-0.220216	0.062089	33	H	2.498894	1.927746	-0.025634
12	C	-1.694160	2.161640	0.050608	34	H	-3.014670	1.763542	1.708473
13	C	3.141151	-1.399875	0.090970	35	H	-4.024265	4.024664	1.673850
14	C	4.533266	-1.366158	0.047653	36	H	-3.246435	5.714870	0.023535
15	C	5.207795	-0.140566	-0.025500	37	H	-1.446523	5.125031	-1.588292
16	C	4.455570	1.046975	-0.052200	38	H	-0.447852	2.845048	-1.557626
17	C	3.069446	1.006418	-0.008913	39	H	-7.150166	-3.378621	-0.523403
18	C	-2.693176	2.492936	0.973353	40	H	-5.857770	-3.910427	0.571752
19	C	-3.251853	3.770294	0.954492	41	H	-5.574728	-3.851347	-1.197675
20	C	-2.810393	4.720736	0.032669	42	H	8.674889	-1.606882	-0.051548
21	C	-1.799045	4.389319	-0.871741	43	H	7.242683	-2.263347	-0.873370
22	C	-1.238224	3.114432	-0.867104	44	H	7.293491	-2.168609	0.915158

Oxidized radical (+1)

Center Number	Element	Coordinates (angstroms)			Center Number	Element	Coordinates (angstroms)		
		X	Y	Z			X	Y	Z
1	C	-3.844123	-1.601616	-0.072789	23	S	-5.590297	-1.583013	-0.245720
2	C	-3.075982	-2.807398	0.080510	24	C	-6.093086	-3.336861	-0.203390
3	C	-1.714760	-2.774448	0.177828	25	S	6.948960	0.055066	-0.059946
4	C	-1.016406	-1.528733	0.135390	26	C	7.587452	-1.651791	-0.022313
5	C	-1.802163	-0.320398	0.035627	27	H	-3.582541	-3.764284	0.105364
6	C	-3.198341	-0.369003	-0.092015	28	H	-1.123970	-3.678499	0.271236
7	N	0.309286	-1.505059	0.166311	29	H	-3.766773	0.544049	-0.214354
8	C	0.923148	-0.304445	0.085916	30	H	2.634344	-2.374581	0.106143
9	N	0.249947	0.870012	0.056007	31	H	5.081531	-2.302595	0.045508
10	N	-1.065309	0.841418	0.051081	32	H	4.939391	2.011705	-0.056337
11	C	2.379730	-0.234621	0.055769	33	H	2.487171	1.927323	0.004341
12	C	-1.685241	2.154582	0.041286	34	H	-2.829026	1.798863	1.841331
13	C	3.140832	-1.417103	0.069116	35	H	-3.825875	4.071953	1.827951
14	C	4.527086	-1.372372	0.035096	36	H	-3.223285	5.684052	0.037903
15	C	5.198321	-0.136918	-0.012135	37	H	-1.610003	5.033127	-1.734316
16	C	4.435224	1.050865	-0.023337	38	H	-0.600740	2.755662	-1.719816
17	C	3.054736	1.004165	0.009645	39	H	-7.178197	-3.312437	-0.319833
18	C	-2.585542	2.501262	1.051480	40	H	-5.854298	-3.801336	0.754789
19	C	-3.135350	3.782165	1.043170	41	H	-5.664135	-3.898302	-1.035032
20	C	-2.788949	4.689767	0.039571	42	H	8.673881	-1.551150	-0.049714
21	C	-1.880108	4.326172	-0.957193	43	H	7.263226	-2.219069	-0.896983
22	C	-1.313155	3.053733	-0.958964	44	H	7.303287	-2.163927	0.899057

4.17 Synthetic details

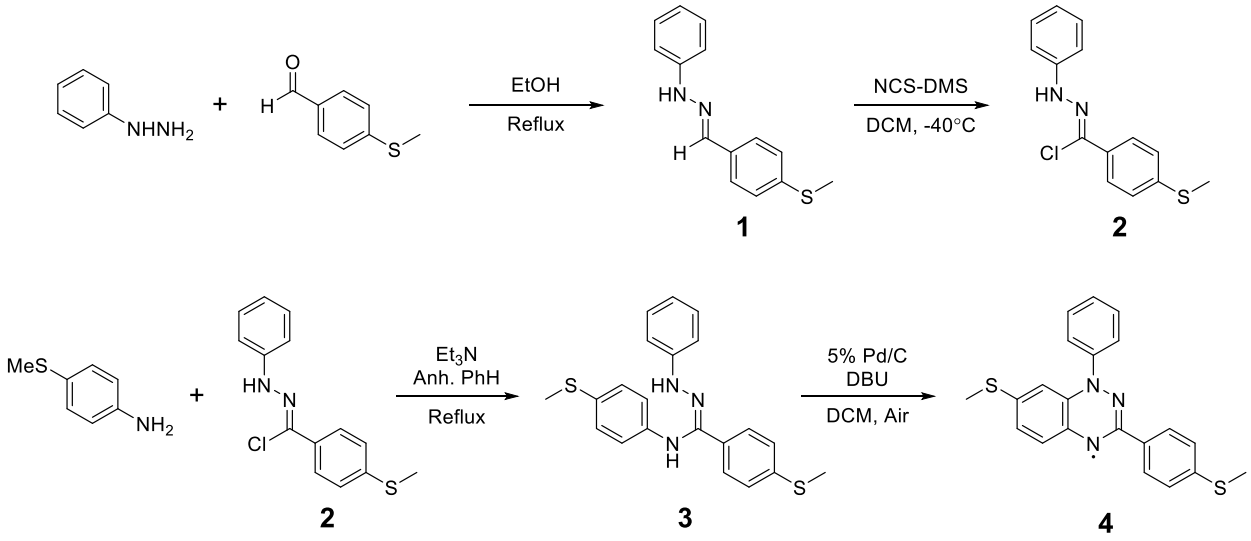

Figure 4.19. Synthetic scheme of the Blatter radical derivative with two thiomethyl linkers.

Compound 1 – Prepared according to a report method with different starting reagents.[47]

Phenylhydrazine (9.4g, 87.4mmol, 1eq) was dissolved in ethanol (200mL). 4-(methylthio)benzaldehyde (13.3g, 87.4mmol, 1eq) was slowly added with stirring. A precipitate formed almost immediately. The solution was refluxed for a further 5h, then cooled to room temperature. The precipitate was collected and recrystallized from ethanol to yield the desired hydrazone **1** as an off-white solid (17.1g, 81%). ^{1}H-NMR (400 MHz, CD_2Cl_2) δ 7.66 (s, 1H), 7.59 (d, *J* = 8.4 Hz, 2H), 7.30 – 7.22 (m, 4H), 7.11 (d, *J* = 7.6 Hz, 2H), 6.86 (t, *J* = 7.6 Hz, 1H), 2.51 (s, 3H). ^{13}C-NMR (125 MHz, CD_2Cl_2) δ 144.80, 139.17, 136.93, 132.22, 129.25, 126.44, 126.18, 119.93, 112.54, 15.31. HRMS (ASAP+) Calculated $[M+H]^+$ 243.0956, observed 243.0954.

Compound 2 – Prepared according to a report method with different starting reagents.[48]

This hydrazonyl chloride was prepared via a reported procedure using the Corey-Kim reagent (NCS-DMS). *N*-chlorosuccinimide (2.15g, 16.1mmol, 1.3eq) was dissolved in dry DCM (160mL) under an inert atmosphere and cooled to 0°C. Dimethyl sulfide (1.16g, 18.6mmol, 1.5eq) was added to the stirring solution, which was then stirred for a further 5 min at 0°C. The solution was cooled to -40°C, and the hydrazone **1** (3.0g, 12.4mmol, 1eq) was added as a solid. The solution was stirred at -40°C for 1.5h and allowed to warm to 0°C over 1h. The reaction was quenched with cold water and extracted twice with DCM. The organic extracts were washed with water and brine and dried over $MgSO_4$. The solvent was removed, and the crude product was purified by column chromatography (silica gel, 20% DCM in hexanes) to yield the product as an off-white solid (1.86g, 54%). ^{1}H-NMR (400 MHz, CD_2Cl_2) δ 8.06 (s, 1H), 7.85 (d, *J* = 8.8 Hz, 2H), 7.34 – 7.25 (m, 4H), 7.21 – 7.16 (m, 2H), 6.94 (t, *J* = 7.6 Hz, 1H), 2.52 (s, 3H). ^{13}C-NMR (125 MHz, CD_2Cl_2)

δ 143.46, 140.66, 130.97, 129.34, 126.58, 125.60, 124.40, 121.05, 113.29, 15.08. HRMS (ASAP+) Calculated $[M+H]^+$ 277.0566, observed 277.0560.

Compound 3 – Prepared according to a report method with different starting reagents.[19]

The hydrazonyl chloride **2** (1.80g, 6.50mmol, 1eq) and 4-(methylthio)aniline (0.91g, 6.50mmol, 1eq) were dissolved in dry benzene (20mL) under an inert atmosphere. Triethylamine (0.99g, 9.76mmol, 1.5eq) was added, and the solution was refluxed for 3-4h. The reaction was quenched with cold water and diluted with ethyl acetate. The organic extracts were washed with water and brine and dried over $MgSO_4$. After removing the solvent, the crude product was purified by column chromatography (silica gel, 10-20% ethyl acetate in hexanes) to yield the amidrazone as an off-white solid (0.81g, 33%). ^{1}H-NMR (400 MHz, CD_2Cl_2) δ 7.65 – 7.59 (m, 3H), 7.28 – 7.15 (m, 6H), 7.13 – 7.07 (m, 2H), 6.85 (t, *J* = 7.6 Hz, 1H), 6.67 (d, *J* = 8.4 Hz, 2H), 5.72 (s, 1H), 2.49 (s, 3H), 2.42 (s, 3H). ^{13}C-NMR (125 MHz, $CDCl_3$) δ 145.14, 139.80, 139.77, 137.89, 131.12, 129.59, 129.38, 129.13, 127.14, 126.01, 120.25, 117.17, 113.43, 17.62, 15.48. HRMS (ESI+) Calculated $[M+H]^+$ 380.1255, observed 380.1261.

Compound 4 – Prepared according to a report method with different starting reagents.[19]

The amidrazone **3** (250mg, 0.66mmol, 1eq) was dissolved in dry DCM (10mL). DBU (107mg, 0.69mmol, 1.05eq) and 5% Pd/C (22.4mg, 1.6% mol eq) were added and the solution was stirred in air at room temperature for 6h. The solution was filtered through a celite bed and the solvent was removed to obtain the crude product, which was purified by column chromatography (silica gel, 10% ethyl acetate in hexanes) to yield the radical product as a dark brown solid (135mg, 54%).

HRMS (ASAP+) Calculated $[M+H]^+$ 377.1029, observed 380.1261. The EPR and UV spectra are presented in Figure 4.1b and Figure 4.17a respectively.

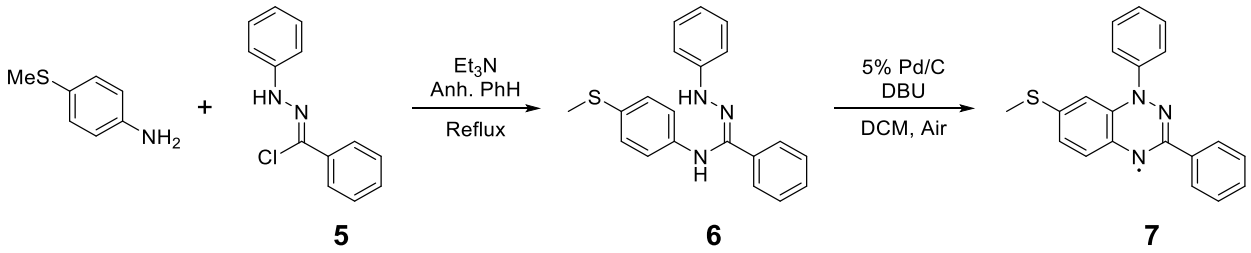

5 **6** **7**

Figure 4.20. Synthetic scheme of the Blatter radical derivative with only one thiomethyl linker, used in section 4.11.

Compound 6 – Prepared according to a report method with different starting reagents.[19]

The hydrazonyl chloride **5** (1.48g, 6.42mmol, 1eq) and 4-(methylthio)aniline (0.94g, 6.74mmol, 1.05eq) were dissolved in dry benzene (15mL) under an inert atmosphere. Triethylamine (0.97g, 9.62mmol, 1.5eq) was added, and the solution was refluxed for 4h. The reaction was quenched with cold water and diluted with ethyl acetate. The organic extracts were washed with water and brine and dried over $MgSO_4$. After removing the solvent, the crude product was purified by column chromatography (silica gel, 10-20% ethyl acetate in hexanes) to yield the amidrazone as a low melting point yellow solid (0.50g, 23%). ^{1}H-NMR (500 MHz, DMSO-d_6) δ 9.16 (s, 1H), 8.09 (s, 1H), 7.61 – 7.57 (m, 2H), 7.38 – 7.28 (m, 3H), 7.23 – 7.14 (m, 4H), 7.10 (d, J = 8.7, 2H), 6.73 (tt, J = 7.0, 1.4 Hz, 1H), 6.58 (d, J = 8.7, 2H), 2.36 (s, 3H). ^{13}C-NMR (125 MHz, DMSO-d_6) δ 145.76, 141.17, 136.97, 135.04, 128.92, 128.71, 128.26, 128.17, 126.68, 126.51, 118.57, 117.18, 112.63, 16.69. HRMS (ESI+) Calculated $[M+H]^+$ 334.1378, observed 334.1370.

Compound 7 – Prepared according to a report method with different starting reagents.[19]

The amidrazone **6** (410mg, 1.23mmol, 1eq) was dissolved in dry DCM (8mL). DBU (190mg, 1.23mmol, 1eq) and 5% Pd/C (42mg, 1.6% mol eq) were added and the solution was stirred in air at room temperature for 6h. The solution was filtered through a celite bed and the solvent was removed to obtain the crude product, which was purified by column chromatography (silica gel, 15% ethyl acetate in hexanes) to yield the radical product as a dark brown solid (203mg, 50%). HRMS (ASAP+) Calculated $[M+H]^+$ 331.1143, observed 331.1147. The EPR is shown in Figure 4.21 below.

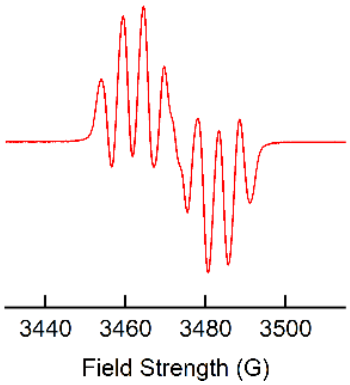

*Figure 4.21. EPR spectrum of Blatter radical **7** with one thiomethyl group. The structure is shown in the inset of Figure 4.16a.*

4.18 Acknowledgements

The experimental work was supported primarily by the National Science Foundation (award number DMR-1507440). G.L. thanks the Center for Precision Assembly of Superstratic and Superatomic Solids at Columbia University, an NSF MRSEC (award number DMR-1420634) for funding. Gas phase DFT calculations used the Extreme Science and Engineering Discovery Environment (XSEDE) startup allocation TG-DMR150018. XSEDE is supported by NSF grant number ACI-1548562.[49] J.Z.L. thanks the A*STAR Graduate Academy in Singapore for a

graduate fellowship. D.C. and G.K. acknowledge partial financial support from the Slovenian Research Agency (program number P1-0112). G.K. acknowledges financial support from the SIR grant SUNDYN (Nr. RBSI14G7TL, CUP B82I15000910001) of the Italian Ministry of Education, Universities and Research MIUR. We thank Steffen Jockusch for performing EPR spectroscopy and Brandon Fowler for mass spectrometry.

4.19 References

(1) Sanvito, S. *Chem. Soc. Rev.* **2011**, *40*, 3336-3355.

(2) Mas-Torrent, M.; Crivillers, N.; Rovira, C.; Veciana, J. *Chem. Rev.* **2012**, *112*, 2506-2527.

(3) Mas-Torrent, M.; Crivillers, N.; Mugnaini, V.; Ratera, I.; Rovira, C.; Veciana, J. *J. Mater. Chem.* **2009**, *19*, 1691-1695.

(4) Herrmann, C.; Solomon, G. C.; Ratner, M. A. *J. Am. Chem. Soc.* **2010**, *132*, 3682-3684.

(5) Hicks, R. G. *Org. Biomol. Chem.* **2007**, *5*, 1321-1338.

(6) Ratera, I.; Veciana, J. *Chem. Soc. Rev.* **2012**, *41*, 303-349.

(7) Campos, L. M.; Garcia-Garibay, M. A. In *Reviews of Reactive Intermediate Chemistry*; Platz, M. S., Moss, R. A., Jones Jr., M., Eds.; John Wiley & Sons, Inc.: New Jersey, USA, 2007, p 271-331.

(8) Mugnaini, V.; Calzolari, A.; Ovsyannikov, R.; Vollmer, A.; Gonidec, M.; Alcon, I.; Veciana, J.; Pedio, M. *J. Phys. Chem. Lett.* **2015**, *6*, 2101-2106.

(9) Arantes, C.; Chernick, E. T.; Gruber, M.; Rocco, M. L. M.; Chassé, T.; Tykwinski, R. R.; Casu, M. B. *J. Phys. Chem. C* **2016**, *120*, 3289-3294.

(10) Kakavandi, R.; Savu, S.-A.; Caneschi, A.; Casu, M. B. *J. Phys. Chem. C* **2013**, *117*, 26675-26679.

(11) Savu, S.-A.; Biswas, I.; Sorace, L.; Mannini, M.; Rovai, D.; Caneschi, A.; Chassé, T.; Casu, M. B. *Chem. - Eur. J.* **2013**, *19*, 3445-3450.

(12) Kakavandi, R.; Savu, S.-A.; Sorace, L.; Rovai, D.; Mannini, M.; Casu, M. B. *J. Phys. Chem. C* **2014**, *118*, 8044-8049.

(13) Frisenda, R.; Gaudenzi, R.; Franco, C.; Mas-Torrent, M.; Rovira, C.; Veciana, J.; Alcon, I.; Bromley, S. T.; Burzurí, E.; van der Zant, H. S. J. *Nano Lett.* **2015**, *15*, 3109-3114.

(14) Yuan, L.; Franco, C.; Crivillers, N.; Mas-Torrent, M.; Cao, L.; Sangeeth, C. S. S.; Rovira, C.; Veciana, J.; Nijhuis, C. A. *Nat. Commun.* **2016**, *7*, 12066.

(15) Hayakawa, R.; Karimi, M. A.; Wolf, J.; Huhn, T.; Zöllner, M. S.; Herrmann, C.; Scheer, E. *Nano Lett.* **2016**, *16*, 4960-4967.

(16) Sugawara, T.; Minamoto, M.; Matsushita, M. M.; Nickels, P.; Komiyama, S. *Phys. Rev. B* **2008**, *77*, 235316.

(17) Blatter, H. M.; Lukaszewski, H. *Tetrahedron Lett.* **1968**, *9*, 2701-2705.

(18) Constantinides, C. P.; Koutentis, P. A.; Krassos, H.; Rawson, J. M.; Tasiopoulos, A. J. *J. Org. Chem.* **2011**, *76*, 2798-2806.

(19) Koutentis, P. A.; Lo Re, D. *Synthesis* **2010**, *12*, 2075-2079.

(20) Berezin, A. A.; Zissimou, G.; Constantinides, C. P.; Beldjoudi, Y.; Rawson, J. M.; Koutentis, P. A. *J. Org. Chem.* **2014**, *79*, 314-327.

(21) Constantinides, C. P.; Obijalska, E.; Kaszyński, P. *Org. Lett.* **2016**, *18*, 916-919.

(22) Karecla, G.; Papagiorgis, P.; Panagi, N.; Zissimou, G. A.; Constantinides, C. P.; Koutentis, P. A.; Itskos, G.; Hayes, S. C. *New J. Chem.* **2017**, *41*, 8604-8613.

(23) Savva, A. C.; Mirallai, S. I.; Zissimou, G. A.; Berezin, A. A.; Demetriades, M.; Kourtellaris, A.; Constantinides, C. P.; Nicolaides, C.; Trypiniotis, T.; Koutentis, P. A. *J. Org. Chem.* **2017**, *82*, 7564-7575.

(24) Hutchison, K.; Srdanov, G.; Menon, R.; Gabriel, J.-C.; Knight, B.; Wudl, F. *Synth. Met.* **1997**, *86*, 2147-2148.

(25) Ciccullo, F.; Gallagher, N. M.; Geladari, O.; Chassé, T.; Rajca, A.; Casu, M. B. *ACS Appl. Mater. Interfaces* **2016**, *8*, 1805-1812.

(26) Xu, B.; Tao, N. J. *Science* **2003**, *301*, 1221-1223.

(27) Wu, S.; Gonzalez, M. T.; Huber, R.; Grunder, S.; Mayor, M.; Schonenberger, C.; Calame, M. *Nat. Nanotechnol.* **2008**, *3*, 569-574.

(28) Frisenda, R.; Janssen, V. A. E. C.; Grozema, F. C.; van der Zant, H. S. J.; Renaud, N. *Nat. Chem.* **2016**, *8*, 1099.

(29) Magyarkuti, A.; Adak, O.; Halbritter, A.; Venkataraman, L. *Nanoscale* **2018**, *10*, 3362-3368.

(30) Heimel, G.; Zojer, E.; Romaner, L.; Brédas, J.-L.; Stellacci, F. *Nano Lett.* **2009**, *9*, 2559-2564.

(31) Mielke, J.; Hanke, F.; Peters, M. V.; Hecht, S.; Persson, M.; Grill, L. *J. Am. Chem. Soc.* **2015**, *137*, 1844-1849.

(32) Smoluchowski, R. *Phys. Rev.* **1941**, *60*, 661-674.

(33) Jia, J.; Kara, A.; Pasquali, L.; Bendounan, A.; Sirotti, F.; Esaulov, V. A. *J. Chem. Phys.* **2015**, *143*, 104702.

(34) Pasquali, L.; Terzi, F.; Seeber, R.; Nannarone, S.; Datta, D.; Dablemont, C.; Hamoudi, H.; Canepa, M.; Esaulov, V. A. *Langmuir* **2011**, *27*, 4713-4720.

(35) Cossaro, A.; Dell'Angela, M.; Verdini, A.; Puppin, M.; Kladnik, G.; Coreno, M.; de Simone, M.; Kivimäki, A.; Cvetko, D.; Canepa, M.; Floreano, L. *J. Phys. Chem. C* **2010**, *114*, 15011-15014.

(36) Urban, C.; Écija, D.; Wang, Y.; Trelka, M.; Preda, I.; Vollmer, A.; Lorente, N.; Arnau, A.; Alcamí, M.; Soriano, L.; Martín, N.; Martín, F.; Otero, R.; Gallego, J. M.; Miranda, R. *J. Phys. Chem. C* **2010**, *114*, 6503-6510.

(37) Frisch, M. J.; Trucks, G. W.; Schlegel, H. B.; Scuseria, G. E.; Robb, M. A.; Cheeseman, J. R.; Scalmani, G.; Barone, V.; Mennucci, B.; Petersson, G. A.; Nakatsuji, H.; Caricato, M.; Li, X.; Hratchian, H. P.; Izmaylov, A. F.; Bloino, J.; Zheng, G.; Sonnenberg, J. L.; Hada, M.; Ehara, M.; Toyota, K.; Fukuda, R.; Hasegawa, J.; Ishida, M.; Nakajima, T.; Honda, Y.; Kitao, O.; Nakai, H.; Vreven, T.; Montgomery, J. A.; Peralta, J. E.; Ogliaro, F.; Bearpark, M.; Heyd, J. J.; Brothers, E.; Kudin, K. N.; Staroverov, V. N.; Kobayashi, R.; Normand, J.; Raghavachari, K.; Rendell, A.; Burant, J. C.; Iyengar, S. S.; Tomasi, J.; Cossi, M.; Rega, N.; Millam, J. M.; Klene, M.; Knox, J. E.; Cross, J. B.; Bakken, V.; Adamo, C.; Jaramillo, J.; Gomperts, R.; Stratmann, R. E.; Yazyev, O.; Austin, A. J.; Cammi, R.; Pomelli, C.; Ochterski, J. W.; Martin, R. L.; Morokuma, K.; Zakrzewski, V. G.; Voth, G. A.; Salvador, P.; Dannenberg, J. J.; Dapprich, S.; Daniels, A. D.; Farkas; Foresman, J. B.; Ortiz, J. V.; Cioslowski, J.; Fox, D. J. Gaussian 09, Revision D.01, Gaussian, Inc., Wallingford CT, 2009.

(38) Mortensen, J. J.; Hansen, L. B.; Jacobsen, K. W. *Phys. Rev. B* **2005**, *71*, 035109.

(39) Enkovaara, J.; Rostgaard, C.; Mortensen, J. J.; Chen, J.; Dułak, M.; Ferrighi, L.; Gavnholt, J.; Glinsvad, C.; Haikola, V.; Hansen, H. A.; Kristoffersen, H. H.; Kuisma, M.; Larsen, A. H.; Lehtovaara, L.; Ljungberg, M.; Lopez-Acevedo, O.; Moses, P. G.; Ojanen, J.; Olsen, T.; Petzold, V.; Romero, N. A.; Stausholm-Møller, J.; Strange, M.; Tritsaris, G. A.; Vanin, M.; Walter, M.; Hammer, B.; Häkkinen, H.; Madsen, G. K. H.; Nieminen, R. M.; Nørskov, J. K.; Puska, M.; Rantala, T. T.; Schiøtz, J.; Thygesen, K. S.; Jacobsen, K. W. *J. Phys.: Condens. Matter* **2010**, *22*, 253202.

(40) Bahn, S. R.; Jacobsen, K. W. *Comput. Sci. Eng.* **2002**, *4*, 56-66.

(41) Yan, B.; Cramen, J.; McDonald, R.; Frank, N. L. *Chem. Commun.* **2011**, *47*, 3201-3203.

(42) Batra, A.; Kladnik, G.; Vázquez, H.; Meisner, J. S.; Floreano, L.; Nuckolls, C.; Cvetko, D.; Morgante, A.; Venkataraman, L. *Nat. Commun.* **2012**, *3*, 1086.

(43) Adak, O.; Kladnik, G.; Bavdek, G.; Cossaro, A.; Morgante, A.; Cvetko, D.; Venkataraman, L. *Nano Lett.* **2015**, *15*, 8316-8321.

(44) Adak, O.; Rosenthal, E.; Meisner, J.; Andrade, E. F.; Pasupathy, A. N.; Nuckolls, C.; Hybertsen, M. S.; Venkataraman, L. *Nano Lett.* **2015**, *15*, 4143-4149.

(45) Nagahara, L. A.; Thundat, T.; Lindsay, S. M. *Rev. Sci. Instrum.* **1989**, *60*, 3128-3130.

(46) Connelly, N. G.; Geiger, W. E. *Chem. Rev.* **1996**, *96*, 877-910.

(47) Vantomme, G.; Jiang, S.; Lehn, J.-M. *J. Am. Chem. Soc.* **2014**, *136*, 9509-9518.

(48) Patel, H. V.; Vyas, K. A.; Pandey, S. P.; Fernandes, P. S. *Tetrahedron* **1996**, *52*, 661-668.

(49) Towns, J.; Cockerill, T.; Dahan, M.; Foster, I.; Gaither, K.; Grimshaw, A.; Hazlewood, V.; Lathrop, S.; Lifka, D.; Peterson, G. D.; Roskies, R.; Scott, J. R.; Wilkins-Diehr, N. *Comput. Sci. Eng.* **2014**, *16*, 62-74.

5. Molecular Structure Affects the Charge State of the Blatter Radical on Gold

Abstract: The stable, neutral Blatter radical is an organic radical that has been studied for its magnetic and charge transport properties. However, to fully develop such organic radicals for electronic and spintronic applications, the radical-metal interface must be well understood. Modifications to the molecule's structure may also affect its interaction with the metal, so it is also important to probe different derivatives within the same class of compounds. Here, we study 3 derivatives of the Blatter radical functionalized with and without terminal thiomethyl groups. We utilize X-ray spectroscopy to probe their electronic structure on gold. XPS and NEXAFS measurements show that the Blatter radical can retain its unpaired spin on gold in a monolayer. However, one of the thiomethyl groups causes charge transfer from metal to radical, resulting in loss of radical character.

5.1 Preface

This chapter is based on a manuscript in preparation titled *Molecular Structure Affects the Charge State of the Blatter Radical on Gold* by Jonathan Z. Low, Gregor Kladnik, Giacomo Lovat, Elango Kumarasamy, Luis M. Campos, Dean Cvetko, Alberto Morgante and Latha Venkataraman.

5.2 Introduction

The interaction of organic molecules with metals can alter their electronic structure. Therefore, characterization of the metal-molecule interface is vital for improving the performance of organic electronic devices.[1] One important class of molecules that has been gaining interest in energy storage and conversion applications are stable organic radicals.[2-4] Furthermore, due to the presence of the unpaired spin and long spin lifetimes,[5] they have also been advocated as candidates for building metal-free magnetic and spintronic devices.[3,6] However, due to their open shell nature, radicals are even more susceptible to strong interactions with the substrate or metal electrodes,

which may cause the loss of radical character. By probing the radical-metal interface, one can determine the nature of such metal-molecule interactions and make appropriate modifications to the chemical structure of the molecules or to the surface of the metal to avoid any undesirable interactions.

Several organic radical systems deposited on various surfaces have been studied by different X-ray spectroscopic techniques. It is known that perchlorinated trityl radicals interact only weakly with gold, but their paramagnetism is quenched on silver.[7] Nitronyl-nitroxide radicals are also inert on gold and SiO_2,[8,9] but form N-Ti bonds that disrupt the radical character on TiO_2.[10] Pentacene derivatives decorated with TEMPO radicals on SiO_2 were found to have a slightly altered electronic structure depending on how the films were processed, although no specific substrate-molecule interactions were probed in this study.[11] Finally, other classes of radicals have also been studied by scanning tunneling microscopy on gold substrates and been found to retain their spin.[12-15] In all the above examples, one molecule is investigated on different substrates, but there have been no reports that establish structure-property relationships by exploring the relationship between molecular structure and the resulting interaction with the substrate. Such a strategy takes advantage of the modularity of synthetic chemistry to establish rational design principles so that materials with desirable characteristics can be developed.

In this report, we investigate how changes to the structure of the Blatter radical affects its interaction with a substrate. The Blatter radical is a benzotriazinyl-based radical in which the unpaired electron is stabilized via delocalization over three nitrogen atoms.[16] Previously, X-ray photoelectron spectroscopy (XPS) revealed that a pyrene fused derivative of the Blatter radical retains its spin on SiO_2.[17] Here, we study films of the native Blatter radical, B0, deposited on a gold substrate, as well as derivatives with one and two thiomethyl groups, B1 and B2 (Figure 5.1).

Using a combination of XPS and near edge X-ray absorption fine structure spectroscopy (NEXAFS), we analyze how strongly each of these radicals couple to gold and whether their electronic structure changes as a result. We find that B2 is the only derivative that undergoes charge transfer from metal to molecule, resulting in a closed shell system. Neither B0 nor B1 lose their radical character despite their similar structure and similar proximity of the radical orbital to the Fermi energy (E_F) of gold.

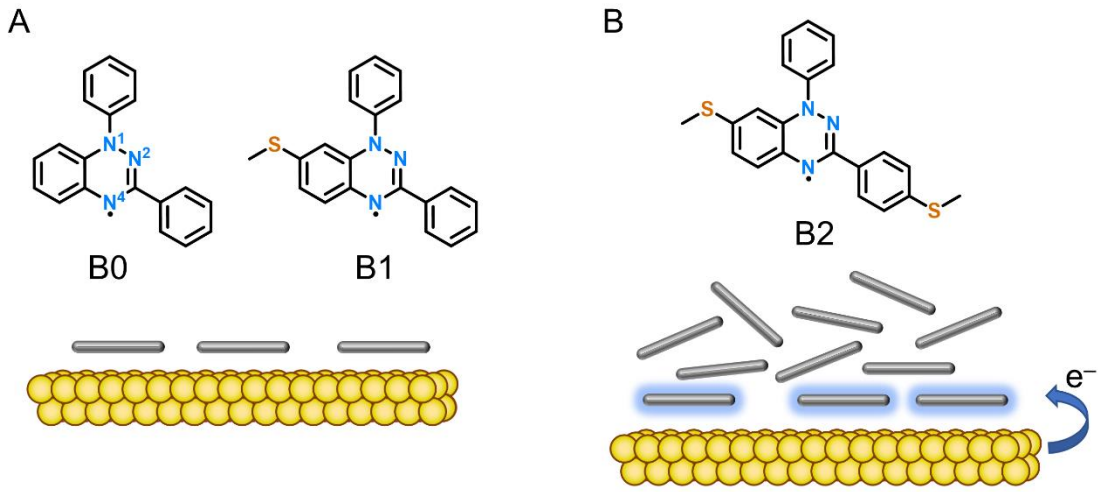

Figure 5.1. (a) Structure of the Blatter radicals B0 and B1 with schematic of the flat monolayer on gold. No charge transfer is observed in both cases. (b) Structure of the Blatter radical B2 and schematic of the multilayer on gold. Here, the first layer of molecules gains an electron from the substrate.

5.3 Results and discussion

We synthesized Blatter radicals B0, B1 and B2 using the method developed by Koutentis et al.[18] B0 is a known compound,[16,18] while the characterization of B1 and B2 were described in chapter 4, section 4.17. The EPR spectra of all 3 molecules show the expected seven-line splitting pattern due to the coupling of the radical electron with 3 nitrogen atoms (Figure 5.2). The radicals were then evaporated onto a pristine Au(111) surface in an ultra-high vacuum (UHV) chamber (see chapter 4, section 4.6 for details). The thickness of the films was controlled by the evaporation

time and substrate temperature. We prepared monolayer and multilayer films of each radical to compare the electronic structure of molecules that are in direct contact with the substrate (monolayer) with those that are not electronically coupled to the substrate (multilayer).

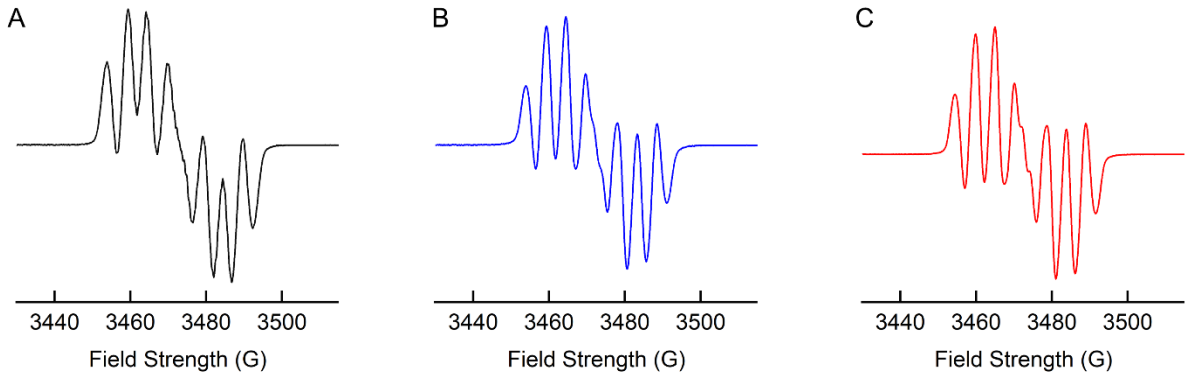

Figure 5.2. EPR spectra of (a) B0, (b) B1, and (c) B2.

We first use XPS to determine the number of chemically inequivalent nitrogen and sulfur atoms in the system. Figures 5.3a and 5.3b show that the monolayer films of B0 and B1 both contain 3 nitrogen 1s peaks, corresponding to 3 nitrogen atoms that are in different environments. Following the assignment of Cicullo et al. and our previous work (see chapter 4), the lowest binding energy peak is due to the radical nitrogen (N4 in Figure 5.1a), while the highest binding energy peak is due to the nitrogen on which the phenyl group is attached (N1).[17] B0 and B1 therefore maintain their radical character in a monolayer. In the XPS of the B2 monolayer however, only 2 peaks are seen, indicating that its electronic structure is different from the other radicals (Figure 5.3c). The multilayer nitrogen XPS of B2 (Figure 5.3d) further shows that the 3 chemically inequivalent nitrogen atoms are recovered when the molecules are not in contact with the substrate. The three peaks are not well defined due to damage from synchrotron radiation as we showed in chapter 4.

Additional insight to the incongruent behavior of B2 in the monolayer is provided by its sulfur 2p XPS, where there are 2 distinct overlapping doublets and therefore 2 sulfur environments (Figure 5.3e). We compare this to the multilayer of B2 and the monolayer of B1, which contrastingly only have 1 sulfur doublet (Figures 5.3d and 5.3f). We therefore deduce that the lower binding energy sulfur peak of B2 is therefore due to the sulfur on the right (as drawn in Figure 5.1b since the B1 monolayer does not have this peak. Furthermore, the lower binding energy peak only occurs when B2 is in contact with the substrate, since it is not present in the spectrum of the multilayer. Taken together, we hypothesize that there is a unique interaction of B2 with the gold substrate that alters its electronic structure, leading to a change in its nitrogen and sulfur XPS spectrum. This interaction is not present in either B0, B1, or in the multilayer of B2.

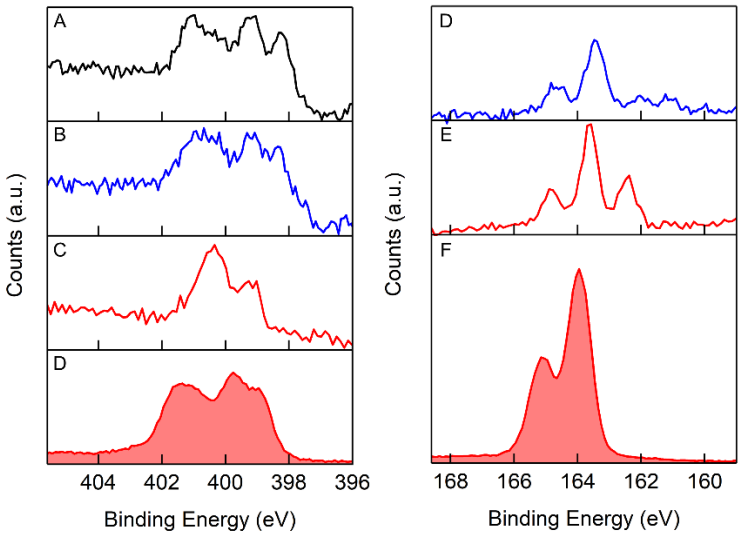

Figure 5.3. (a-d) N 1s XPS of (a) monolayer of B0, (b) monolayer of B1, (c) monolayer of B2, and (d) multilayer of B2. (c-e) S 2p XPS of (c) monolayer of B1, (d) monolayer of B2, and (e) multilayer of B2.

Next, we performed nitrogen 1s (N 1s) NEXAFS, where core electrons are excited to unoccupied orbitals in the molecule and therefore any singly unoccupied molecular orbitals (SUMOs) arising from the radical states can be detected. Figures 5.4a-c show the NEXAFS spectra

of the three radical monolayers. The spectra of B0 and B1 are very similar, with two less-intense absorption features at lower incident photon energy and a more intense absorption at ~400 eV. From our previous density functional theory (DFT) calculations (chapter 4), these peaks arise from core transitions of nitrogen atoms with different initial states to the same final state – the SUMO. Since the SUMO orbital has electron density on all 3 nitrogen atoms (Figure 5.4e), 3 peaks are expected. The absorption energies follow the order of XPS binding energies, where the lowest (highest) energy absorption is due to N4 (N1). The ~400 eV peak has a higher intensity because this absorption feature overlaps with a transition from the core to the lowest unoccupied molecular orbital (LUMO) which occurs slightly lower at ~399.5 eV; the LUMO here refers to the first doubly unoccupied orbital of the radical molecule, which only has electron density on one nitrogen atom (N2, indicated by the blue arrow in Figure 5.3e) and therefore gives rise to a single peak.

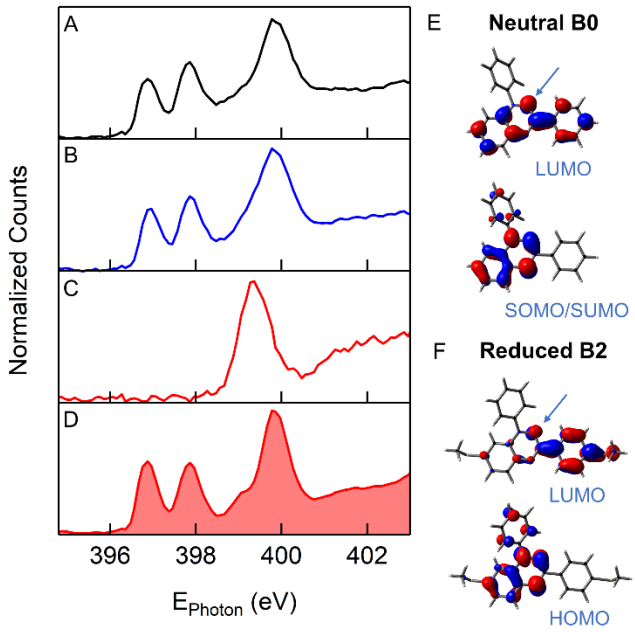

Figure 5.4. N 1s NEXAFS spectra of (a) monolayer of B0, (b) monolayer of B1, (c) monolayer of B2, and (d) multilayer of B2. (e) The orbitals of B0 involved in the NEXAFS transitions. (f) The frontier orbitals of the reduced B2 species. In (e) and (f), the arrows on both LUMOs indicate the only nitrogen atom that has significant orbital density.

The NEXAFS of the monolayer of B2 is different from that of B0 and B1 (Figure 5.4c). Here, there is only a single peak at 399.3 eV. By contrast, the multilayer of B2 is almost the same as the monolayer of B0 and B1 (Figure 5.4d), showing that the radical is intact. NEXAFS therefore agrees with XPS that only the first layer of B2 has an altered electronic structure. We described in chapter 4 that B2 gains an electron from the gold substrate and it SUMO is now filled. Therefore, the remaining peak in its monolayer NEXAFS is the core to LUMO transition. This LUMO is similar to that of the neutral radical and only has electron density on one nitrogen atom (Figure 5.4f). Only molecules in contact with the substrate undergo this electron transfer, and subsequent layers retain the radical character as illustrated in Figure 5.1b. The different behavior of B2 compared to B0 and B1 does not arise from a difference in the orientation of the molecules in the monolayer, since polarization dependent NEXAFS shows that the molecules lie flat on the substrate in all 3 cases (Figure 5.5).

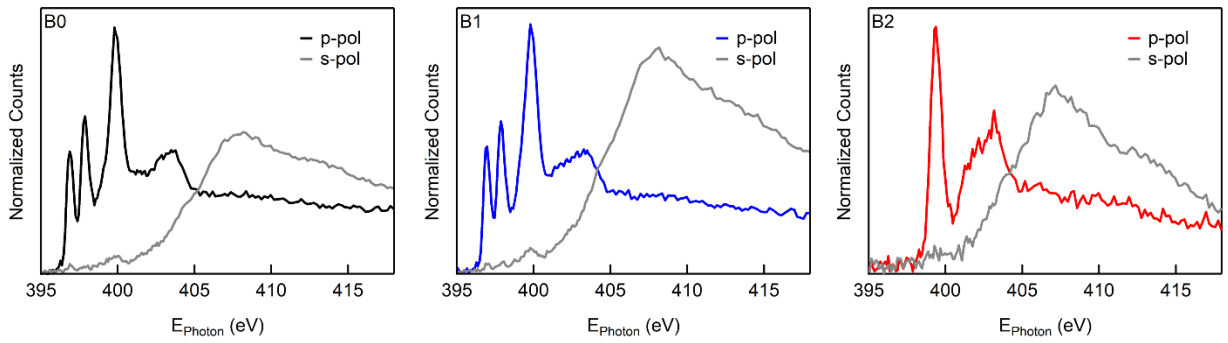

Figure 5.5. Nitrogen K-edge NEXAFS spectra of monolayer films of (a) B0, (b) B1, and (c) B2 taken at p-pol and s-pol. In all 3 films, the core to π^* absorption feature at ~400 eV is strongly quenched, showing that the benzotriazinyl core of the molecules lie flat on the gold surface.

Using XPS and NEXAFS, we have shown that Blatter radicals B0 and B1 are surprisingly stable on gold. They retain their radical character and are only physisorbed onto the substrate. However, the addition of a second thiomethyl group to form B2 appears to introduce an interaction

that mediates an electron transfer event from metal to molecule. Thus, B2 is reduced in the monolayer, although successive layers do not undergo reduction. The location of the thiomethyl group is important too, since B1 shows no charge transfer. While the mechanism of this sulfur-mediated charge transfer needs to be further investigated, our results imply broadly that charge transfer is not only determined by the proximity of the unoccupied orbitals to E_F, but requires some specific interactions at the interface.

5.4 Conclusions

In conclusion, we have studied the interaction of 3 Blatter derivatives on gold. We find that only the derivative with 2 thiomethyl groups, B2, loses its radical character when in contact with the substrate. This derivative undergoes charge transfer from metal to molecule and its SUMO gets filled. The other two radicals studied retain their radical character. Our results show that the Blatter radical may be suitable for spintronic and magnetic applications since it can retain its unpaired electron in films. We also highlight that the same radical core backbone with different functional groups can behave interact differently with the same surface. More generally, we demonstrate that electronically stabilized radicals with large, delocalized half-filled orbitals can still be stable on metal substrates.

5.5 Acknowledgements

The experimental work was supported primarily by the National Science Foundation (award number DMR-1507440). G.L. thanks the Center for Precision Assembly of Superstratic and Superatomic Solids at Columbia University, an NSF MRSEC (award number DMR-1420634) for funding. Gas phase DFT calculations used the Extreme Science and Engineering Discovery Environment (XSEDE) startup allocation TG-DMR150018. XSEDE is supported by NSF grant number ACI-1548562.[19] J.Z.L. thanks the A*STAR Graduate Academy in Singapore for a

graduate fellowship. D.C. and G.K. acknowledge partial financial support from the Slovenian Research Agency (program number P1-0112). G.K. acknowledges financial support from the SIR grant SUNDYN (Nr. RBSI14G7TL, CUP B82I15000910001) of the Italian Ministry of Education, Universities and Research MIUR. We thank Steffen Jockusch for performing EPR spectroscopy and Brandon Fowler for mass spectrometry.

5.6 References

(1) Hwang, J.; Wan, A.; Kahn, A. *Mater. Sci. Eng., R* **2009**, *64*, 1-31.

(2) Wilcox, D. A.; Agarkar, V.; Mukherjee, S.; Boudouris, B. W. *Annu. Rev. Chem. Biomol. Eng.* **2018**, *9*, 83-103.

(3) Tomlinson, E. P.; Hay, M. E.; Boudouris, B. W. *Macromolecules* **2014**, *47*, 6145-6158.

(4) Oyaizu, K.; Nishide, H. *Adv. Mater.* **2009**, *21*, 2339-2344.

(5) Szulczewski, G.; Sanvito, S.; Coey, M. *Nat. Mater.* **2009**, *8*, 693.

(6) Sanvito, S. *Chem. Soc. Rev.* **2011**, *40*, 3336-3355.

(7) Mugnaini, V.; Calzolari, A.; Ovsyannikov, R.; Vollmer, A.; Gonidec, M.; Alcon, I.; Veciana, J.; Pedio, M. *J. Phys. Chem. Lett.* **2015**, *6*, 2101-2106.

(8) Savu, S.-A.; Biswas, I.; Sorace, L.; Mannini, M.; Rovai, D.; Caneschi, A.; Chassé, T.; Casu, M. B. *Chem. - Eur. J.* **2013**, *19*, 3445-3450.

(9) Kakavandi, R.; Savu, S.-A.; Sorace, L.; Rovai, D.; Mannini, M.; Casu, M. B. *J. Phys. Chem. C* **2014**, *118*, 8044-8049.

(10) Kakavandi, R.; Savu, S.-A.; Caneschi, A.; Casu, M. B. *J. Phys. Chem. C* **2013**, *117*, 26675-26679.

(11) Arantes, C.; Chernick, E. T.; Gruber, M.; Rocco, M. L. M.; Chassé, T.; Tykwinski, R. R.; Casu, M. B. *J. Phys. Chem. C* **2016**, *120*, 3289-3294.

(12) Grillo, F.; Fruchtl, H.; Francis, S. M.; Mugnaini, V.; Oliveros, M.; Veciana, J.; Richardson, N. V. *Nanoscale* **2012**, *4*, 6718-6721.

(13) Zhang, Y.-h.; Kahle, S.; Herden, T.; Stroh, C.; Mayor, M.; Schlickum, U.; Ternes, M.; Wahl, P.; Kern, K. *Nat. Commun.* **2013**, *4*, 2110.

(14) Müllegger, S.; Rashidi, M.; Fattinger, M.; Koch, R. *J. Phys. Chem. C* **2013**, *117*, 5718-5721.

(15) Liu, J.; Isshiki, H.; Katoh, K.; Morita, T.; Breedlove, B. K.; Yamashita, M.; Komeda, T. *J. Am. Chem. Soc.* **2013**, *135*, 651-658.

(16) Blatter, H. M.; Lukaszewski, H. *Tetrahedron Lett.* **1968**, *9*, 2701-2705.

(17) Ciccullo, F.; Gallagher, N. M.; Geladari, O.; Chassé, T.; Rajca, A.; Casu, M. B. *ACS Appl. Mater. Interfaces* **2016**, *8*, 1805-1812.

(18) Koutentis, P. A.; Lo Re, D. *Synthesis* **2010**, *12*, 2075-2079.

(19) Towns, J.; Cockerill, T.; Dahan, M.; Foster, I.; Gaither, K.; Grimshaw, A.; Hazlewood, V.; Lathrop, S.; Lifka, D.; Peterson, G. D.; Roskies, R.; Scott, J. R.; Wilkins-Diehr, N. *Comput. Sci. Eng.* **2014**, *16*, 62-74.

6. Conclusions and Outlook

6.1 Summary

Through this work, we have explored different ways to tune single molecule conductance by exploiting the electronic properties of different classes of molecules. We have described how conducting orbitals can be predictably tuned between the highest occupied molecular orbital (HOMO) and lowest unoccupied molecular orbital (LUMO), showed that molecules with conducting orbitals close to the Fermi energy of gold can display an increase of conductance with length, and investigated the interface between the half-occupied frontier orbitals of organic radicals and metal electrodes. Through our investigations, we established structure-property relationships that can guide the design and synthesis of future materials for the various applications described.

We first introduced the scanning tunneling microscope break junction (STM-BJ) method used herein to measure the conductance of single molecules. An overview of the method was provided, showing how statistically significant conductance values are obtained. Next, we described how the electronic structure of the molecules gives rise to a transmission function, which in turn determines the nature of the conducting orbitals and the magnitude of conductance.

We then showed that adding very strong electron-withdrawing groups onto a thiophene backbone can induce LUMO conducting behavior since the LUMO shifts closer to gold. A combination of thiophene dioxides and thienopyrrolodiones was used to create a suite of molecules with varying electron affinities. As more electron-withdrawing groups were added to the backbone, a transition from HOMO, to mid-gap, to LUMO conduction was observed.

We also presented work on bis(triarylamines), discovering that they can be switched to a high conducting state via chemical oxidation. These high conducting states have mixed-valence

character and surprisingly become more conducting as the molecular length increases. Typically, the opposite length dependence is observed: indeed, the neutral molecules show an expected decrease in conductance as they get longer.

Finally, we found that the presence of half-filled orbitals near the Fermi energy of gold can make molecules behave very differently when there are slight changes to the surroundings. When the 1,2,4-benzotriazinyl Blatter radical was measured in the STM-BJ in solution, only the conductance signature of the oxidized species was recorded. Conversely, this molecule deposited on a gold substrate in ultra-high vacuum undergoes charge transfer from metal to molecule and gets reduced. Further investigation revealed that gold binding thiomethyl groups mediate this charge transfer event, but only when attached to specific sites on the molecule.

6.2 Future Work

Since the studies described here investigate aspects of molecular conductance using motifs and materials that have hitherto been underexplored, there is much room to expand the scope of investigations. As mentioned in the introduction, one vision for the field is to be able to predict conductance behavior of a given structure, or similarly be able to design a molecule for a specific purpose in a molecular circuit. Within that framework, identifying *classes* of materials to suit a specific purpose is an important first step.

The investigation of the conductance of thiophene dioxides in this thesis is part of a larger body of work that has explored thiophenes and thiophene dioxides in a variety of single molecule conductance experiments. One underlying motivation for these experiments is that the conductance behavior of these oligomeric materials can be used to predict how they will perform when incorporated into semiconducting polymers for organic electronics. Thus far, we have established that thiophene dioxides can potentially be used as electron acceptors or n-type

materials, which are rare among organic systems. However, devices made from thiophene dioxide-based materials still face challenges like low solubility and poor morphology. These challenges could potentially be overcome by the oxidized thienopyrrolodione moiety introduced in this work, which has yet to be incorporated into donor-acceptor type semiconducting polymers. Since it is a stronger electron withdrawing moiety than thiophene dioxide, stoichiometrically smaller amounts of it need to be added into a material to induce n-type behavior, potentially alleviating poor solubility brought on by the rigidity of multiple adjacent thiophene dioxide units. Within the molecular conductance field, thiophene dioxides also present a good opportunity to study near- or at- resonant transport if a molecule with a LUMO very close to the Fermi energy of gold can be synthesized.

Mixed-valence systems such as the bis(triarylamines) require theoretical investigations to describe their highly conducting nature so that it can be replicated in other systems. It has also yet to be established whether other mixed-valence compounds – organic and inorganic alike – also show similar desirable long-range transport properties. Additionally, methods to generate and measure the conductance of the dication states of the bis(triarylamines) have to be developed in order to compare the behavior with the neutral and cation states. The dications are potentially interesting because of the length dependence of their diradical character; this might give rise to new conducting phenomena.

In general, we have mentioned throughout this thesis that organic radicals have huge potential for magnetic and spintronic applications. Thus, more varieties of radicals should be synthesized and tested. Even within the family of Blatter radicals we studied here, one can design a derivative that does not get oxidized in the molecular junction to investigate transport through a half-occupied orbital. Techniques to measure spin-dependent transport and magnetoresistance

currently exist but must also be developed further to make these more accessible and reliable so that the scope of materials studied can be expanded.

6.3 Concluding remarks

The field of molecular electronics is highly interdisciplinary and requires heavy collaboration between engineers to design and build equipment, physicists to develop theory and perform experiments, and chemists to design and synthesize molecules. Breakthroughs in this field will no doubt require a combination of cutting edge measurement techniques, robust theoretical models, and a colorful variety of molecules to study. This thesis seeks to inspire other chemists to imagine how molecules that have other applications in chemistry will behave in molecular junctions and to team up with others to investigate them.

7. NMR Spectra of reported compounds

7.1 Compounds in Chapter 2

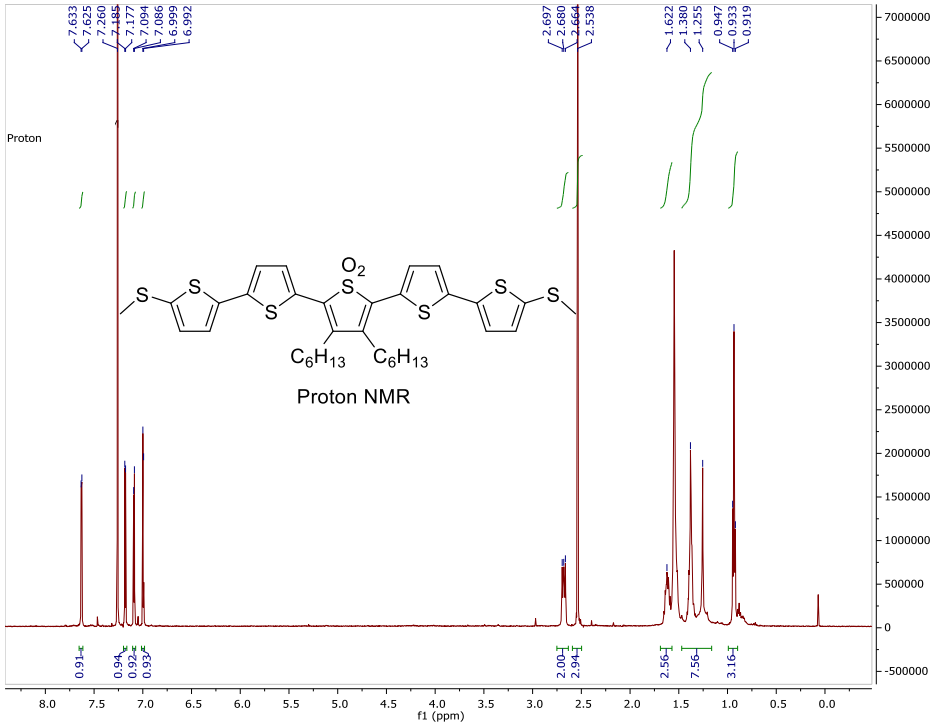

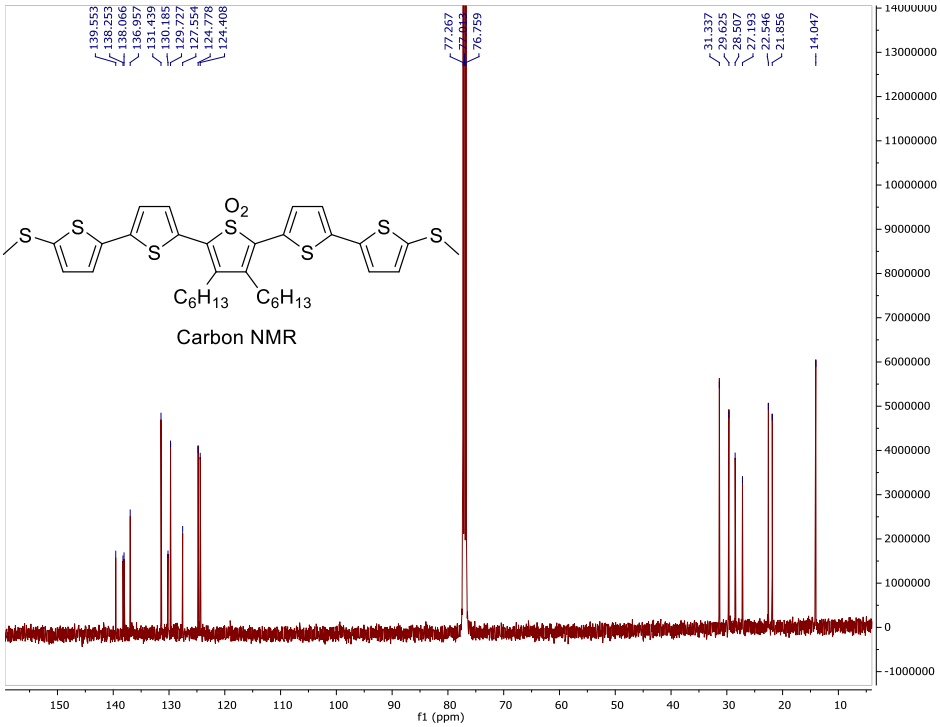

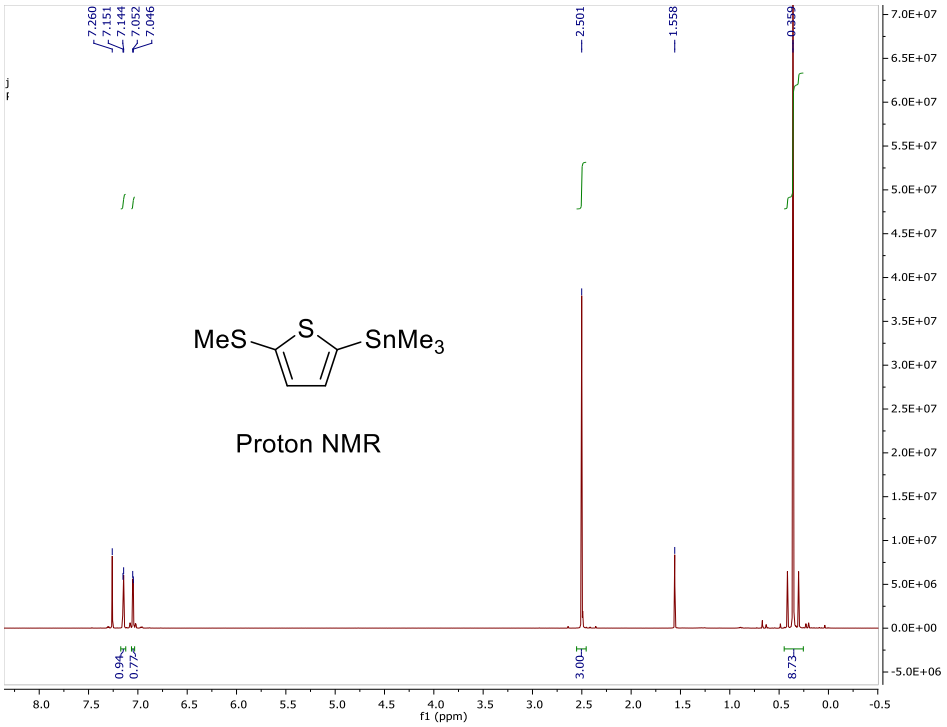
7.260
7.151
7.144
7.052
7.046
2.501
1.558
0.359
MeS
S
SnMe3
Proton NMR
0.94
0.77
3.00
8.73
f1 (ppm)

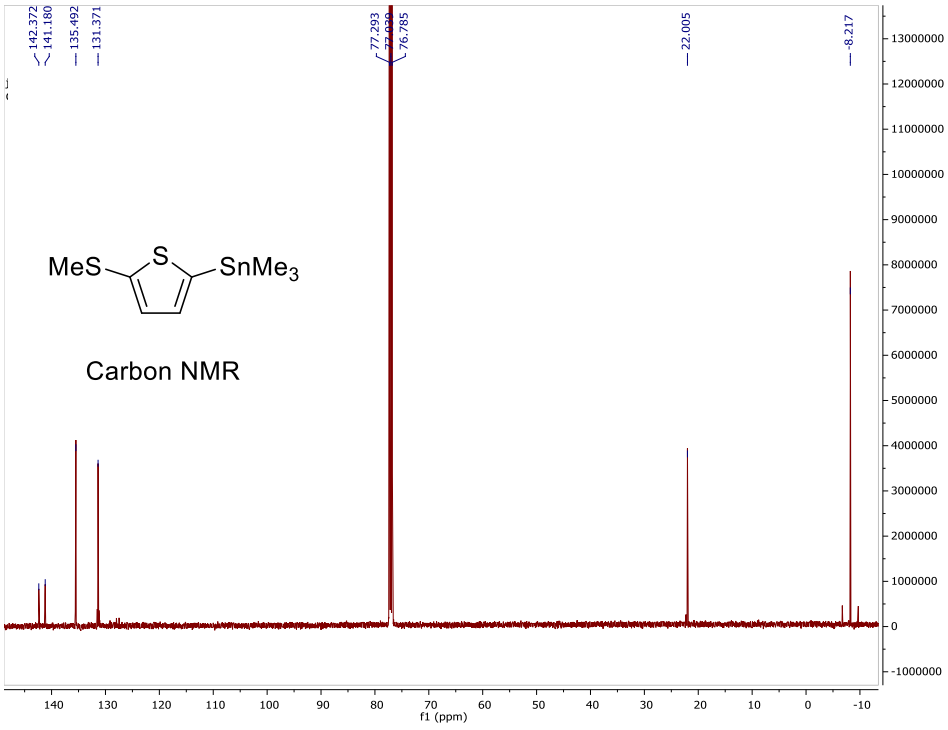
142.372
141.180
135.492
131.371
77.293
77.038
76.785
22.005
-8.217
MeS
S
SnMe3
Carbon NMR
f1 (ppm)

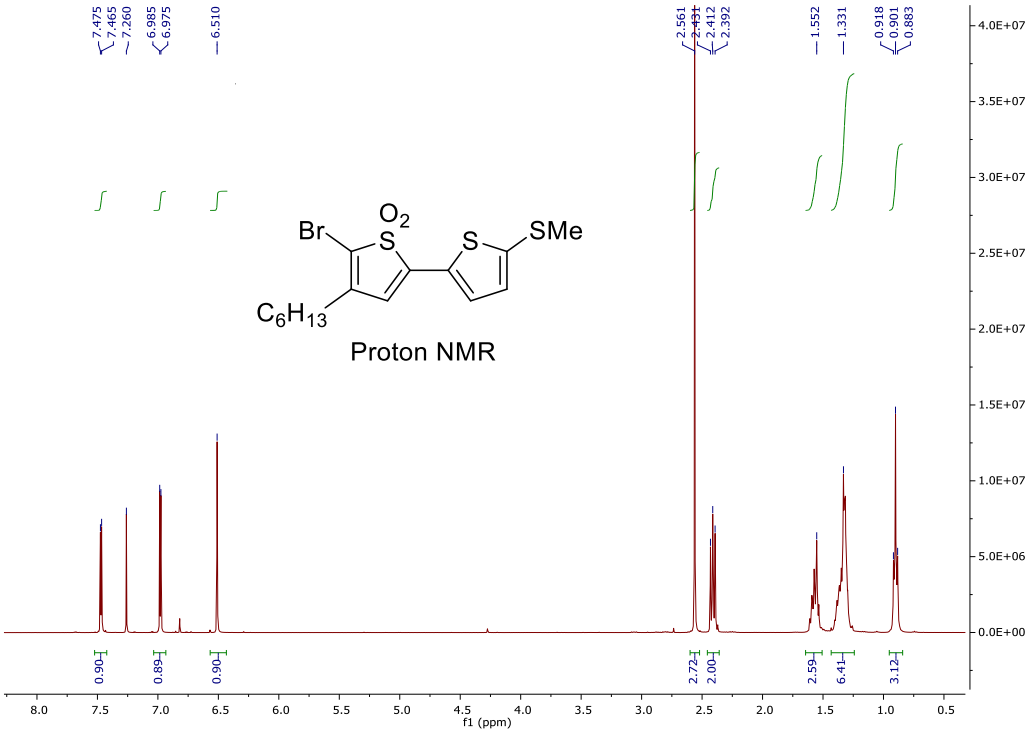
7.475
7.465
7.260
6.985
6.975
6.510
2.561
2.431
2.412
2.392
1.552
1.331
0.918
0.901
0.883
Br
O2
S
S
SMe
C6H13
Proton NMR
0.90
0.89
0.90
2.72
2.00
2.59
6.41
3.12
f1 (ppm)

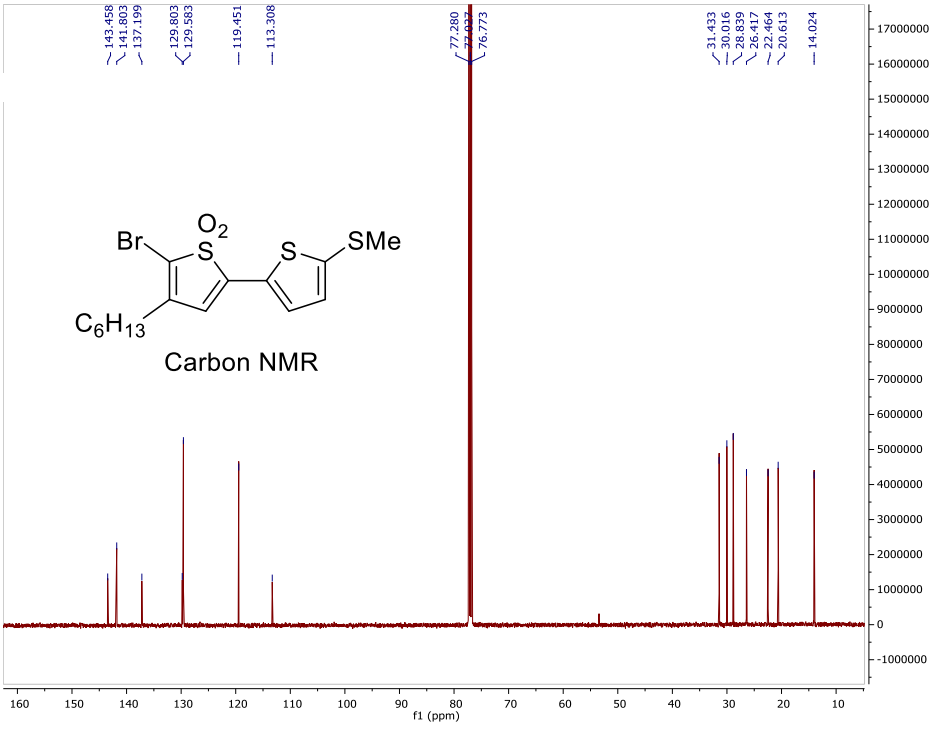
143.458
141.803
137.199
129.803
129.583
119.451
113.308
77.280
77.032
76.773
31.433
30.016
28.839
26.417
22.464
20.613
14.024
Br
O2
S
S
SMe
C6H13
Carbon NMR
f1 (ppm)

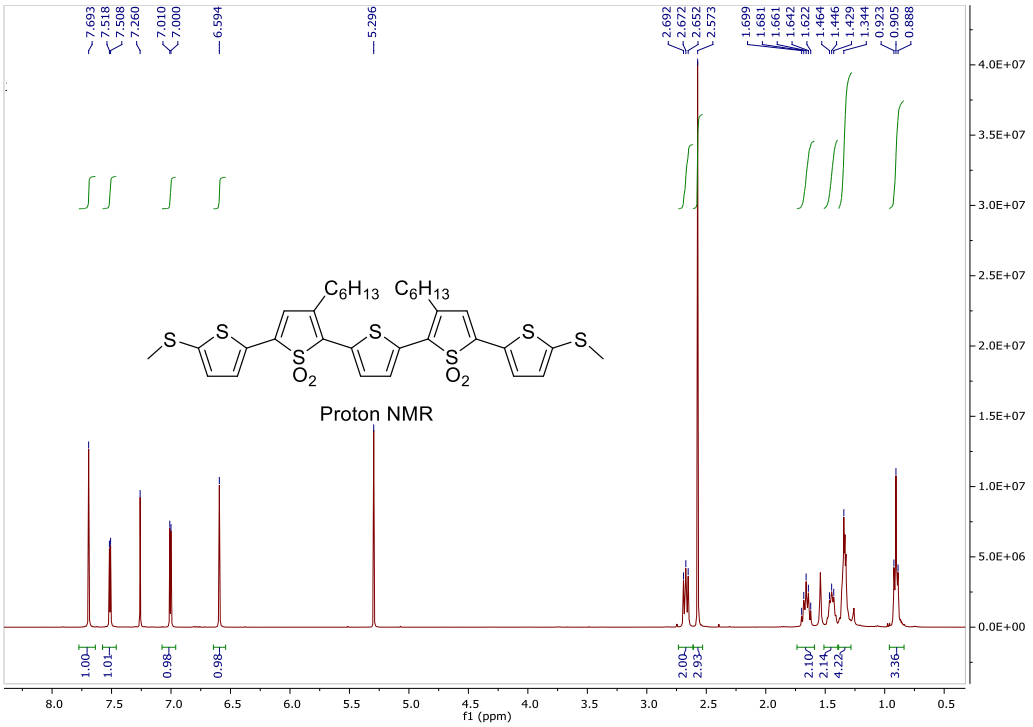
7.693
7.518
7.508
7.260
7.010
7.000
6.594
5.296
2.692
2.672
2.652
2.573
1.699
1.681
1.661
1.642
1.622
1.464
1.446
1.429
1.344
0.923
0.905
0.888
Proton NMR
1.00
1.01
0.98
0.98
2.00
2.93
2.10
2.14
4.22
3.36
f1 (ppm)

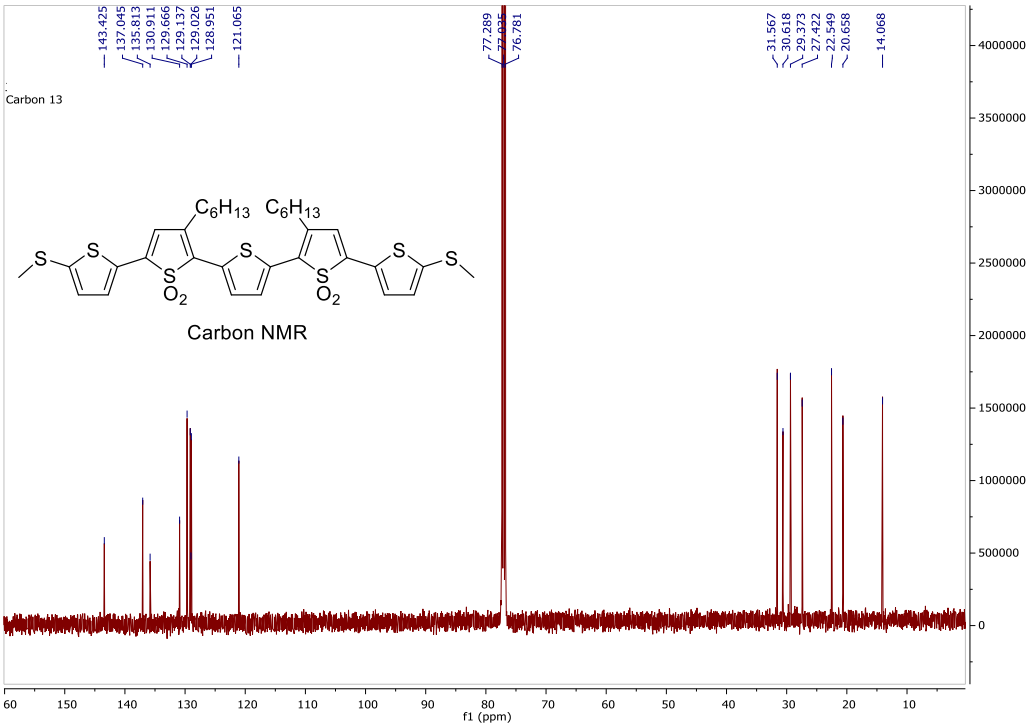
143.425
137.045
135.813
130.911
129.666
129.137
129.026
128.951
121.065
77.289
77.081
76.781
31.567
30.618
29.373
27.422
22.549
20.658
14.068
Carbon 13
Carbon NMR
f1 (ppm)

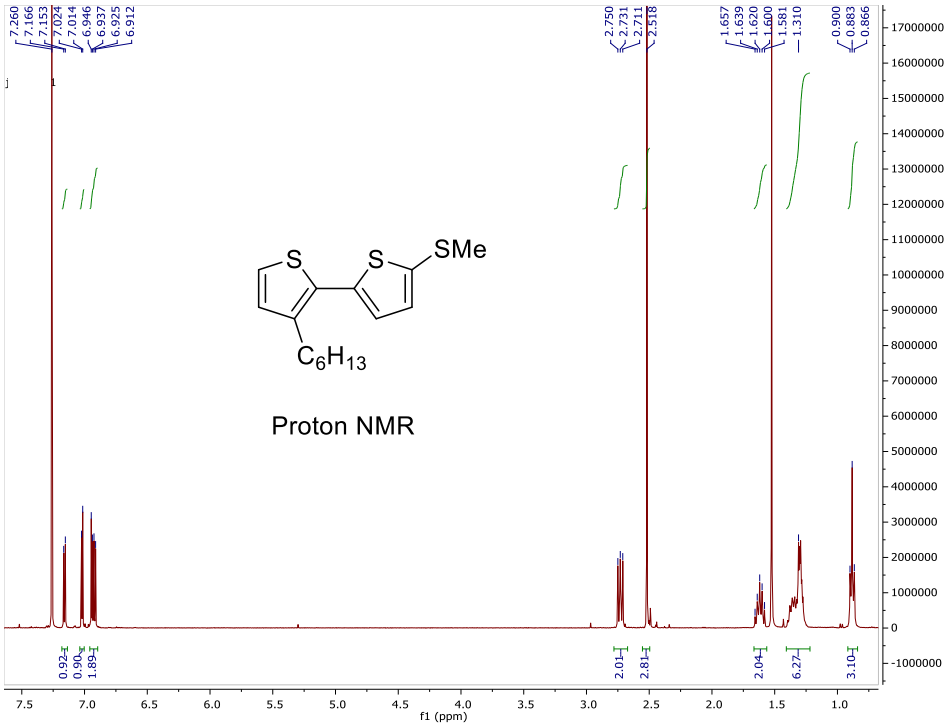
7.260
7.166
7.153
7.024
7.014
6.946
6.937
6.925
6.912
2.750
2.731
2.711
2.518
1.657
1.639
1.620
1.600
1.581
1.310
0.900
0.883
0.866
SMe
S
S
C6H13
Proton NMR
0.92
0.90
1.89
2.01
2.81
2.04
6.27
3.10
f1 (ppm)

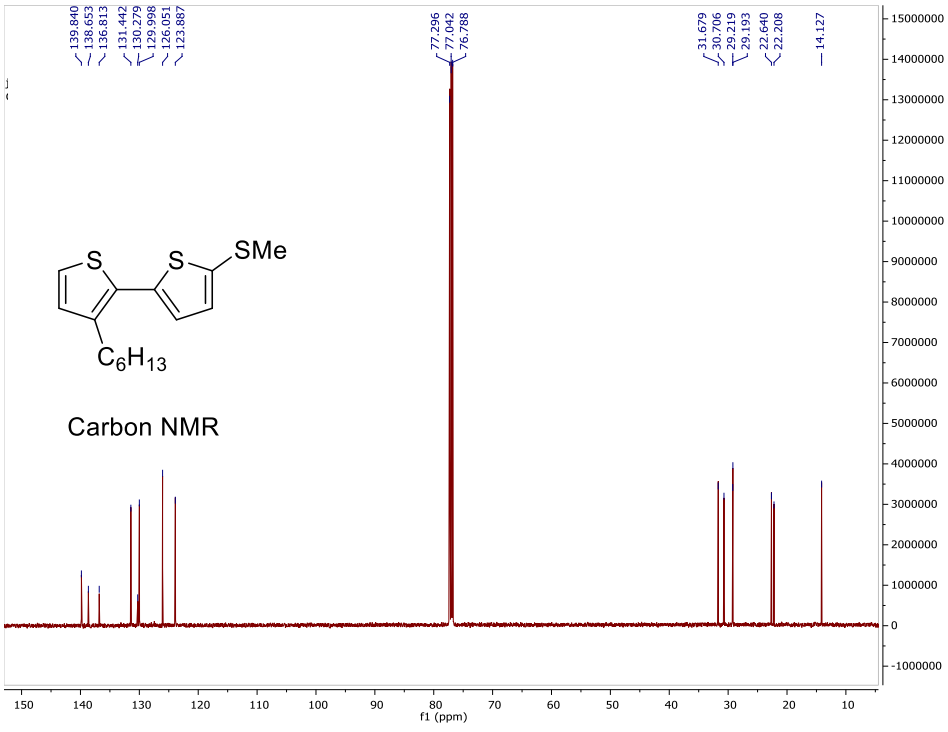
139.840
138.653
136.813
131.442
130.279
129.998
126.051
123.887
77.296
77.042
76.788
31.679
30.706
29.219
29.193
22.640
22.208
14.127
SMe
S
S
C6H13
Carbon NMR
f1 (ppm)

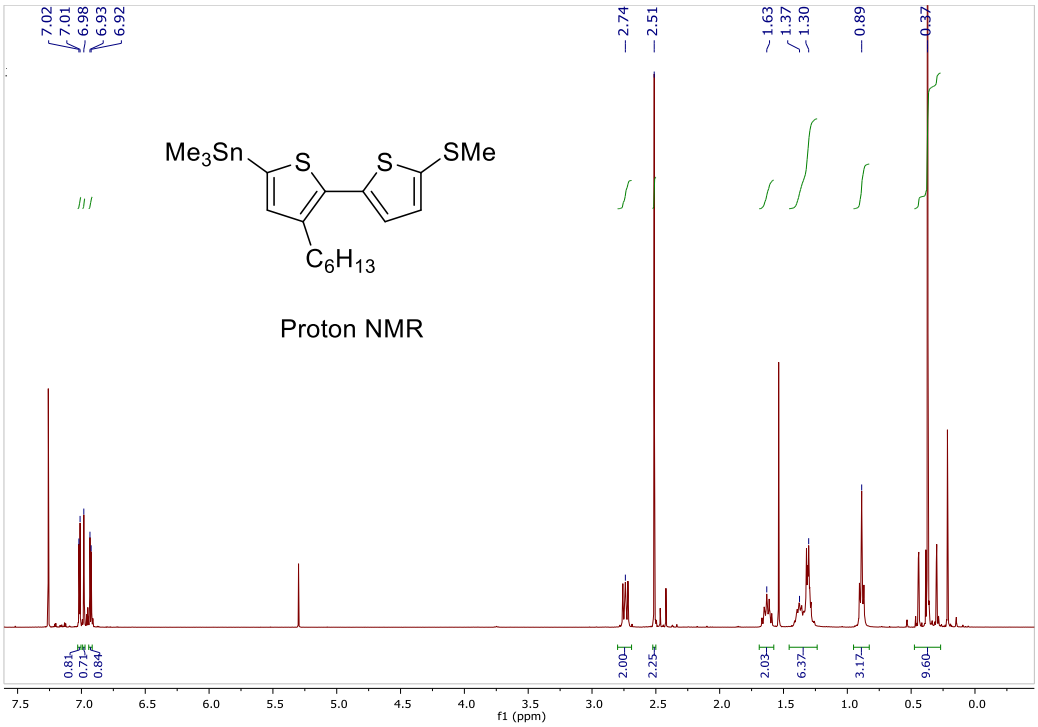
7.02
7.01
6.98
6.93
6.92
2.74
2.51
1.63
1.37
1.30
0.89
0.37
Me3Sn
S
S
SMe
C6H13
Proton NMR
0.81
0.71
0.84
2.00
2.25
2.03
6.37
3.17
9.60
f1 (ppm)

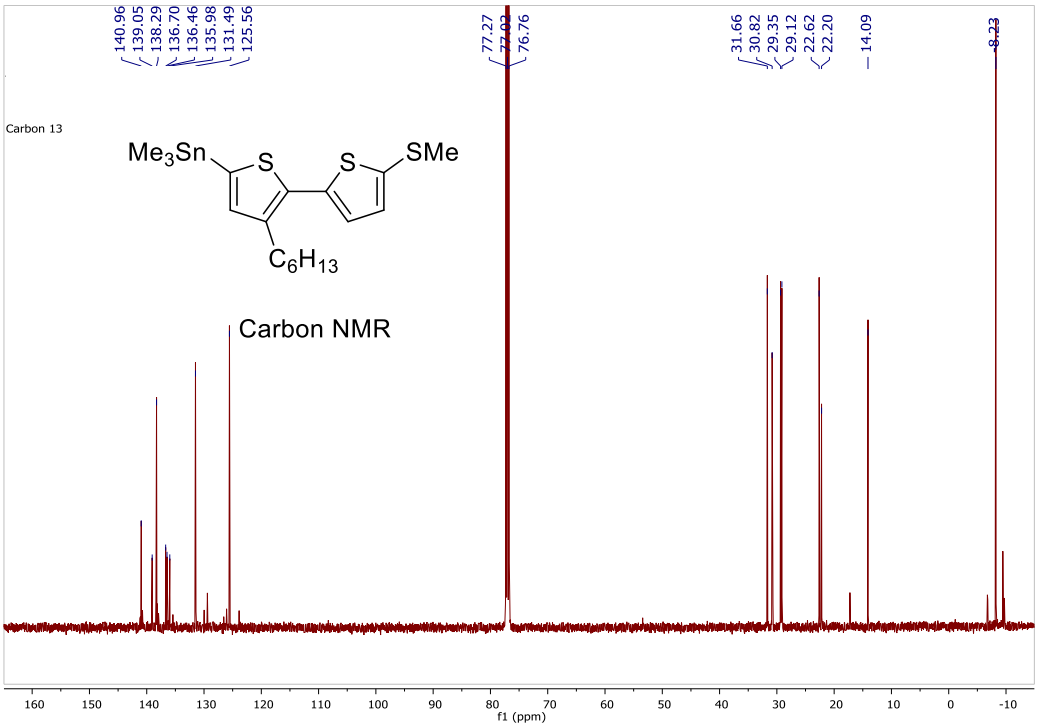
140.96
139.05
138.29
136.70
136.46
135.98
131.49
125.56
77.27
77.01
76.76
31.66
30.82
29.35
29.12
22.62
22.20
14.09
8.23
Carbon 13
Me3Sn
S
S
SMe
C6H13
Carbon NMR
f1 (ppm)

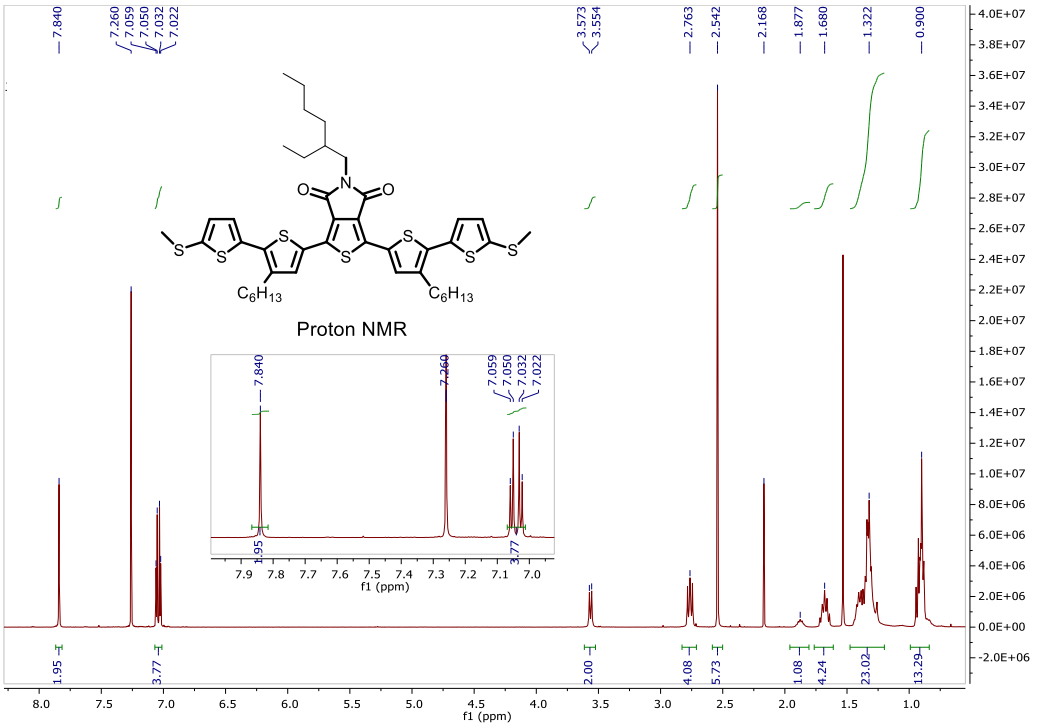
7.840
7.260
7.059
7.050
7.032
7.022
3.573
3.554
2.763
2.542
2.168
1.877
1.680
1.322
0.900
Proton NMR
f1 (ppm)

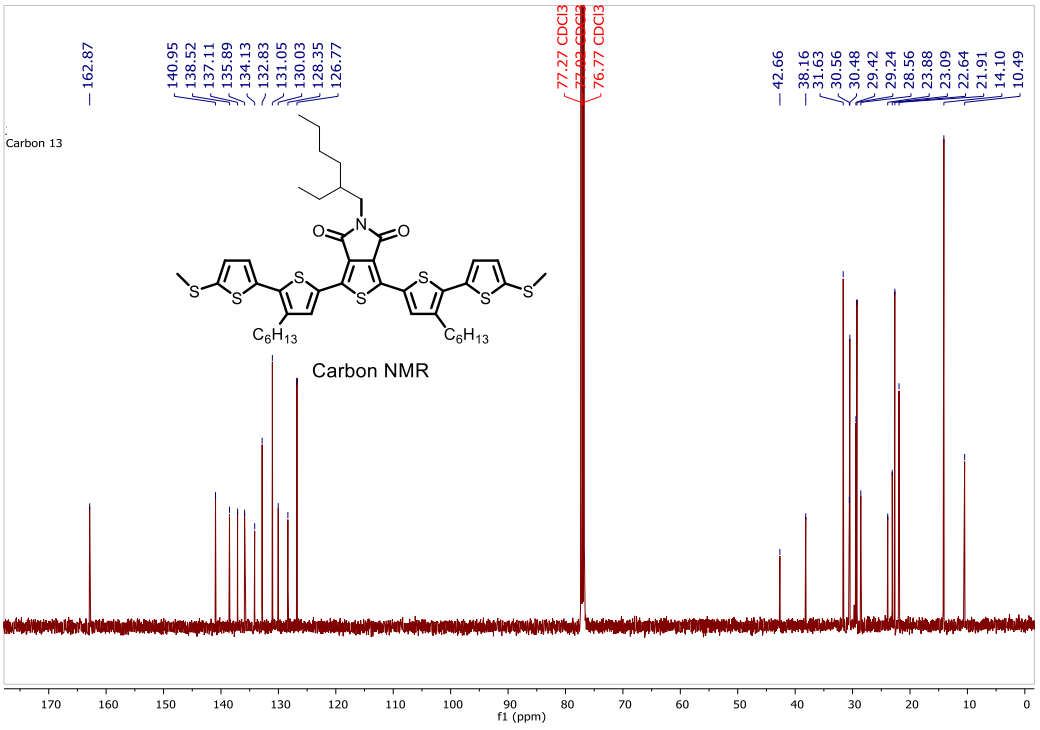
162.87
140.95
138.52
137.11
135.89
134.13
132.83
131.05
130.03
128.35
126.77
77.27 CDCl3
77.03 CDCl3
76.77 CDCl3
42.66
38.16
31.63
30.56
30.48
29.42
29.24
28.56
23.88
23.09
22.64
21.91
14.10
10.49
Carbon 13
Carbon NMR
f1 (ppm)

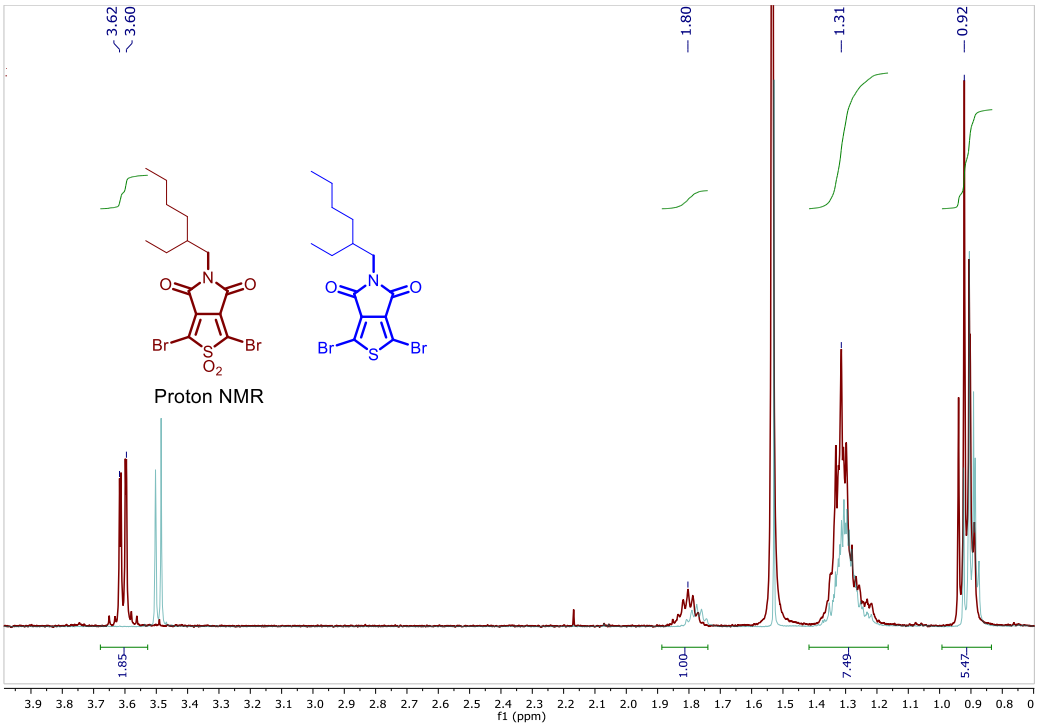
3.62
3.60
1.80
1.31
0.92
Proton NMR
1.85
1.00
7.49
5.47
f1 (ppm)

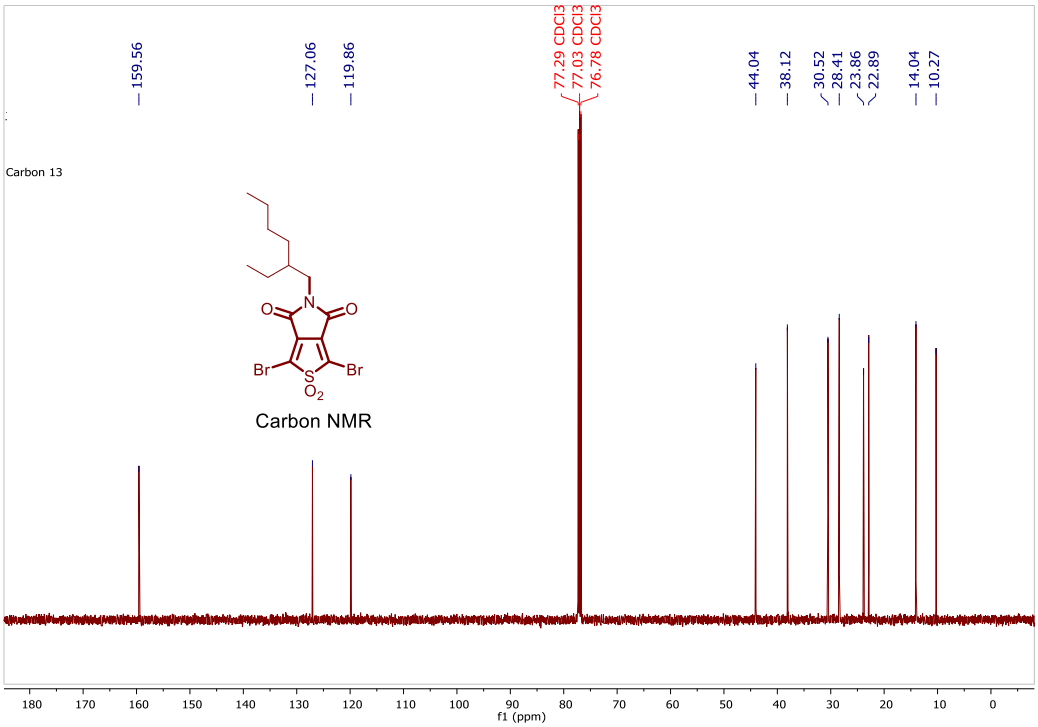
159.56
127.06
119.86
77.29 CDCl3
77.03 CDCl3
76.78 CDCl3
44.04
38.12
30.52
28.41
23.86
22.89
14.04
10.27
Carbon 13
Carbon NMR
f1 (ppm)

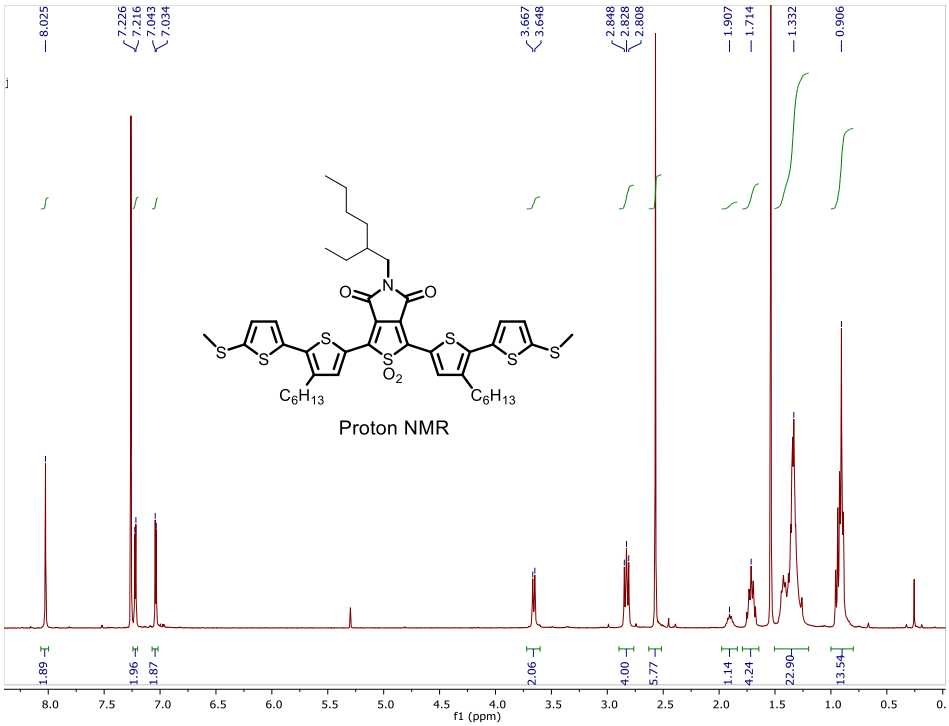
8.025
7.226
7.216
7.043
7.034
3.667
3.648
2.848
2.828
2.808
1.907
1.714
1.332
0.906
1.89
1.96
1.87
2.06
4.00
5.77
1.14
4.24
22.90
13.54
f1 (ppm)
Proton NMR

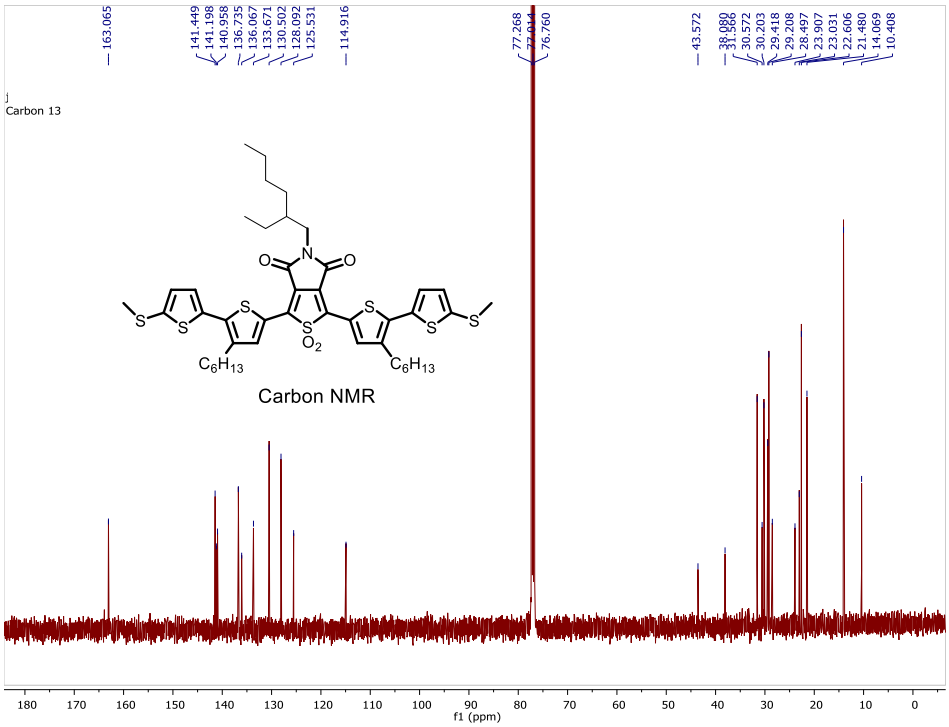
Carbon 13
163.065
141.449
141.198
140.958
136.735
136.067
133.671
130.502
128.092
125.531
114.916
77.268
77.014
76.760
43.572
38.080
31.980
30.572
30.203
29.418
29.208
28.497
23.907
23.031
22.606
21.480
14.069
10.408
f1 (ppm)
Carbon NMR

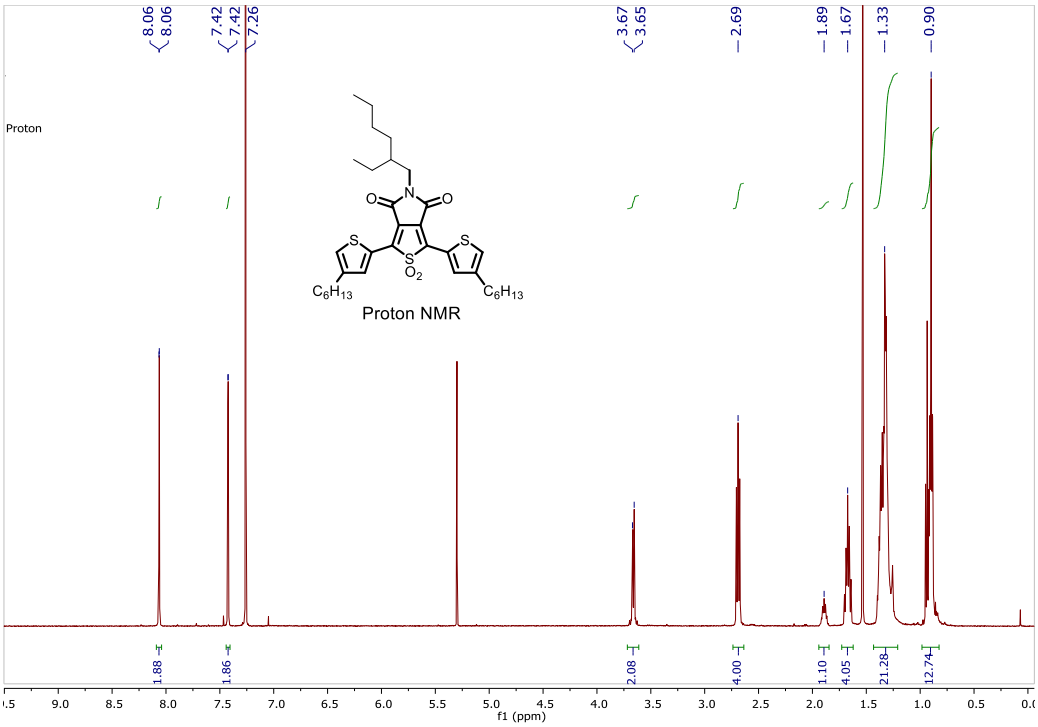
Proton
8.06
8.06
7.42
7.42
7.26
3.67
3.65
2.69
1.89
1.67
1.33
0.90
1.88
1.86
2.08
4.00
1.10
4.05
21.28
12.74
f1 (ppm)
Proton NMR

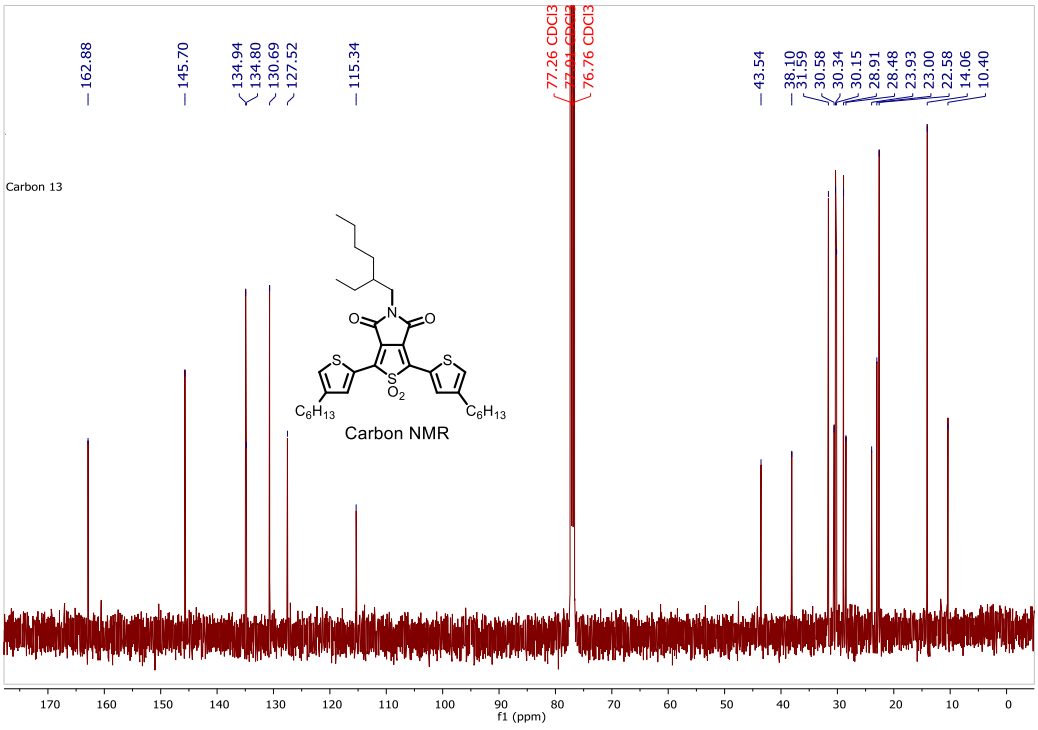
Carbon 13
162.88
145.70
134.94
134.80
130.69
127.52
115.34
77.26 CDCl3
77.01 CDCl3
76.76 CDCl3
43.54
38.10
31.59
30.58
30.34
30.15
28.91
28.48
23.93
23.00
22.58
14.06
10.40
f1 (ppm)
Carbon NMR

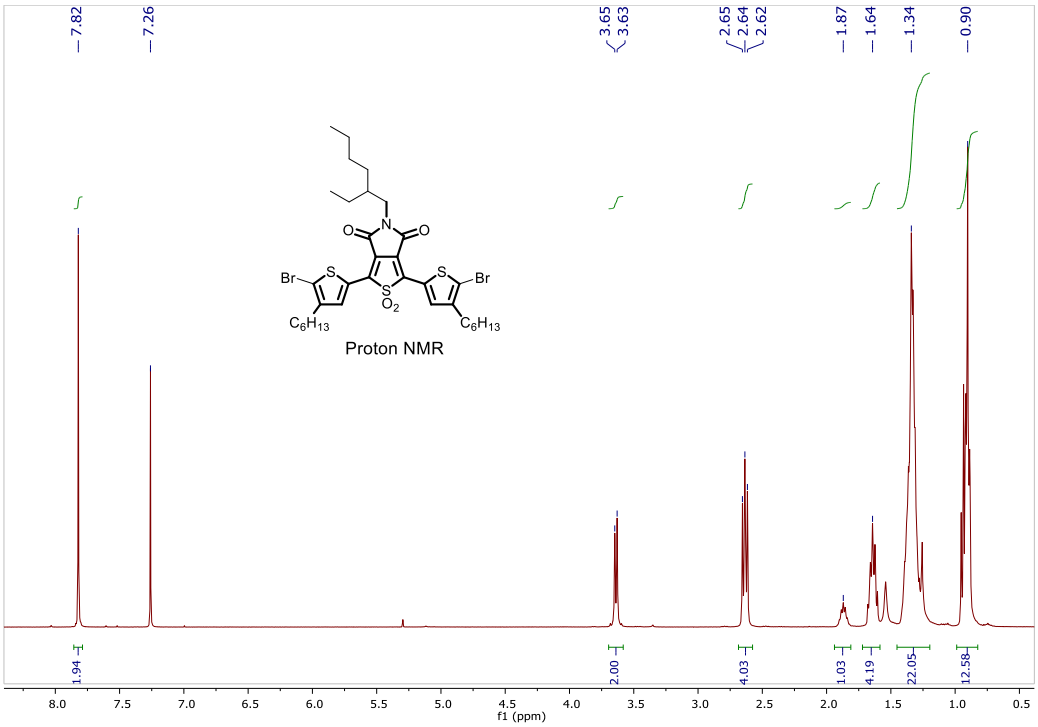
7.82
7.26
3.65
3.63
2.65
2.64
2.62
1.87
1.64
1.34
0.90
Br
Br
C_6H_{13}
C_6H_{13}
Proton NMR
1.94
2.00
4.03
1.03
4.19
22.05
12.58
f1 (ppm)

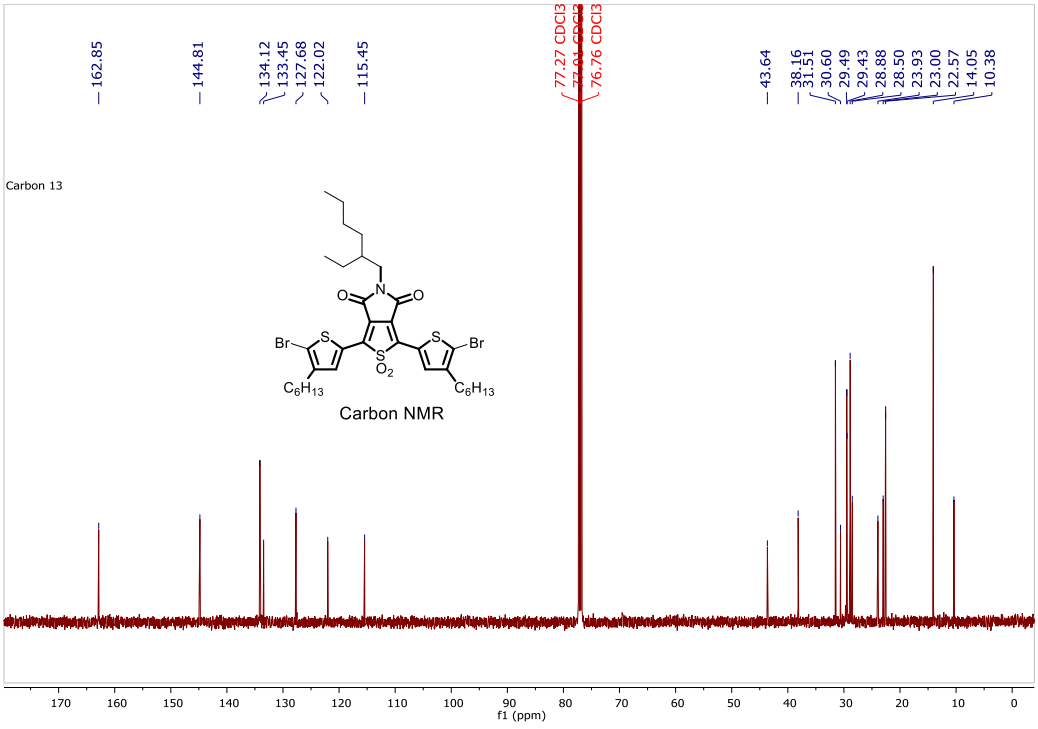
Carbon 13
162.85
144.81
134.12
133.45
127.68
122.02
115.45
77.27 CDCl3
77.01 CDCl3
76.76 CDCl3
43.64
38.16
31.51
30.60
29.49
29.43
28.88
28.50
23.93
23.00
22.57
14.05
10.38
Br
Br
C_6H_{13}
C_6H_{13}
Carbon NMR
f1 (ppm)

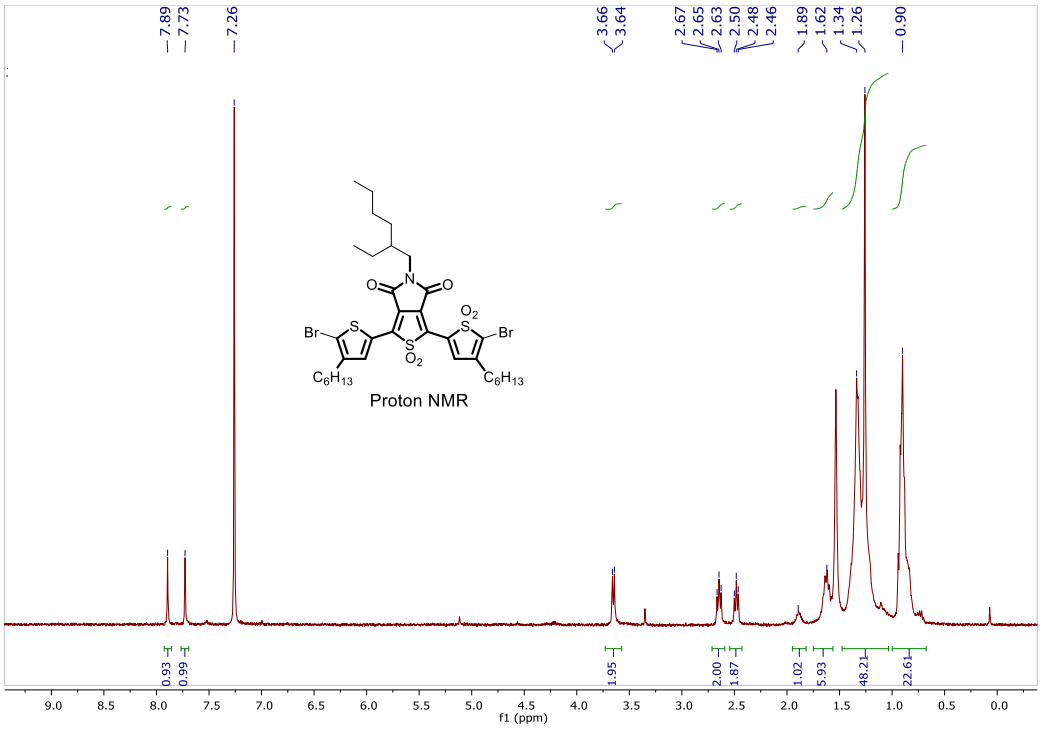
7.89
7.73
7.26
3.66
3.64
2.67
2.65
2.63
2.50
2.48
2.46
1.89
1.62
1.34
1.26
0.90
Proton NMR
0.93
0.99
1.95
2.00
1.87
1.02
5.93
48.21
22.61
f1 (ppm)

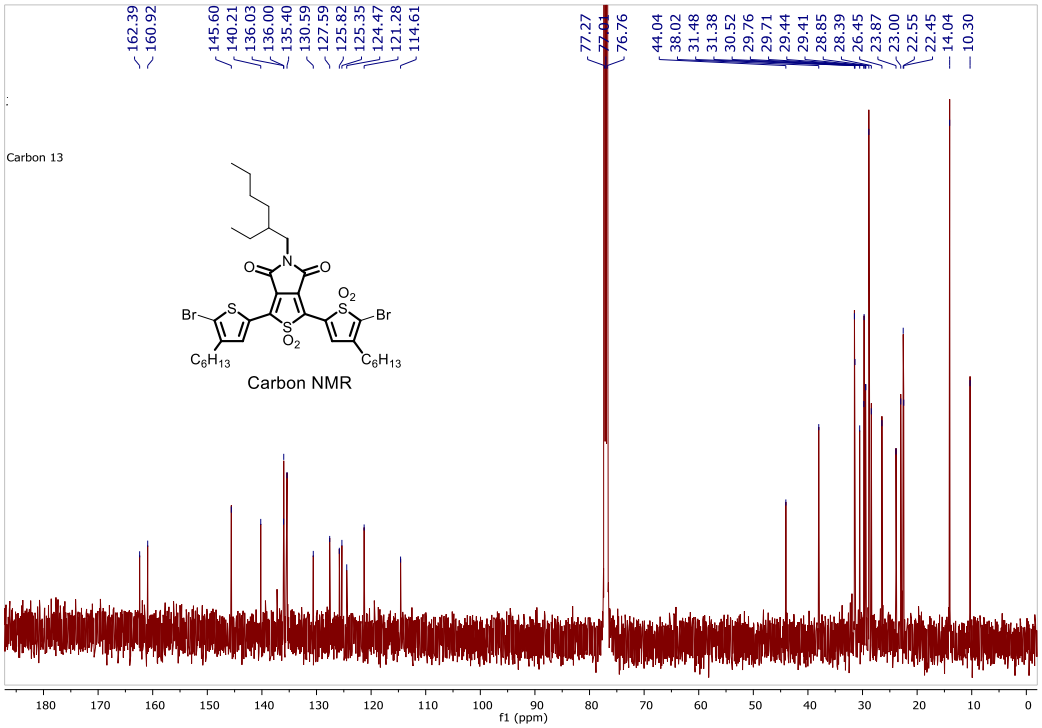
Carbon 13
162.39
160.92
145.60
140.21
136.03
136.00
135.40
130.59
127.59
125.82
125.35
124.47
121.28
114.61
77.27
77.01
76.76
44.04
38.02
31.48
31.38
30.52
29.76
29.71
29.44
29.41
28.85
28.39
26.45
23.87
23.00
22.55
22.45
14.04
10.30
Carbon NMR
f1 (ppm)

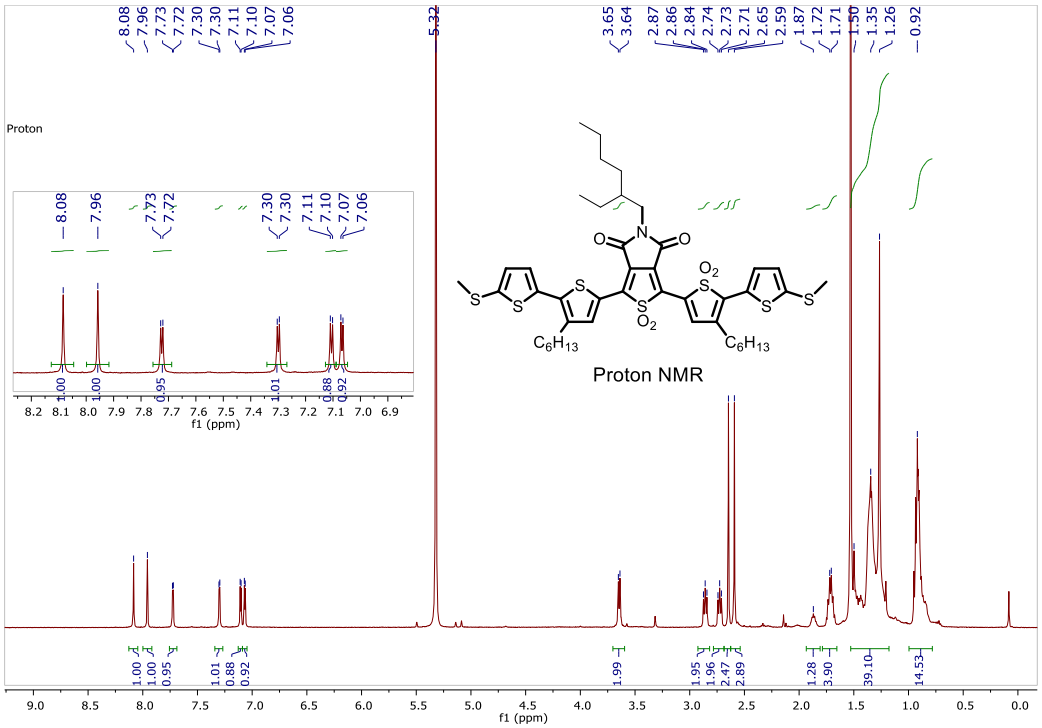
Proton
Proton NMR
f1 (ppm)

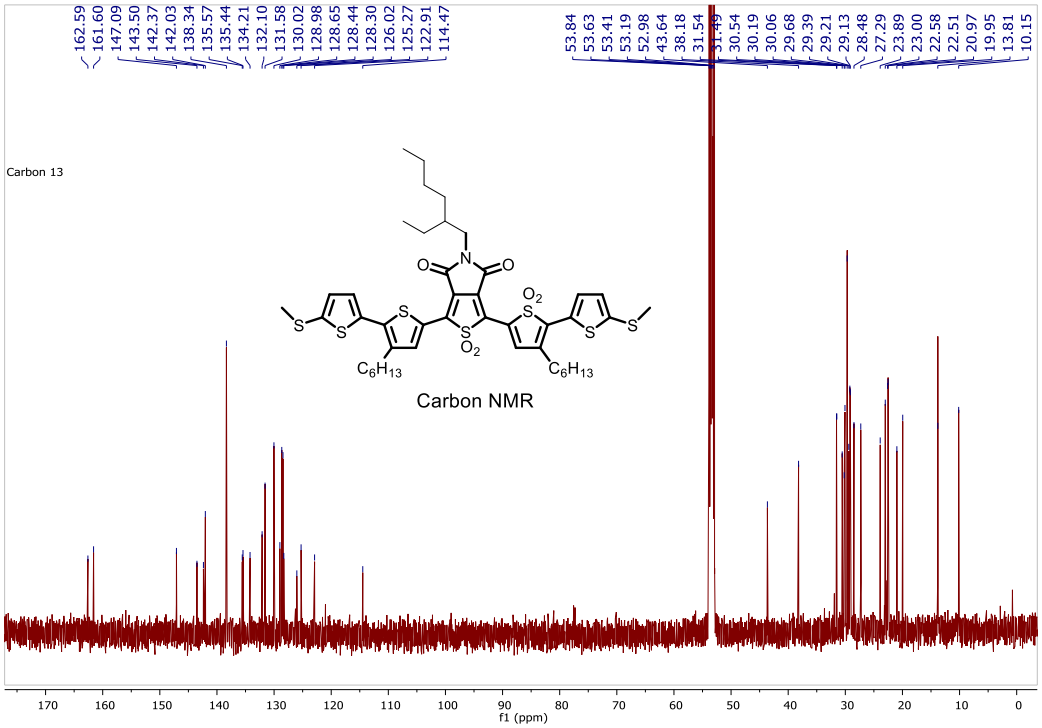
Carbon 13
Carbon NMR
f1 (ppm)

7.2 Compounds in Chapter 3

^{1}H-NMR of **B1** (400 MHz, Acetone-d6, 25ºC)

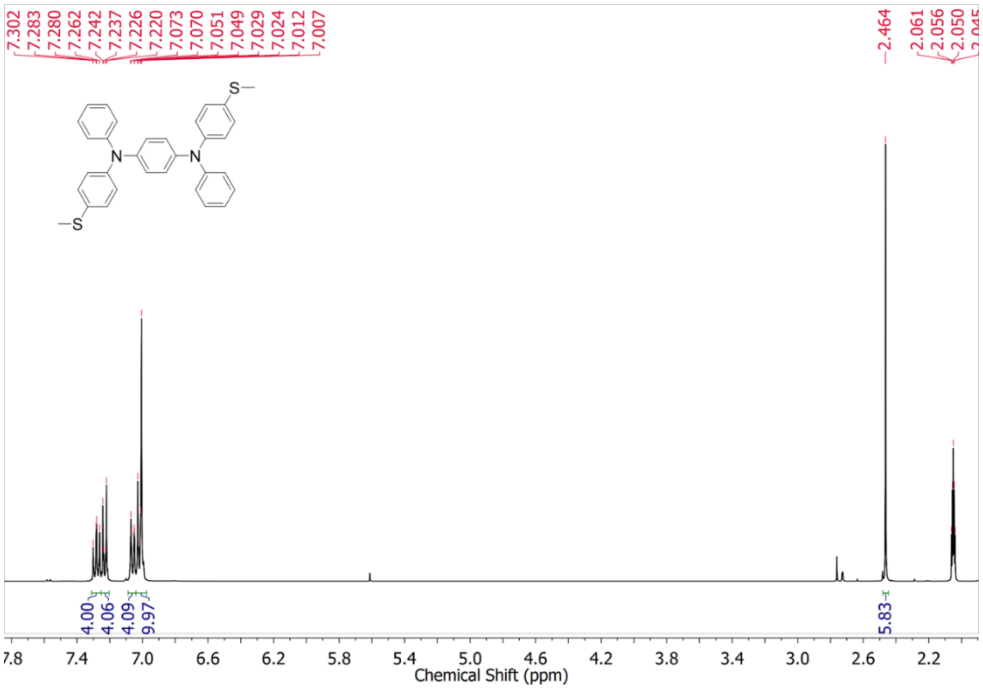

^{13}C-NMR of **B1** (125 MHz, Acetone-d6, 25ºC)

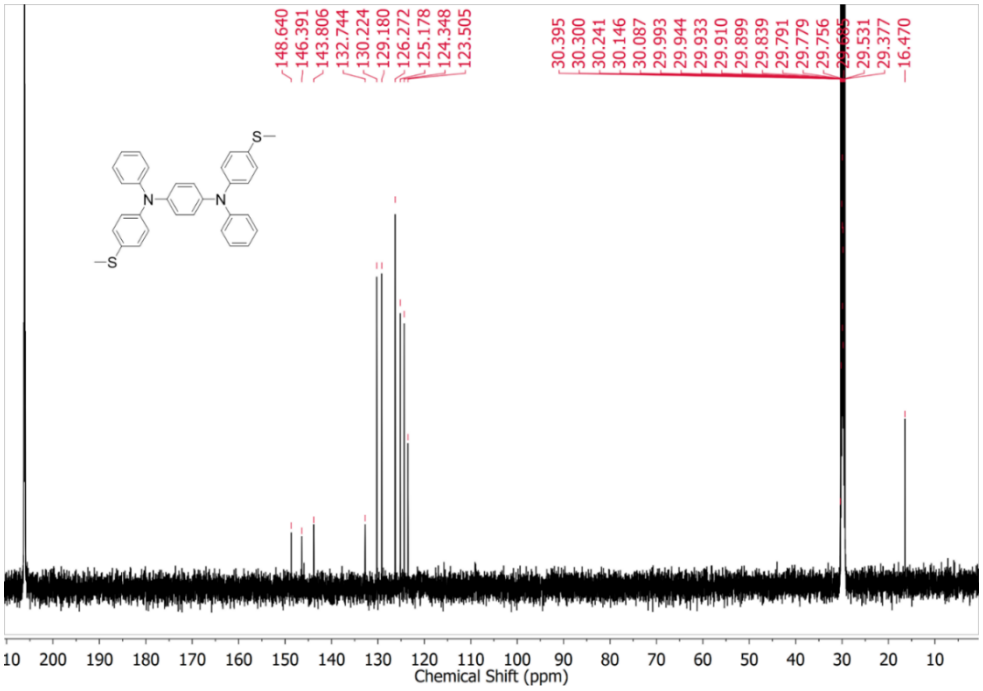

[1]H-NMR of **B2** (400 MHz, Acetone-d6, 25ºC)

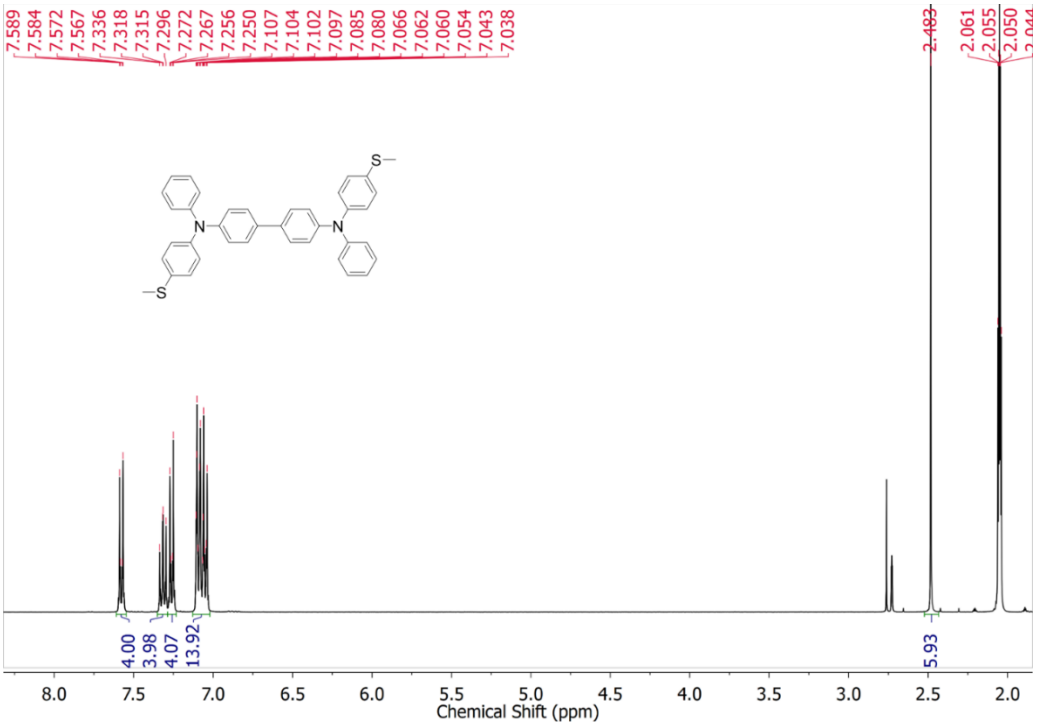

[13]C-NMR of **B2** (125 MHz, Acetone-d6, 25ºC)

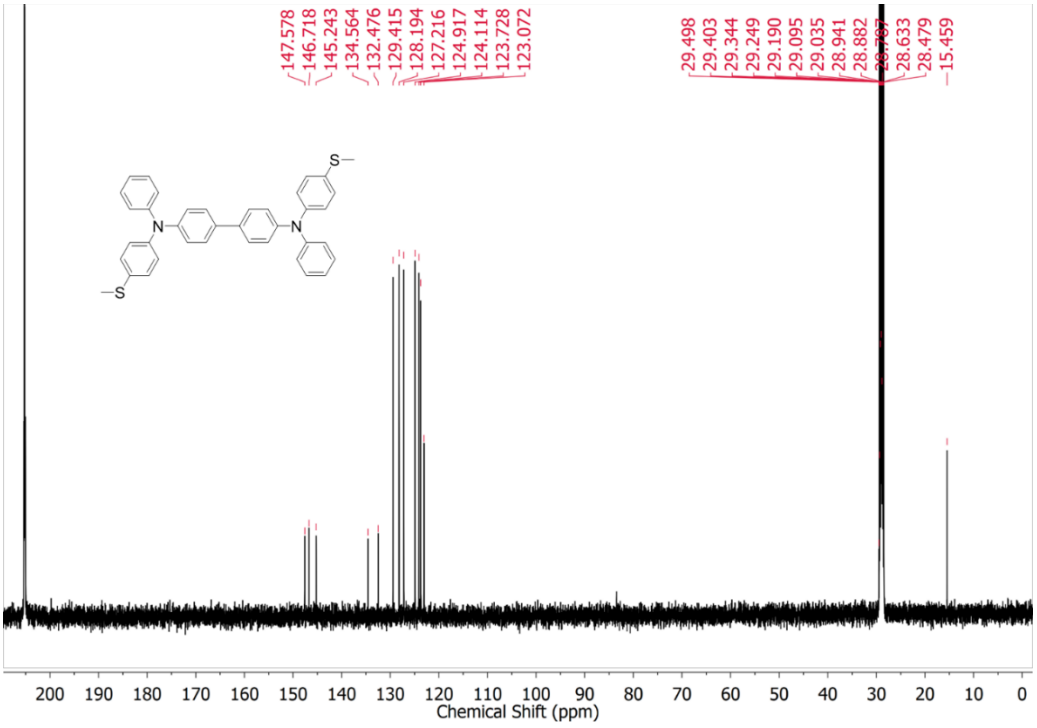

[1]H-NMR of **B3** (400 MHz, Acetone-d6, 25ºC)

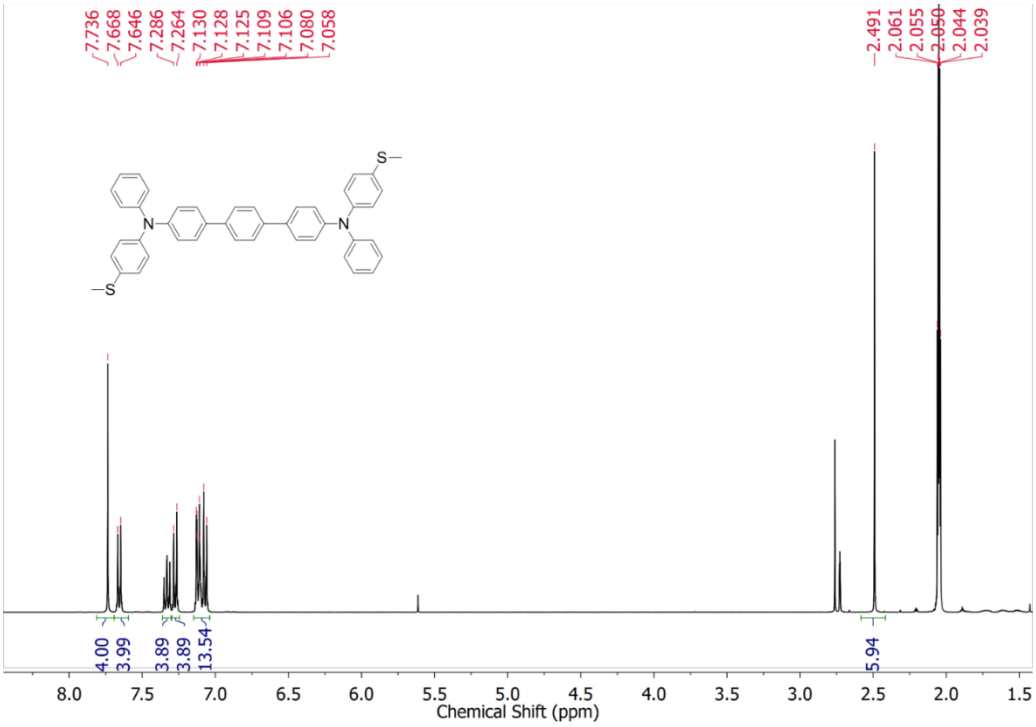

[13]C-NMR of **B3** (125 MHz, Acetone-d6, 25ºC)

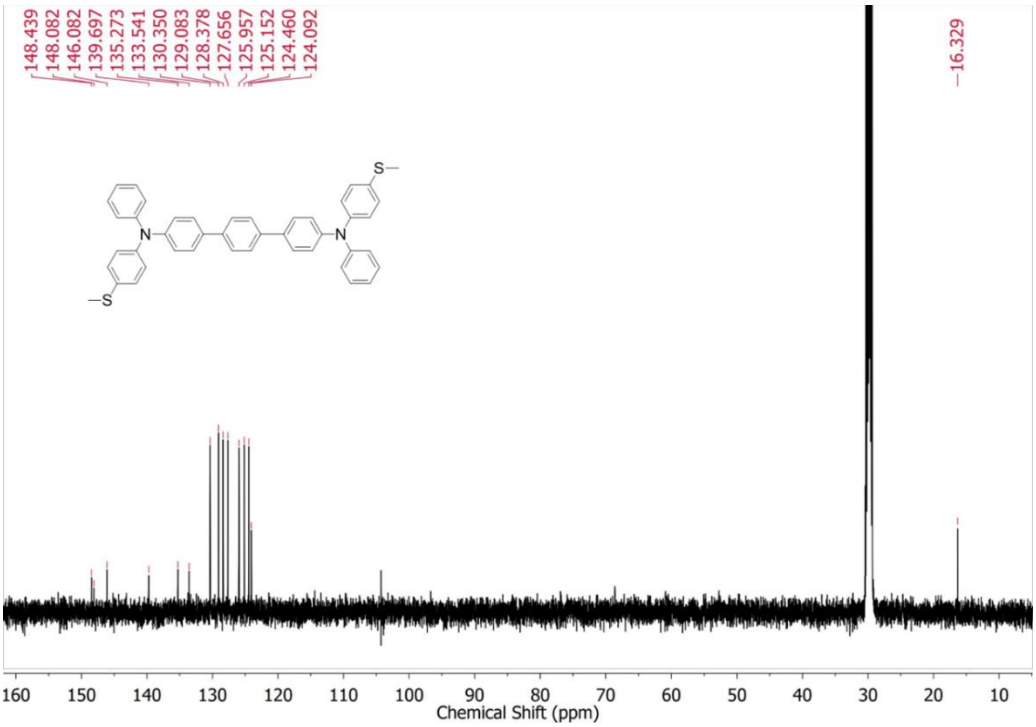

^{1}H-NMR of **B2-mono** (400 MHz, CD_2Cl_2, 25ºC)

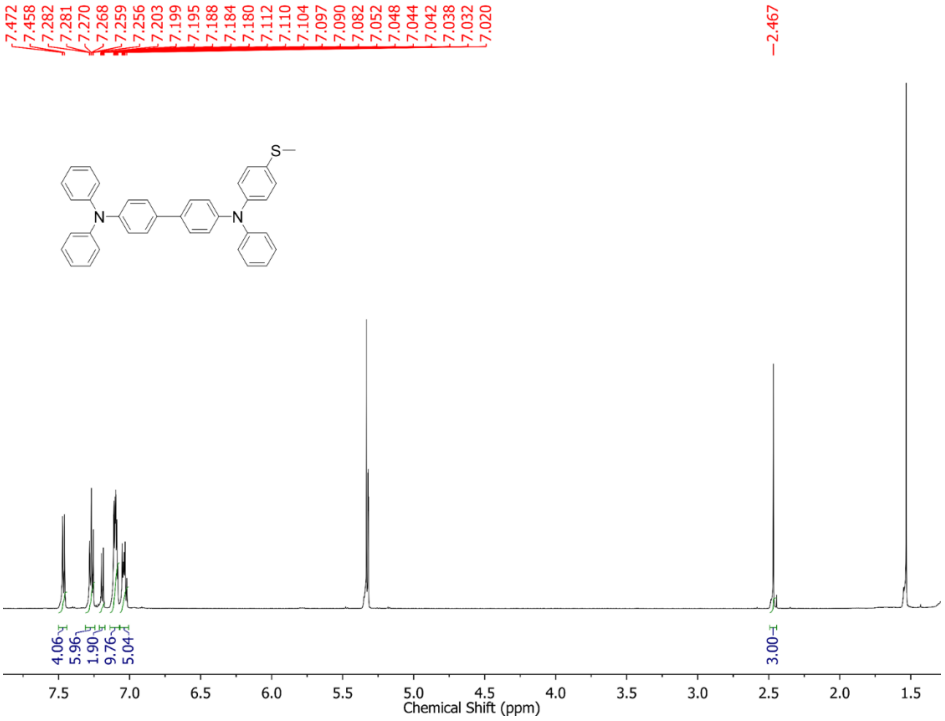

^{13}C-NMR of **B2-mono** (125 MHz, CD_2Cl_2, 25ºC)

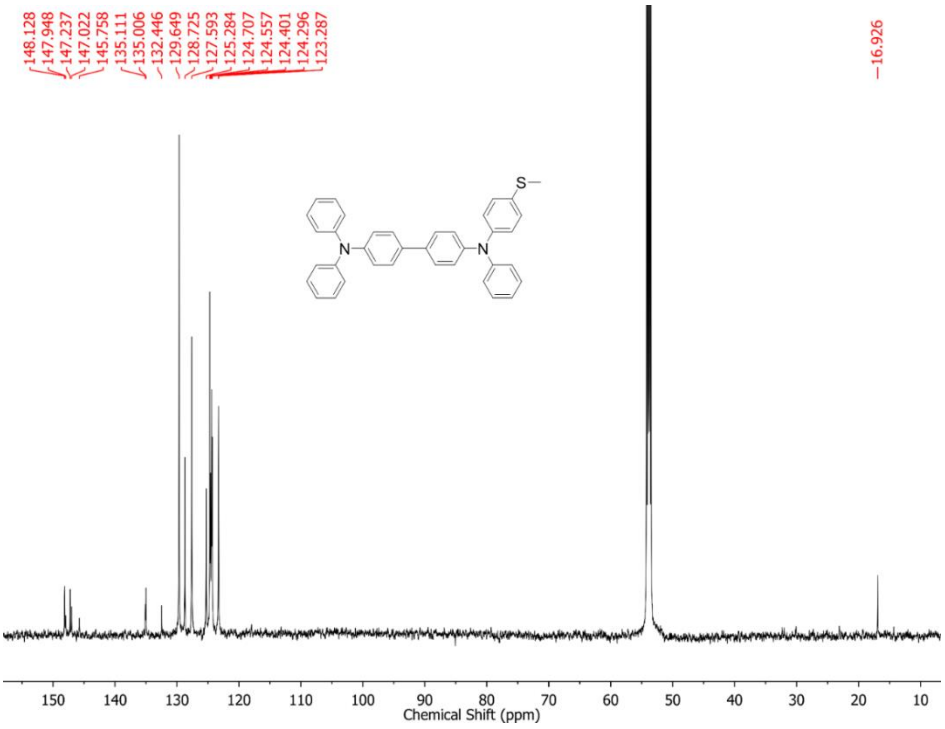

7.3 Compounds in Chapter 4

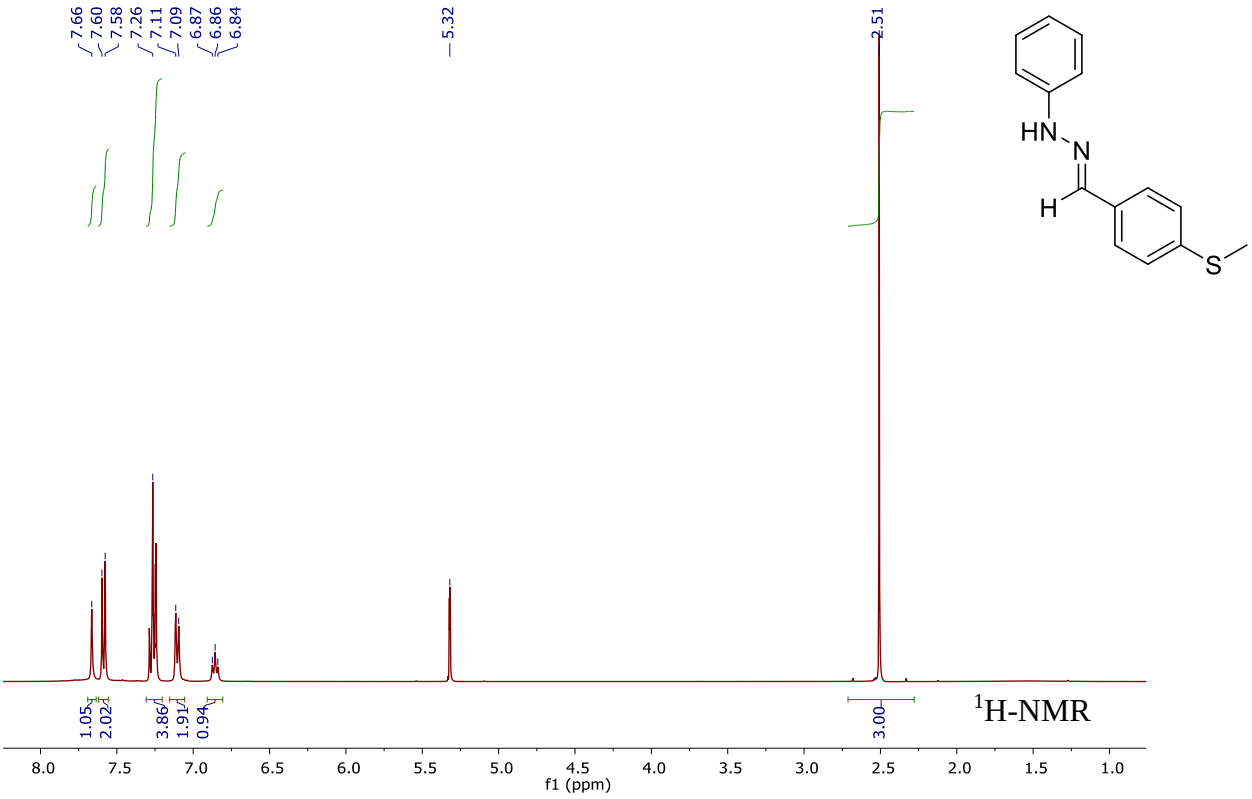

^{1}H-NMR

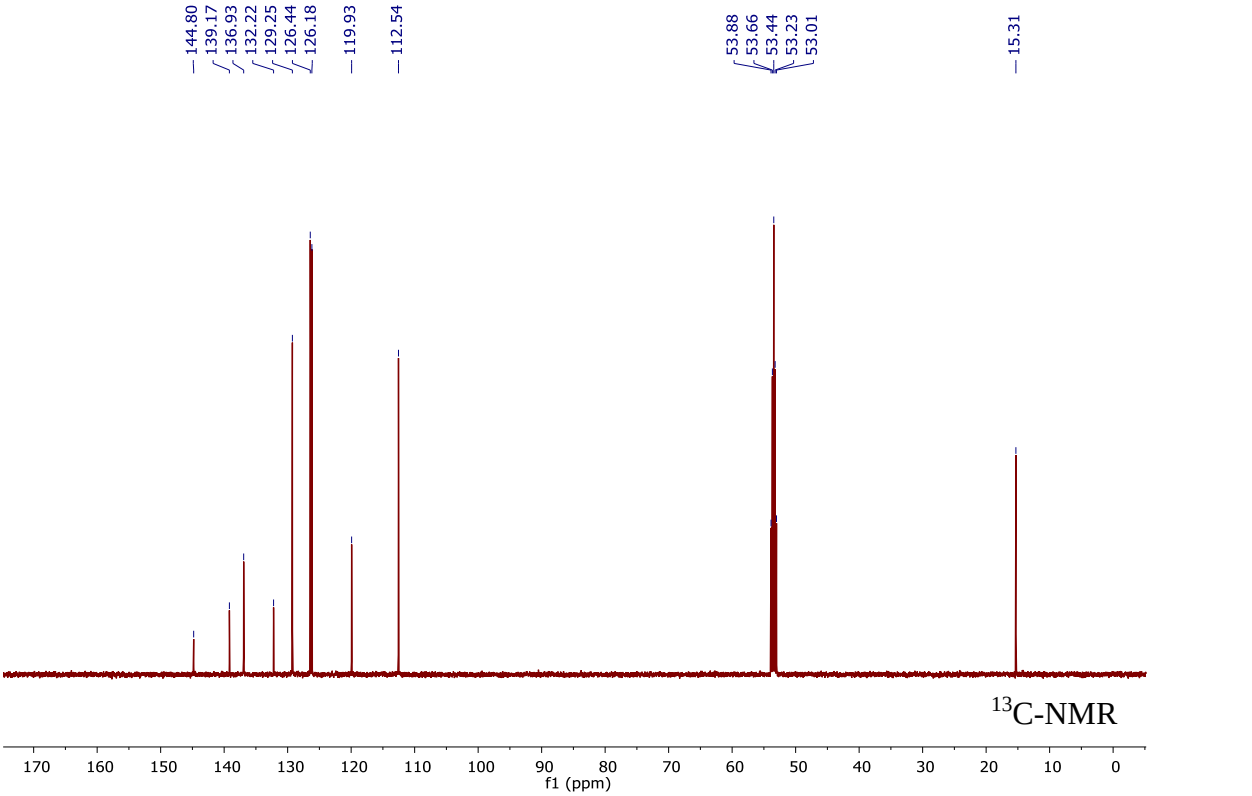

^{13}C-NMR

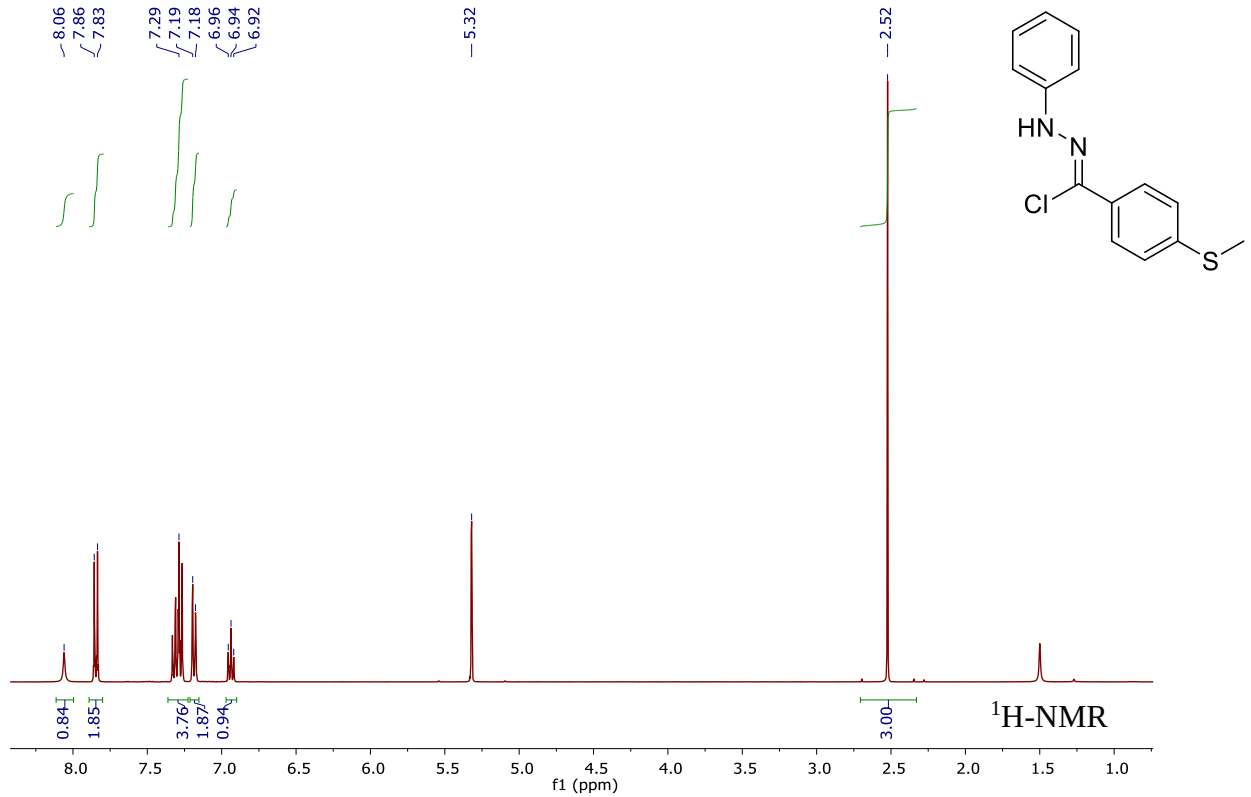

^{1}H-NMR

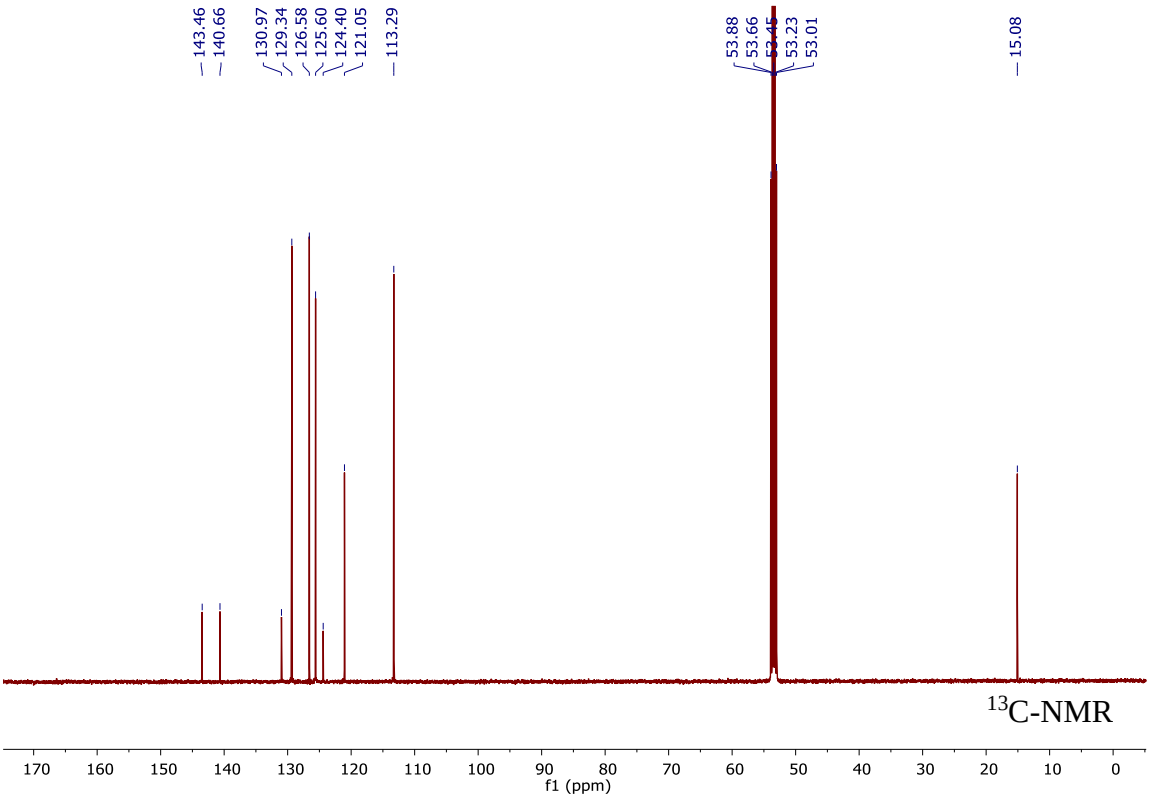

^{13}C-NMR

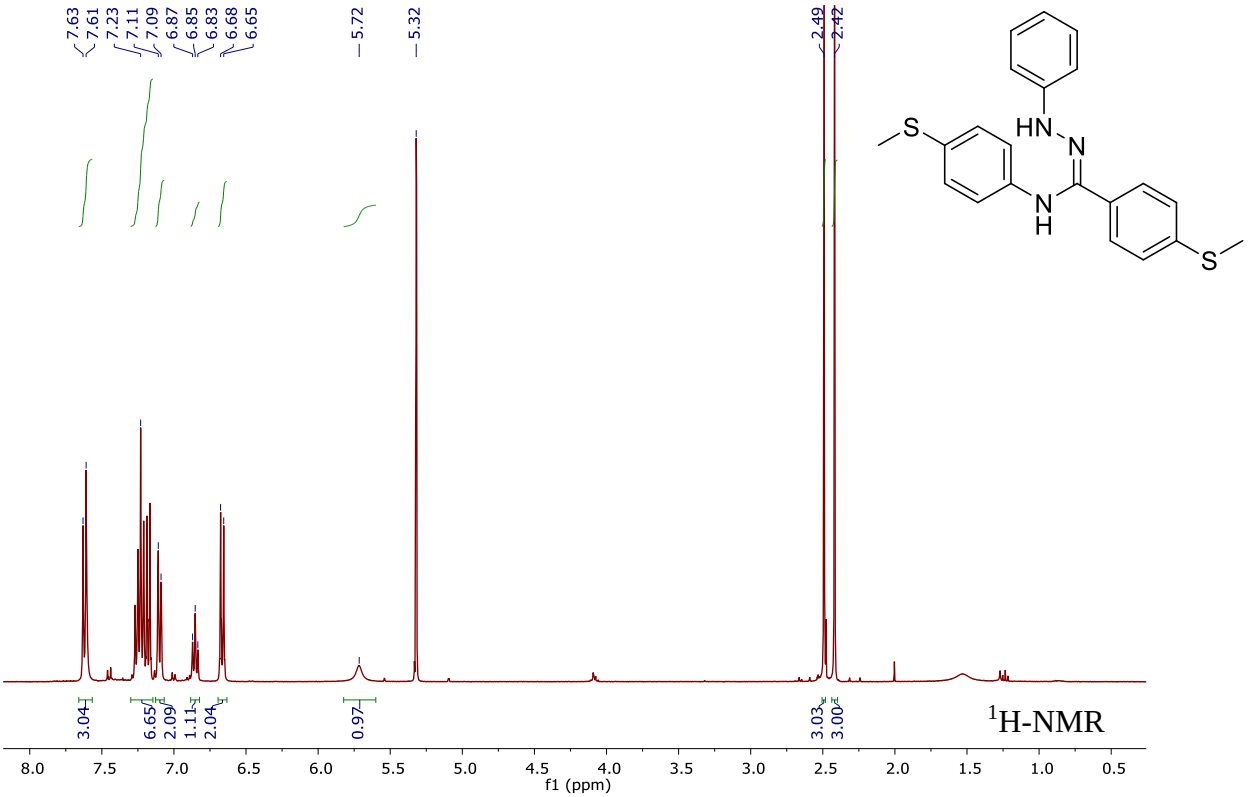

^{1}H-NMR

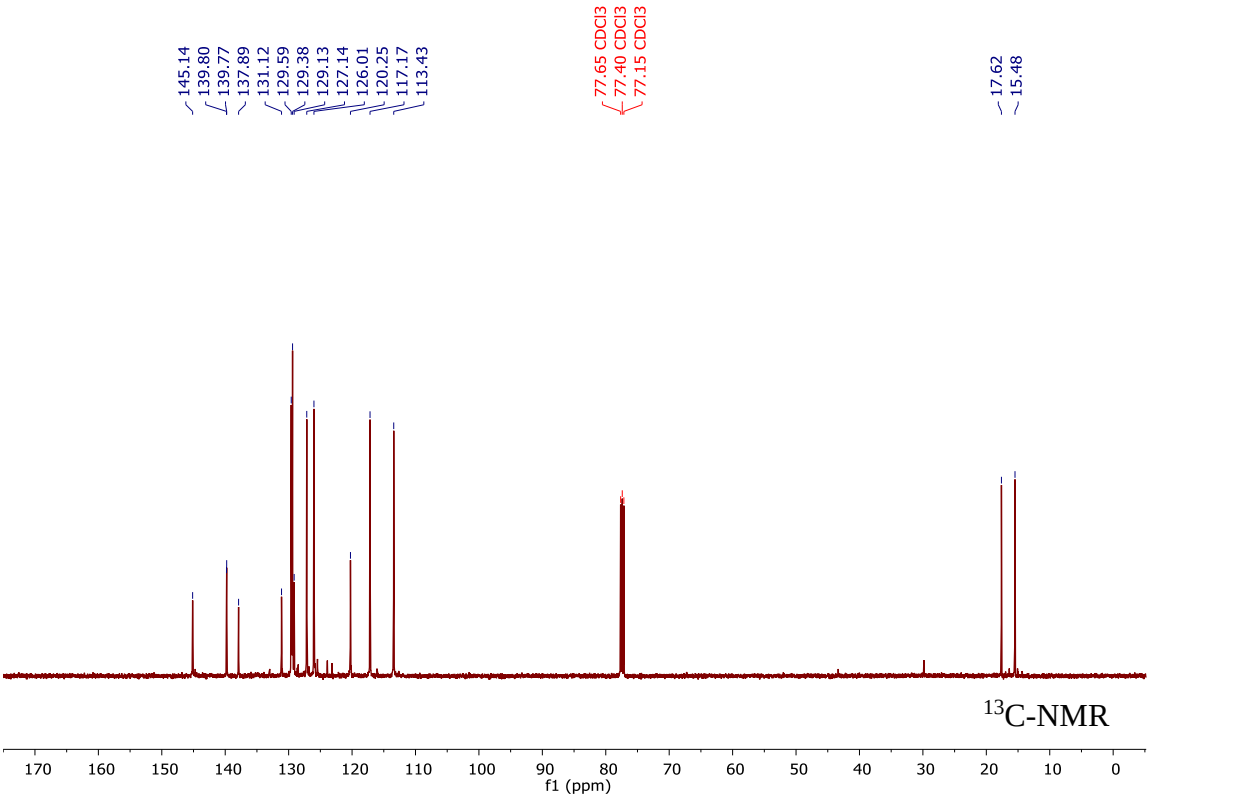

^{13}C-NMR

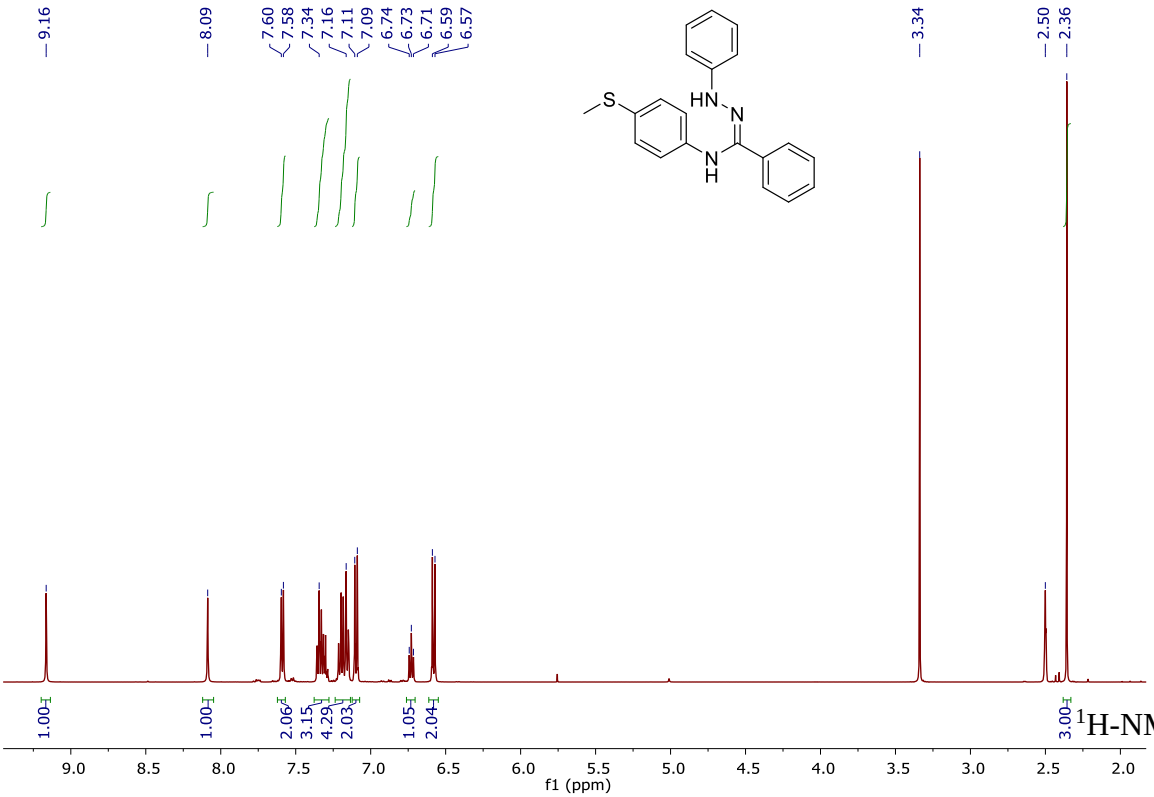

^{1}H-NMR

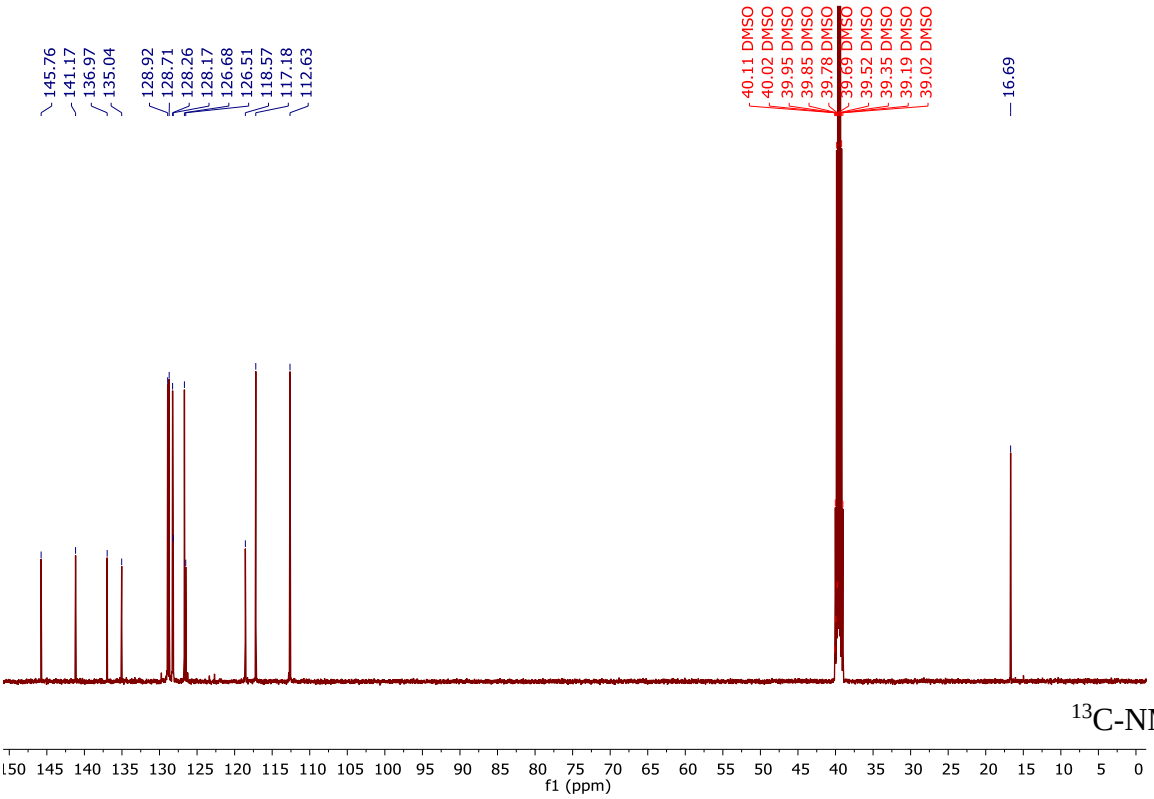

^{13}C-NMR